University of Kerbala

College of Science

Department of Physics

Performance Enhancement of MWCNTs-ZnO/TiO_2 Nanostructure Solar Cell

A Thesis
Submitted to the Council of the College of Science, University of Kerbala, in Partial Fulfillment of the Requirements for the Ph.D. Degree in Physics

By

Ammar Salah Hameed

Supervised by

Prof. Dr. Rajaa A. Madlool **Prof. Dr. Noor J. Ridha**

2022 AD **1444 AH**

بِسْـــــمِ اللهِ الرَّحمَـنِ الرَّحِيـــــم

هُوَ الَّذِي جَعَلَ الشَّمْسَ ضِيَاءً وَالْقَمَرَ نُورًا وَقَدَّرَهُ مَنَازِلَ
لِتَعْلَمُوا عَدَدَ السِّنِينَ وَالْحِسَابَ ۚ مَا خَلَقَ اللَّهُ ذَٰلِكَ
إِلَّا بِالْحَقِّ ۚ يُفَصِّلُ الْآيَاتِ لِقَوْمٍ يَعْلَمُونَ

صَدَقَ الله العلي العَظِيـــــم

سورة يونس - الآية (٥)

Supervisor Certificate

I certify that the preparation of this thesis, entitled "***Performance Enhancement of MWCNTs - ZnO/TiO_2 Nanostructure Solar Cell***" was made under my supervision by (**Ammar Salah Hameed**) at the College of the Science University of Kerbala in partial fulfillment of the requirements for the degree of Ph.D. of Science in Physics.

Signature :

Name: Dr. Rajaa A. Madlool

Title: Professor

Date: / / 2022

Signature :

Name: Dr. Noor J. Ridha

Title: Professor

Date: / / 2022

In view of the available recommendations, I forward this thesis for debate by the examining committee.

Signature:

Name: Dr. Rajaa A. Madlool

Title: Professor

Head of Physics Department, College of Science

Date: / / 2022

Examination Committee Certification

We certify that we have read this thesis, entitled **"Performance Enhancement of MWCNTs- ZnO/TiO_2 Nanostructure Solar Cell"** and as an examining committee, examined the student **"Ammar Salah Hameed)** on its contents and that in our opinion it is adequate for the partial fulfillment of the requirements for the degree of Ph.D. of Science in Physics.

Signature:
Name: **Dr. Thamir A. A. Hassan**
Title: Professor
Address: Al-Karkh University of Science
Date: / /2022
(Chairman)

Signature
Name: **Dr. Ghaleb Ali Al-Dahash**
Title: Professor
Address: University of Babylon, College of Science for Women.
Date: / / 2022
(Member)

Signature
Name: **Dr. Nahida Bukheet Hasan**
Title: Professor
Address: University of Babylon, College of Science, Department of Physics
Date: / / 2022
(Member)

Signature:
Name: **Dr. Rajaa A. Madlool**
Title: Professor
Address: University of Kerbala, College of Science, Department of Physics.
Date: / / 2022
(Member & Supervisor)

Signature:
Name: **Khawla Jameel Tahir**
Title: Professor
Address: University of Kerbala, College of Science, Department of Physics
Date: / / 2022
(Member)

Signature:
Name: **Dr. Mohammed A. Kadhim**
Title: Professor
Address: University of Kerbala, College of Science, Department of Physics
Date: / / 2022
(Member)

Signature:
Name: **Dr. Noor J. Ridha**
Title: Professor
Address: University of Kerbala, College of Science, Department of Physics.
Date: / / 2022
(Member & Supervisor)

Signature:
Name: **Dr. Jasem Hanoon Hashim Al-Awadi**
Title: Assist. Professor
Address: **Dean of the College of Science, University of Kerbala**
Date: 30 / 10 / 2022

Dedication

This thesis work is dedicated to . . .

My parents who provided me the best life . . .

My Wife... with my great thanks . . .

My children; Mariam & Abbas...

My brothers, sisters and my best Friends

With my love and respect,

Ammar S. Hameed

Acknowledgements

I would like to thank God Almighty for helping me complete this work, and I would like to dedicate my deepest thanks to my supervisors, **Prof. Dr. Rajaa A. Madlool** and **Prof. Dr. Noor J. Ridha**, for their guidance، patience, kindness, and motivation during the development and completion of this dissertation. Without their persistent help and support, this dissertation would not be in the present form.

I would like to thank the University of Karbala - College of science for their supporting. Also, I am deeply thankful to all members of physical department and all my colleagues for their help and supporting me to accomplish my dissertation.

Great thanks to my family especially my mother, father and my wife for their patience and support and also to all my friends and to all lovely people who helped me, directly or indirectly to complete this work.

Ammar S. Hameed

Abstract

Innovations in materials technology in the fields of photovoltaic (PV) play a key role in the paradigm shift from fossil fuels to renewable sources. The solar energy sources are one of the renewable energies that exhibited several advantages such as low cost, simple assembly, and environmentally friend. The main objectives of this study are to fabricate dye-sensitized solar cell (DSSC) and improve their performance.

Platinum thin films were prepared on the FTO substrate with different H_2PtCl_6 precursor concentration 2.5, 5, 10, and 15 mM using spin-coating methods as a counter electrode. On the other hand, titanium butoxide ($Ti(OBu)_4$) precursor was used to prepare titanium dioxide nanorods TiO_2 as a photoanode using hydrothermal method directly on the FTO glass with different hydrochloric acid (HCl) – water (H_2O) ratios of 12.5-7.5, 10-10, 7.5-12.5 and 5-15 ml and etching times of 24, 48 and 72 h. In addition, ZnO NRs were synthesized on TiO_2 NR using seeding and growth process. 0.01 M seed solution of zinc acetate was used to prepare zinc oxide (ZnO) seed layer on TiO_2 NR by spin coating device. Then hydrothermal method was used to grow ZnO NR in aqueous solution of 0.03M zinc nitrate hydrate, hexamethylenetetramine (HMT) and deionized water (DI). Moreover, multi-walled carbon nanotubes (MWCNT) were insetted into ZnO seed layer with different concentration of 0, 0.5, 1 and 1.5 wt.%. Finally, photoanode was immersed in N719 dye for 24 h and assembled with the counter electrode (CE) to complete a sandwich-structure DSSC then sealed and filled by Meltonix 45 µm and electrolyte (Iodolyte HI-30) respectively.

X-ray diffraction (XRD) results illustrate that the TiO_2 samples have polycrystalline rutile phase structures with preferred orientations (101) and (002). ZnO NRs were grown on the (002) plane. Furthermore, there is no

distinct MWCNT peak due to the small amount of MWCNT perhaps cannot be detected. As well as the variation of the MWCNT concentration led to shaft the ZnO peak position. The increase of HCl concentration leads to an increase in the rod diameter of the TiO_2 NRs and decrease the length as exhibited in scanning electron microscopy (SEM) Image. While the etching time leads to a decrease in the diameter and length of TiO_2 NRs.

The morphology of ZnO has a rods shape and the crest of ZnO NRs has a hexagonal shape. In addition, the Energy-dispersive X-ray spectroscopy (EDX) spectrum verified that the prepared samples were pure and no other impurities were found. Moreover, the ultraviolet-visible (UV-Vis) spectroscopy shows the optical properties of synthesized TiO_2 NRs where declare that the optical band gap decreased with increasing the HCl concentration while it increased with increasing the etching time. The ZnO growth on TiO_2 NRs leads to an increase in the Eg of the optical electrode whereas reduces with an increase in MWCNT content.

Current density-voltage (J-V) measurement show that the increase in the H_2PtCl_6 precursor concentration leads to an increase of the solar cell efficiency of 1.666, 2.067, 2.96 and, 2.96 for single layer film while gradually decreased to 2.956, 2.938, 2.891 and 2.816 with increase in the H_2PtCl_6 precursor concentration for double layers. On the other hand, the optimum efficiency (η) of DSSC based on TiO_2 NRs was 3.255% at sample ET where the preparation condition (7.5 ml HCl + 12.5 H_2O) with 48 h etching time. The DSSC constructed with ZnO/TiO_2 based photo-anode shows remarkably improved efficiency (η) of 20 % where improved the electron transfer.

The solar cell efficiency of insetted MWCNT into ZnO seed layer of the fabricated cells are 3.938, 4.358, 4.047 and 3.203 with increase the MWCNT concentration. At the best conditions, the incorporation of MWCNTs at 0.5

wt% increases the conversion efficiency by approximately 10%. Finally, the total improving on the TiO2 nanostructure photo anode was 34%.

List of Content

Contents

List of Content

List of Tables

List of Figures

List of Symbols

Symbols	Description	Unit
^{o}C	Centigrade degree	degree
σ	Conductivity	$(\Omega.cm)^{-1}$
J	Current density	mA/cm^2
η	Efficiency	-
η	Rear to front efficiency ratio	-
υ	Frequency	Hz
D	Grain size	nm
h	Hour	h
I^-	Iodide	-
a, b, c	Lattice constant	nm
$\mathbf{d_{hkl}}$	Inter planer distance	nm
$\mathbf{E_f}$	Fermi level energy	eV
$\mathbf{I_{max}}$	Maximum current	mA
J_{max}	Maximum current density	mA/cm^2
$\mathbf{V_{max}}$	Maximum voltage	Volt
$\mathbf{P_{max}}$	Maximum Power	Watt
hkℓ	Miller indices	-

List of Symbols

V_{oc}	Open-circuit voltage	Volt
e-	Photoelectron	
hυ	Photon energy	eV
R	Resistance	Ω
ρ	Resistivity	Ω.cm
R_s	series resistance	Ω
I_{sc}	Short circuit current	mA
R_{sh}	shunt resistance	Ω
T	Temperature	K
t	Thickness	m
I_3^-	Triiodide	-
λ	Wavelength	m

List of Abbreviations

Abbreviation	Description
AM	Air Mass
AFM	Atomic Force Microscope
CNT	Carbon Nanotube
CB	Conduction Band
CE	Counter Electrode
DSSCs	Dye-Sensitized Solar Cells
eV	Electron-Volt
Eg	Energy Gap (Ev)
EDX	Energy-Dispersive X-Ray Spectroscopy
FF	Filling Factor
FTO	Fluorine-Doped Tin Dioxide
FWHM	Full Width at Half Maximum
HOMO	Highest Occupy Molecular Orbital
ITO	Indium Doped Tin Oxide
Pin	Input Optical Power (Mw/Cm^2)
µm	Micrometer
mm	Millimeter

List of Abbreviations

mW	Milliwatt
MWCNT	Multi Walled Carbon Nanotube
nm	Nanometer
NRs	Nanorods
NPs	Nano particles
NIR	Near Infra-Red
PE	Photoanode
Ru	Ruthenium
SEM	Scanning Electron Microscopy
TiO_2	Titanium Dioxide
$Ti(OBu)_4$	Titanium(IV) Butoxide
TCO	Transparent Conducting Oxi
VB	Valance Band
XRD	X-Ray Diffraction
ZnO	Zinc Oxide

Chapter One

Introduction and Literature Review

Chapter One
Introduction and Literature Review

1.1 Introduction

In recent years, investigations on clean and secure energy sources have been received tremendous attention due to the lack of fossil based sources and their hazards to environment [1]. Over 85% of humanity's energy demand is met by fossil fuels, leading to severe climate changes such as global warming and depletion of our planet's natural sources [2,3]. Nowadays energy crisis is a big issue for every country in the world. Fossil fuel is still an idol because of its relatively low price, ease in the usage and availability. However, since the reserves are becoming to decrease, alternative energy resources especially which are eco-friendly and inexpensive are urged to be explored and utilized. Henceforth, the development of renewable energies with fossil fuels free like wind [4], solar thermal [5], biomass [6], hydropower [7] as well as photovoltaic (PV) [8] energy has been widely studied in order to overcome the global issues. It is worth to mention that the natural renewable energy like solar energy can be converted into controllable and useful energy which is everlasting and potential damage/pollution free to the environment. Solar energy is also considered to be a large clean energy source [9].

However, the production cost, device size, stability, repeatability, reproducibility, and also its efficiencies have yet to approach to the green and sustainable technology in future. Moreover, solar energy is the most renewable, abundant and green energy which could be converted into electrical or thermal energy [10]. Therefore, using solar energy in the future will have a positive effect on national economies [11]. The production, investment and usage of renewable energy are growing worldwide. However, a variety of different renewable energy sources, amongst them PVs could make a great contribution, would make the transition from fossil fuels to renewable energy possible

[12,13]. The PV technology is one of the direct ways of converting sunlight into usable energies [14]. PVs have a huge potential since the sun is a never ending energy source providing us with more energy in an hour than the world human population consumes in a year [15]. There will not be one solution for the renewable energy production in the future. Different regions in the world have different resources.

Solar cells improved significantly in the last few decades into four generations depending on time and categories of materials which are used for their fabrication as shown in Figure 1.1. The most common solar cells available in the market are the first-generation solar cells which comprise single and multicrystalline silicon. Second-generation solar cells were introduced as a response to high material usage and cost of silicon solar cell. To reduce the material usage, the maximum film thickness for this generation was brought down to a few nanometers to tens of micrometers. Meanwhile many researchers have attempted light management concepts using dye-sensitized solar cells (DSSCs), perovskite, organic solar cells, photo chemical cells, QDs, nanostructuring, and nanopattering. Fourth-generations solar cells fall in the class of conjectural generation consisting of composites [16,17].

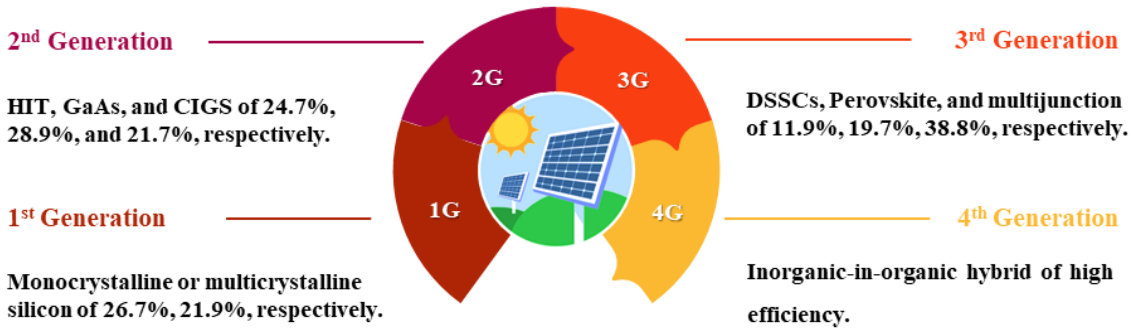

Figure 1.1. Schematic diagram of the PV solar cells generations and the current PV efficiencies [16].

DSSC represents the most prominent third generation solar cell. It is expected to provide solutions to enhance energy demand along with its

flexibility in architecture, multicolor options, low production cost, transparency and short energy pay-back time even though this field is dominated by solid-state junction devices [18]. Particular DSSCs have important features due to the low cost and simple fabrication as compared with conventional silicon solar cells [11].

DSSC has a number of attractive features; it is simple to fabricate using conventional roll-printing techniques, is semi-flexible and semi-transparent which offers a variety of uses not applicable to glass-based systems, and most of the materials used are low-cost [19–21]. In practice it has proven that it is difficult to eliminate a number of expensive materials, notably platinum and ruthenium, and the liquid electrolyte presents a serious challenge to make a cell suitable for use in all-weather [22–24].

This kind of solar cells is environmentally friend and emulates the chlorophyll photosynthesis process which takes place inside leaves, where photons are absorbed by chlorophylls, explaining the fundamental role of the dyes in DSSCs. On the other hand, also the semiconductor layer is very important in the electron conduction and transport processes in a PV cell. Moreover, the chemical and physical proprieties can influence the final efficiency of the device. A suitable semiconductor has to display a wide band gap that can fit the HOMO-LUMO dye energy level, a nanostructured morphology, relatively high surface area, pore volume and diameter for a proper dye adsorption and large crystallite domains to decrease traps-level recombination of carriers [25,26]. For these reasons, an appropriate semiconductor for DSSC is titanium dioxide (TiO_2) and zinc oxide (ZnO) nanoparticles (NPs) or nanorods (NRs) that shows a band gap of 3.0-3.2 eV, which can be prepared as a nanostructured material, with tunable surface area and pore size distribution [27–30]. Therefore, it is important to consider the

materials selection and suitable DSSC components to produce solar cells with high performance.

1.2 Literature Review

Recently, DSSC have drawn great attention with a low production cost of electricity and high energy conversion efficiency. This literature review includes the preparation of TiO_2 and ZnO as a DSSC. Moreover, the effect of inserting the carbon nanotube (CNT) in the photoanode structure on the DSSC performance.

1.2.1 Preparation of TiO_2 as DSSC

Teen-Hang Meen et al [31] in 2012 prepared TiO_2 nanotube arrays as a photo electrode using electrochemical anodization methods. The lengths of TiO_2 nanotube arrays were obtained approximately around (10-30) μm where the efficiency of TiO_2 nanotubes increases with increment the rods length. The $TiCl_4$ treatment leads to improve the dye-sensitized solar cell efficiency of TiO_2 nanotubes up to 6.58%.

In 2013, J. R. Hou [32] grown TiO_2 NRs arrays on fluorine-doped tin oxide (FTO) substrate using hydrothermal method. TiO_2 NR arrays with different morphologies were obtained by systematically changing preparation conditions, including reaction temperature, reaction time, and concentrations of the reactants in the solution. The optimum obtained PV cell performances are as follows: open-circuit voltage (V_{oc}) (0.64) V, short-circuit current density (J_{sc}) (0.41) mA, filling factor (FF) (0.69), and photoelectric efficiency (η) (0.7%). It's concluded that the morphology of TiO_2 NRs array is controllable, and their photoelectric properties can be modified by altering the morphology.

In 2015 G. Wang et al [33] fabricated high-efficiency DSSCs based on multi-layered composite film photoanodes. Where the photoelectric conversion efficiencies were (4.92, 6.37 and 8.03) % for DSSCs based on NRs/NRs

(DNR), NPs/NPs (DNP) and NPs/NRs (NPR) photoanodes. NPR photoanodes exhibited the best PV performance with a short-circuit current of (15.7) mA cm^2. The enhanced photo-electricity performance of NPR solar cells could be attributed to the geometry of TiO_2 NRs provided a fast and long charge carrier transfer pathway, thus improving the transfer of photo-induced electrons. As well as TiO_2 NRs NPs provided a large surface area.

Y. L. Lai et al [34] in 2017 investigated the influence of thin film thickness of working electrodes on the PV characteristics of DSSCs . TiO_2 thin films, with the thickness from (7.67 to 24.3) μm, were used as working electrodes of DSSCs. A TiO_2 film was coated on a FTO conductive glass substrate and then sintered in a high-temperature furnace. The PV results showed the increasing of thickness of the TiO_2 film from (7.67 to 18.5 and 24.3) μm led to decrease J_{sc} and PV conversion efficiency of the DSSC.

In same year A. M. A. Alsammarraie and M. K. Jawad [35] studied the electrical conversion efficiency (η %) of the dye sensitive solar cells with different TiO_2 morphology. TiO_2 nanotube produced via anodizing of the Ti foil in ethylene glycol containing (0.5%) NH_4F and 4 mL deionized water (DI), at different anodizing potentials for 1 h at room temperature. The tube's wall thickness of the TiO_2 increased with increased anodizing potential. The calculated (η %) ranged between (0.370 and 2.126 %). It’s concluded that the electrical conversion efficiency (η %) continuously increased due to the tube's wall thickness increment.

N. Rab et al [36] in 2018 a new reaction medium containing water and glycerol used to synthesis the anatase phase TiO_2 NPs. TCl_4 is used as a precursor solution. The band gap calculated from UV-Vis spectra ranged from (3.02-3.28) eV. The TiO_2 NPs exhibited spherical shapes in the form of nano-clusters were revealed in the FESEM images. The crystallite sizes of TiO_2 NPs ranged from (9.50- 26.14) nm. As well, the sizes of the TiO_2 NPs increased

with increased the calcination temperature. Moreover, smaller particles and lowers the band gap of TiO_2 NPs were formatted by the promotion of the glycerol.

I. O. Selyanin et al [37] in 2020 proposed a simple method to prepare TiO_2 paste using titania powder (Degussa) and organic binders (terpineol and ethyl cellulose) for making a continuous photoactive layer of a DSSC. The DSSC PV characteristics were measured for the prepared and commercial pastes. The open-circuit photovoltage value reaches (0.4–0.5) V; J_{sc} reaches (1 mA/cm^2) for both layers. Finally, The TiO_2 layers produced using either prepared or commercial paste had similar properties, but the prepared paste was cheapest to manufacture.

M. M. I. Megat Hasnan et al [38] in 2021 prepared TiO_2 rutile NR-flower (T-NRF) by hydrothermal using TiO_2 reactive ion high impulse power magnetron sputtering (HiPIMS) treatment. The IPCE and UV–Visible analysis shows an increment of dye absorption in the visible wave region due to improve in T-NRF photoanode dye absorbance after HiPIMS treatment. Both photoanodes with and without HiPIMS treatment were used in DSSC fabrication. The DSSC efficiency with HiPIMS treatment photoanode is improved by (80%) due to improvement of open-circuit voltage and short-circuit current density. It was proved that the HiPIMS treatment is capable to improve the T-NRF photoanode prepared by hydrothermal method, hence improved the DSSC performance.

W. F. Lai et al [39] in 2022 utilized the physical and chemical methods to fabricate the TiO_2 strip array. A TiO_2 strip array was a one-dimensional protrusive structure with a thickness of 90 nm fabricated by photolithography. A porous compact layer made of TiO_2 NPs was coated on TiO_2 strip array. The conversion efficiency (4.38%) of DSSC with TiO_2 strip array exceeded that (3.20%) of a DSSC without a TiO_2 strip array by (37%). The increase of

DSSCs efficiencies due to TiO_2 strip array provided a large surface area of the one-dimensional protrusive structure and specific electron transport paths.

In same year J. hun Bae et al [40] determined the ultrasonic treatments on TiO_2 particles to manufacture the photoelectrodes of a dye-sensitized solar cell (DSSC). Two methods were used to prepare TiO_2 particles directly sonicated by an ultrasonic horn, and TiO_2 treated indirectly by an ultrasonic cleaner. TEM, XPS analysis was confirmed that cavitation bubbles generated during ultra-sonication. The energy conversion efficiency of the ultrasonic horn DSSC was measured to be (3.35%), which is about (45%) increase in comparison to that of the non-ultrasonic treated DSSC (2.35%). In addition to this regard, recombination resistance of ultrasonic horn DSSC was calculated to be (450) $\Omega \cdot cm^2$, increasing more than two times compared to the non-ultrasonic treated DSSC (200) $\Omega \cdot cm^2$.

1.2.2 Preparation of (CNT, TiO_2 and ZnO) as DSSC

Y. Lou et al [41] In 2013 reported a simple method to decorate TiO_2 NPs on ZnO for DSSC. By simple immersing ZnO film into butyl alcohol solution of tetrabutyl titanate (TBOT), TiO_2 NPs were well decorated onto ZnO nanocrystal surface. By taking the advantage of the hydrolysis and condensation differential of different TiO_2 precursors, the simple method allowed an easy tune over the TiO_2 modification structure on ZnO nanocrystilie for DSSC application. As the concentration of TBOT increasing, the J_{sc} firstly increased and then declined as the concentration greater than (0.50 M). The V_{oc} or FF has no significant change as the concentration increasing. They suggested the change of J_{sc} at (0.50 M) content of TBOT was ascribed to the alteration of the electron collection mechanism.

In the same year L. Yang and W. W. F. Leung [42] obtained a high power conversion efficiency of (10.24%) in a dye- sensitized solar cell by

incorporating multiwall carbon nanotubes (MWCNT) inside a TiO_2 NR photoanode. The MWCNT in the NR could effectively collected and transported the photo-generated electrons which in turn reduced the recombination as well as improved the efficiency of the device.

G. K. L. Goh et al [43] in 2014 synthesized high aspect ratio ZnO NR arrays on FTO glasses via a low temperature solution method. By adjusting the growth condition and adding polyethylenimine, ZnO NR arrays with tunable length were successfully achieved. Results of solar cell testing showed that addition of a TiO_2 shell to the ZnO NR significantly increased short circuit current from (4.2 to 5.2) mA/cm^2), open circuit voltage (V_{oc}) from (0.6 V to 0.8 V) and FF from (42.8% to 73.02%). The overall cell efficiency jumped from (1.1%) for bare ZnO NR to (3.03%) for a ZnO@TiO_2 core shell structured solar cell with 18–22 nm shell thickness, a nearly three-fold increase.

M. Z. Razali et al [44] in 2014 used sol-gel method to prepare CNT/TiO_2 doped ZnO nanocomposite using for DSSC. All samples are designated as CNT/TiO_2 – x, where x is the mol % of the Zn [x = 0.5, 1.5 and 2.5]. The percentages efficiency (η) for (0.5 %, 1.5% and 2.5 mol %) were as follow (2.2 %, 2.4 % and 2.8 %), respectively.

In 2015 F. Li, Y. Jiao et al [45] synthesized TiO_2/ZnO nanodonuts by one step electrospray method, and the effects of different morphologies and ZnO concentrations on the performances of DSSCs were studied. The DSSC efficiency of optimized ZnO concentration (9.00%) was obtained with J_{sc} of (16.70) mA / cm^2, V_{oc} of (0.78) V and FF of (0.69), which is (44.4%) higher than of pure TiO_2. Where the dye absorption is higher and more efficient electron transport and electrolyte penetration properties.

In 2018, Z. Arifin et al [46] fabricated DSSCs using double-layer photoanodes consisting of TiO_2 NPs and Zn-doped TiO_2 hollow fibers (HFs). The TiO_2 HFs were prepared by co-axial electro-spinning and used as the light-

scattering layer in the DSSC. The highest efficiency of the DSSC (3.122%) was achieved with a (15 µm) NP-5 µm HF photoanode, for which the short-circuit photocurrent density, open-circuit photo-voltage, and FF were (15.81 mA/cm^2, 0.566 V, and 34.91%), respectively.

In 2018, S. Noor et al [47] used sol-gel process to synthesis TiO_2 and ZnO nanomaterials. The varied amount of ZnO was incorporated onto surface of TiO_2 by wet chemical impregnation method to fabricate ZnO/TiO_2 hetero structures. The photoanodes of DSSC fabricated with ZnO/TiO_2 nanocomposites were characterized by photocurrent-voltage measurements and exhibited the enhancement in PV properties as compared to bare TiO_2. (15.0 %) ZnO/TiO_2 heterojunction is optimum quantity which delivered (2.8%) greater PV efficiency than bare TiO_2 based DSSC.

In 2019 F. Kabir et al [48] fabricated ($TiCl_4$) treated FTO/MWCNT-TiO_2) as photoanode with difference MWCNTs concentration. As the concentration of MWCNTs in TiO_2 was increased, the cell efficiency also increased gradually until it reached an optimum concentration of (0.015 wt.%). Further increments in MWCNT's concentration in TiO_2 led to the negative effect of the DSSC's cell parameters by decreasing the short circuit current and the FF, thus decreasing the overall cell efficiency.

In 2020 T. S. Bramhanka et al [49] prepared blocking layer by using TiO_2 and TiO_2 doped Zn and Ni with various concentrations. the co-doped TiO_2 of Zn and Ni improved the PV parameters. The blocking layer of Zn and Ni co-doped TiO_2 gave (61%) increase in the efficiency as compared with bare TiO_2 photoanode.

In the same year S. Aseena et al [50] prepared ZnO/CNT, ZnO/CuO/CNT nanocomposite. The working electrode for DSSC was prepared by coating the nanocomposite by doctor blade technique on FTO plates. In this method the J_{sc} and FF is highly improved as compared to the ZnO/CNT prepared by

hydrothermal procedures. The obtained results show improved efficiency for the ZnO/CNT compared to ZnO/CuO/CNT.

S. Aksoy et al [11] in 2020 investigated the growth of titania nanotubes on titanium sheets by electrochemical oxidation. ZnO NRs were decorated with hydrothermal method on TiO_2 nanotubes. Hydrothermal temperatures values were changed to find the optimal ZnO decoration density to increase photo conversion efficiency. The results showed the photo conversation efficiency of DSSC by TZ photoanode reached (1.67%) for hydrothermal temperature of (130 ℃) which is twofold higher than that of DSSC by TiO_2 nanotubes (0.81 %).

In the same year, S. Borbón [51] reported that an enhancement of the V_{OC} of about 0.10 V with respect to a TiO_2-based DSSC modified with ZnO nanoflowers that prepared by a new and facile method. An additional increase of the V_{OC} of about (0.08) V was achieved by modifying the ZnO nanoflowers with Au NPs, resulting in a DSSC with an efficiency of (2.79%), highlighted by a high V_{oc} of (0.89 V).

A. Zatirostami [52] in 2021 fabricated the DSSCs based on the TiO_2 NPs and ZnO NRs composite with different porosities. The photoanode porosity is a determining factor in the efficiency and stability of the DSSCs. The optimized cell in case of porosity showed an V_{oc} of (704 mV), J_{sc} of (14.2 mA/cm^2) and FF of (65 %), which results in efficiency of (6.5 %). This high performance corresponds to optimized amounts of dye-adsorption, charge transfer resistance, and specific surface area of the nanocomposite photoanode. The stability of this cell was measured for two months and showed only an (8%) drop in its open-circuit voltage with the suitable condition achieved.

In 2021 I. S. Mutashar and M. R. Al-bahran [53] prepared TiO_2/MWCMT nanocomposite using hydrothermal method reaction for the effective distribution of TiO_2 NPs on carbonaceous materials. MWCNT was

incorporated in a nanocomposite to increase the electron transfer of the photoanode. DSSC results showed that the energy conversion efficiency (8.96%) which is good compared to pure TiO_2 (8.147%).

X. Li et al [29] in 2021 produced well-aligned ZnO NRs using two growth methods, leading to ZnO with different surface chemistries. A thin layer of TiO_2 shell was applied via layer-by-layer adsorption method. The core–shell structure was confirmed via high-resolution transmission electron microscopy. Both PL and XPS results suggested surface defects are passivized by TiO_2 coating shell. The shell coating had a stronger effect on ZnO synthesized in OH- rich environment, due to excessive hydroxyl groups provided during synthesis, which remain even after annealing-induced crystallization.

Also in 2021 S. W. Himmah et al [19] reported that the TiO_2/ZnO rods photo anodes were fabricated in several steps. First, TiO_2 NPs were deposited on the conductive surface of indium tin oxide substrate (ITO) to form a double layer using the spin-coating method. Meanwhile, ZnO rods grown on the TiO_2 NPs layer using the hydrothermal method by varying Zinc Nitrate Tetrahydrate precursors (20, 30, 50, and 100 mM). Based on the results, the increasing concentration of Zinc Nitrate Tetrahydrate precursor affected the structural, morphological, optical, and electrical properties of TiO_2/ZnO rods multilayer photoanode and increased the J_{sc} and V_{oc}. However, the DSSC based on TiO_2/ZnO rods multilayer photoanode 50 mM with an active area of (0.5 cm^2) shown a decrement in J_{sc} (0.092 mA/cm^2) and an increment in V_{oc} (0.684 V) while photoanode based on an active area of (0.2 cm^2) showed an increase in J_{sc} and a decrease in V_{oc}, namely (0.209 mA/cm^2 and 0.494 V), respectively.

In 2022 A. S, N. ABRAHAM et al [54] Used the ultra-sonication followed by magnetic stirring of ZnO nanopowders with (0.01, 0.05, 0.1, 0.2, to 0.3) wt% of microwave irradiated functionalized CNTs to obtain ZnO/CNT nanocomposite as a ZnO based photoanode. The performance of DSSC is

greatly influenced by the varying amount of CNTs in ZnO/CNT. An optimum content of (0.1 wt%) of CNT exhibits maximum power conversion efficiency of (2.9 %). The improvement in efficiency is mainly due to the increased dye adsorption and enhanced visible light absorption provided by the ZnO/CNT nanocomposite.

1.3 The Aim of Study

The main objectives of this study are:

1. Enhancement of the dye sensitized solar cell (DSSC) performance synthesized with nano materials prepared by hydrothermal methods.
2. Obtained the optimum preparation conditions to produce MWCNTs-ZnO/TiO_2 Nanostructures Solar Cells.

1.4. Thesis Structure Overview

A comprehensive overview of the contents of this thesis will be provided by reviewing what each chapter dealt with and what was highlighted, as follows: The first one gives an introduction to the thesis by describing the background and the general overview of the current PV technologies Moreover the related literature review on the synthesis methods of semiconductor thin film and the aim of study as well as the outline of the thesis. Chapter two explains the dye-sensitized solar cell beginning with the components of a DSSC then a short description of the operating principle of the cell and the parameters related to the DSSC. In addition, the theoretical background of the working principal semiconductors photoanode of the DSSC as well as the parameters of solar cells is described. The experimental techniques for the formation of photoanode and the counter electrode (CE) films on FTO glass substrate also, DSSC preparations are presented in chapter three. Chapter four covers the major part of this thesis, where the experimental results are presented, analyzed and discussed in depth.

Chapter Two

Theoretical Part

Chapter Two
Theoretical Part

2.1 Introduction

The controllable synthesis of nanocrystalline materials has received tremendous attention worldwide in the last couple of years due to their uncommon optical, electronic, catalytic, transport and mechanical properties compared to their bulk phase counterparts [55–57]. All these uncommon properties of materials at the nanoscale are mainly governed by their size, shape, crystallinity, arrangement and structure [58]. Recently, many efforts have been made to develop metals inside semiconductor materials with typical optical properties such as strong photoluminescence, electroluminescence or nonlinear optical behavior which may lead to new optoelectronic devices with superior performance [59]. The year 1991 marked a significant milestone in the PV technology world due to the first highly efficient DSSCs invented by O'Regan and Grätze [60]. This breakthrough invention has been extensively developed for the last 30 years by worldwide scientists (about 29,770 records of scientific articles may be found in databases) [61]. Due to many advantages, such as inexpensive manufacturing costs using non-toxic substrates and leaving a remarkably lower carbon footprint, as well as workability under indoor ambient light, DSSCs are a promising alternative to the other types of solar cells [61–63]. Furthermore, DSSC technology can be considered as an alternative to p-n junction PV devices due to its several interesting features and vantages such as being semiflexible, semitransparent, using abundant and cheap materials, highly customizable and a simple manufacturing process [51,64,65]. In addition, as another attractiveness of DSSCs, it can be mentioned that DSSCs can work even in low-light conditions (cloudy skies or non-direct sunlight), whereas limitation of illumination and angle of incident light are not critical issues because of using nanocrystalline semiconductors in

this technology [30,66,67]. Basically, the DSSCs system consists of nanocrystalline semiconductor film on transparent conductive oxide (TCO) glass as the photoanode; cathode are usually made of platinum that is vacuum deposited on conducting glasses to reduce the over potential for reduction of tri-iodide to iodide in redox electrolyte, and an iodide/tri-iodide redox couple in a proper mediator as the electrolyte where described in the next section [34,68,69]. In general, the device can be associated with a sandwich-type structure in which each layer has to respect specific chemical-physical requirements as has specific and well-defined functions in the electric current generation process [34,70].

2.2 Structure of Dye sensitized solar cell (DSSC).

Figure 2.1 shows the structure and arrangement of each component of DSSC. The structure of DSSC consist of glass substrates coated with TCO, dye-sensitized metal oxide semiconductor electrode, a catalyst counter electrode, and an electrolyte solution inserted between the two electrodes [71,72].

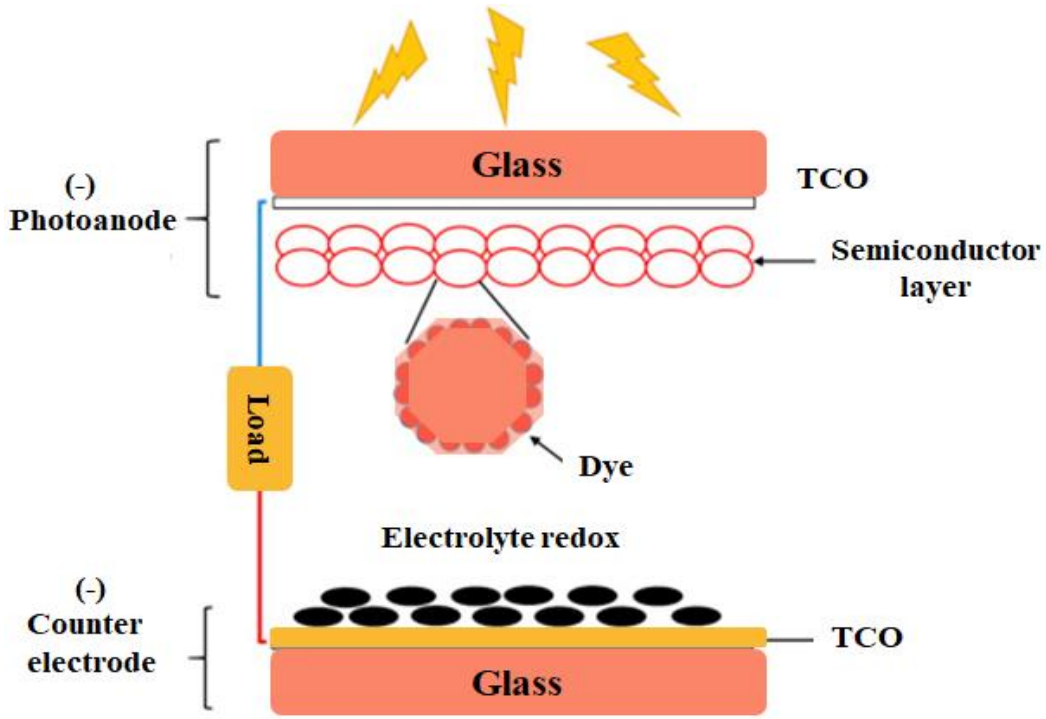

Figure 2.1. Cross section of the dye sensitized solar cell (DSSC).

a. TCO Substrate The TCO-coated glass was used as substrates for both photoanode and counter electrode. The TCO was coated by a transparent and conductive thin film. This layer is required for the collection of electrons ejected from the photoanode (dye-coated TiO_2) and passes it to CE through outer circuit. Therefore, it is called current collector. Moreover, TCO must has a very low electrical resistance of <20 Ω/sq at room temperature [71,73].

b. Photoanode consists of semiconductor metal oxide. It provides the surface area for the dye adsorption. Normally, it is used in the paste form. The power conversion efficiency PCE of DSSCs strongly depends on surface area, morphology, crystallinity, porosity and semiconductor materials CB. The dye absorption will be greater using the semiconductor materials with higher surface area [71].

c. Dye sensitizer is a dye molecule, and they play the central and most crucial role in the DSSC. It is the heart of DSSCs. It absorbs the sunlight and excited. The dye molecules which must has a deep absorbance in the visible and near-infrared of the solar spectrum that results in a high molar absorbance coefficient. Also the transfer of electrons from the dye into the semiconductor should be quicker than the decay of the dye [74].

d. The electrolyte is one of the most crucial components in DSSCs, since it is responsible for the inner charge carrier transport between electrodes and continuously regenerates the dye during DSSC operation [75]. The electrolyte constructed of a redox couple and diffused ions of reducing/oxidizing agents. Here, the following reduction and oxidation reactions have been represented to show how the tri-iodide ions get reduced to iodide ions by gain two electrons [76].

Reduction: $I_3^- + 2e^- \rightarrow 3I^-$ . . . . . (2-1)

$$\textbf{Oxidation: } 3I^- \rightarrow I_3^- + 2e^- \ldots\ldots\ldots\ldots\ldots (2\text{-}2)$$

e. Counter electrode (CE) which has a crucial role in DSSC, predominantly as a catalyst to accelerate reduction-oxidation reactions within the electrolyte. It consists of thin film of catalyst material deposited on transparent conductive glass substrate. Platinum is a popular CE in DSSC application due to it has high efficiency compared to carbon and graphene therefore platinum has nearly ideal characteristics as CE [77–79]. However, an effort to further enhance the Pt properties by adding or attach them to other materials has been reported [80].

2.3 Mechanism and Kinetics of charge transport in DSSCs.

DSSCs working is a step by step sequential phenomenon, carried out by different layers as shown in Figure 2.2 [76,81]:

a. Mechanism 1 (Photoexcitation): After the adsorption of a photon (hv) by the photosensitizer (dye), the dye molecules change from the ground state, S into the excited state, S* or excites an electron from the HOMO level to the LUMO level through the following reaction.

$$S_{adsorbed} + hv \rightarrow S^*_{adsorbed} \ldots\ldots\ldots\ldots\ldots (2\text{-}3)$$

b. Mechanism 2 (Electron injection): Then the excited dye molecules will inject the electrons to the semiconductor CB, thus leaving the dye in an oxidized state, *S*+ as follows,

$$S^*_{adsorbed} \rightarrow S^+_{adsorbed} + e^-_{\textit{injected}} \ldots\ldots\ldots\ldots (2\text{-}4)$$

c. Mechanism 3 (Energy generation): The injected electrons are transmitted through the semiconductor TiO_2 film and ultimately the electrical energy is transferred through the conductive substrate, CE,

and external circuit. This highly efficient process usually occurs in milliseconds (ms).

$$e^{-}_{\textit{injected}} + C.B. \rightarrow e^{-}_{(C.E.)} + \text{electrical energy} \quad \ldots\ldots\ldots\ldots (2\text{-}5)$$

It is crucial to note that electron transport occurred by diffusion event due to the electron concentration that becomes the main driving force for electron transport in the TiO_2 mesoporous film. Furthermore, incident light intensity plays an important role in which faster electron diffusion can be obtained at higher light intensities.

d. Mechanism 4 (Reduction of redox mediator): In the 4th mechanism, the I^3 in the electrolyte that obtains an electron will reduce to I^- at the counter electrode. Thus, the regenerative cycle is completed.

$$I_3^- + 2e^-_{(C.E.)} \rightarrow 3I_{CE}^- \quad \ldots\ldots\ldots\ldots\ldots\ldots (2\text{-}6)$$

e. Mechanism 5 (Regeneration of dye): At the same time, the oxidized dyes, S+ are shifted to the ground state dye, S caused by the electron obtained from I^- and thus the regenerative cycle is completed.

$$S^+_{adsorbed} + \frac{3}{2}I^- \rightarrow S_{adsorbed} + \frac{1}{2}I_3^- \quad \ldots\ldots\ldots\ldots (2\text{-}7)$$

f. Mechanism 6 (Recombination): Direct recombination of the excited dye that is reflected by the excited state lifetime.

g. Mechanism 7 (Recombination): The next recombination process is the injection of electrons in TiO_2 with oxidized dyes.

$$S^+_{adsorbed} + 2e^-_{(TiO2)} \rightarrow S_{adsorbed} \quad \ldots\ldots\ldots\ldots\ldots\ldots (2\text{-}8)$$

h. Mechanism 8 (Recombination): The recombination of injected electrons in TiO_2 with acceptors in the electrolyte.

$$I_3^- + 2e^-_{(TiO2)} \rightarrow 3I_{anode}^- \quad \ldots\ldots\ldots\ldots\ldots\ldots\ldots\ldots (2\text{-}9)$$

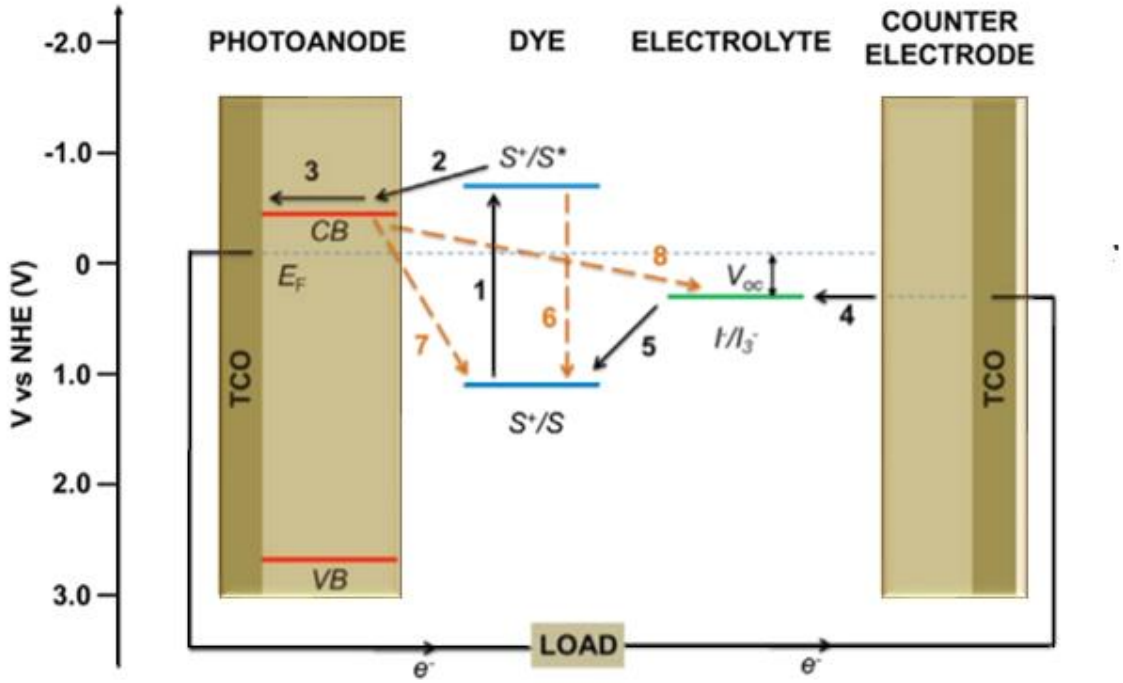

Figure 2.2. Electron transfer mechanisms and energy level diagram of DSSCs [82].

2.4 Nanotechnology in DSSC

The term "nanomaterial" alludes to a wide range of substances have particles with at least one dimension in the nanometer range from 1-100 nm [83]. Nanomaterials are the linked bridge between atoms and microstructures, and the nanostructures are much near to dimensions that are near to atomic dimensions. By comparison, the bond length of between typical carbon atoms, or the spacing between these atoms in a molecule, is within the range of 0.15-0.12 nm [84,85]. Nanotechnology is concerned with NPs, which are aggregates; their size is approximately 100 nanometers. These NPs are altered forms of the basic elements that are created by changing their atomic characteristics [86].

Nanomaterials are essential due to their physical, chemical, and magnetic properties, and the fact that they are inexpensive, safe, and

environmentally friendly. In additions, nanomaterial's have a high surface to volume ratio include NPs, NRs, nano porous frameworks, and other structures. Changing the size of semiconductor NPs is being tried to quickly tune their optical and charge transport capabilities. The chemical features of nano catalysts, such as catalytic activity, may be dramatically altered by increasing the number of surface atoms. By inventing new ways, nanomaterials are being used to increase the efficiency of energy generation.

The optical and electronic properties of nanomaterial, which become strongly size dependent focused attention on the preparation of NP semiconductors [87]. In almost all of these cases, when the particle size is reduced greatly, especially to several nanometer scales, due to the large surface-to-volume ratio, some novel optical properties can be expected [88]. When the size of a material is comparable to- or smaller than its bulk Bohr exciton diameter, its optical property becomes strongly dependent on size due to quantum confinement of electrons and holes [59,89].

The DSSCs are a model system to illustrate the potential of nanomaterial's in studying the electron transfer, electron transport, and electron–hole charge separation and recombination processes. Moreover, nanotechnology can be utilized to provide new materials and fabrication processes, allowing for the production of low-cost DSSC cells with adequate energy conversion potential. DSSC made of traditional material like TiO_2, ZnO and SnO_2 while the nanostructures of these materials will be lighter, cheaper, and more powerful [90]. The DSSC performance can be improved by exposing more dye adsorbed surfaces area to solar radiation and NPs with a higher surface area to volume ratio which lead to increase the solar radiation collection [91].

2.5 Metal oxide Materials for DSSC

DSSC is converts photons energy into electrical energy using semiconductor materials that have the wide band gap energy represented by the difference between the valence band (VB) and CB energies [63]. A DSSC is composed of CE, TCO substrate, a wide semiconductor, dye sensitizers, and an electrolyte. Photoanodes play an important role in deciding the performance of DSSC [92]. Various photoanodes are being employed for both dye and quantum dot sensitized solar cells. A wide band gap nanocrystalline semiconductor oxide film is used as an electron transportation layer in the photoanode of a DSSC [93]. These include mostly the wide band gap semiconductor photoanodes such as TiO_2, ZnO, and SnO_2. Though ZnO has higher electron mobility and has identical band position as TiO_2, due to its instability in acidic dye it is not the preferred choice for commercialization. SnO_2 have also been used as photoanodes in DSSC, though it has higher mobility due to its rapid recombination and poor open circuit voltage, surface treatments were required for SnO_2 to be used as photoanode in DSSC [94,95]. Among the different materials, TiO_2 has a perfect position of CB which is lies lower to the LUMO level of the most of the commonly used organic dyes that lead it to obtain good DSSC efficiency as shown in Figure 2.3 [96]. There are various factors that affect the DSSCs performance, in particular the physical and chemical properties of TiO_2 NPs are the most significant among them [76,22].

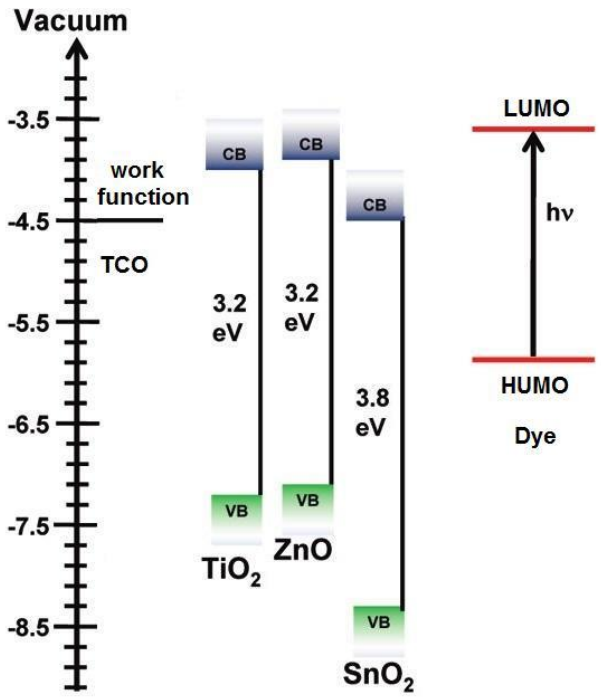

Figure 2.3. Schematic diagram illustrating the energy levels of CB and VB of TiO_2, ZnO, and SnO_2 [96].

2.6 Titanium-Di-Oxide as a photoelectrode

Titanium-Di-Oxide (TiO_2) is one of the most attractive materials in the field of nano-science also in nano-technology because of the potential application of TiO_2 in different processes and it has its extraordinary properties like high stability, low cost, biocompatibility, high chemical inertness, non-toxicity, wide band gap, high refractive index etc. [71,97]. Therefore, it has been already used in the application of efficient photo catalyst for water purification [98], catalyst support [98] , degradation of dyes [5], chemical sensor [7,8], dye sensitized solar cell [99] and optical device [9,10] etc. Furthermore, crystal phase, specific surface area, surface morphology, crystal defect, grain size, and band gap of the absorber material of DSSC play the importance role on the cell performance [98].

As shown in Figure 2.4, TiO_2 exists as one of three mineral phases: anatase, brookite, and rutile. Anatase-phase TiO_2 is the most common phase of TiO_2, but has 3.2 eV Eg, and is therefore weakly active under visible light. Rutile-phase, with a band gap of 3.0 eV, has the strongest visible light absorption, whereas brookite (Eg = 3.3 eV) has the weakest [99]. The use of mixed-phase TiO_2 enhances both the visible light harvesting ability and the electron–hole separation of TiO_2 [100]. The crystalline phase of TiO_2 is highly dependent on its preparation technique

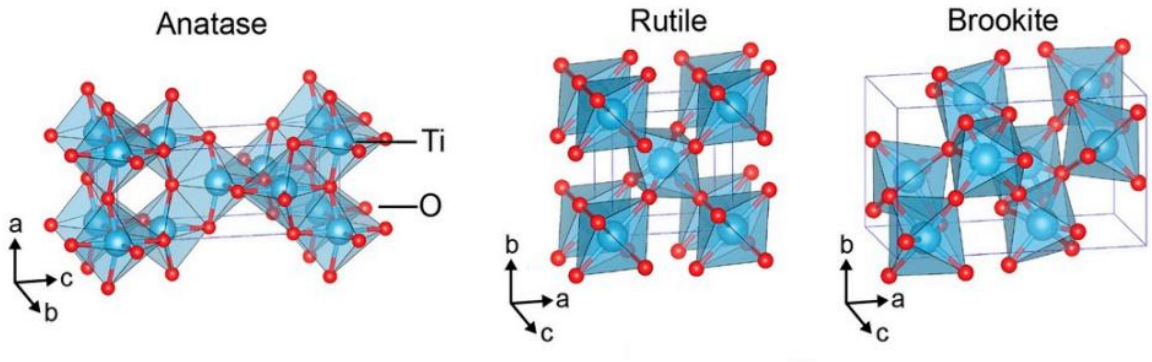

Figure 2.4. Crystal structures of TiO_2 [101].

Rutile- and anatase-phase TiO_2 nanostructures have been most intensively investigated for photocatalysis applications because of their better catalytic activity and easier synthesis. Rutile nanostructure, having a tetragonal phase with lattice parameters a=b=0.459 nm, and c=0.296 nm is obtained with very high crystalline quality. Although the growth direction for 1D nanostructures depends on the growth method used, for rutile TiO_2 NRs, the growth direction is generally the [001] direction. Moreover, the geometric parameters of anatase TiO_2 nanostructure are very close to those of rutile TiO_2 nanostructure, having widths of about 50–200 nm and thicknesses of 20–50 nm [17]. The crystalline structure of anatase TiO_2 nanostructure can also be

assigned to a tetragonal phase, but with different lattice parameters: a = b = 0.3766 nm and c = 0.9486 nm.

2.6.1 Basic Properties of Titanium dioxide

While the differences between the crystalline structure of rutile and anatase TiO_2 nanostructure are tiny, they are sufficient to result in dissimilar electronic structure and optical, mechanical and surface properties. These properties affect the performance of rutile and anatase TiO_2 nanostructure in their multiple applications

2.6.2 Electronic Band Structure

Electronic properties are known to control light absorbance, redox potential, and charge carrier mobility, and consequently to strongly affect the functional properties of semiconductors [19]. Full understanding of the electronic band structures of 1D TiO_2 nanostructures, especially those of TiO_2 nanostructure, is critical for their application in several fields, such as photocatalysis, solar energy conversion or gas sensing. The wide bandgaps of bulk anatase TiO_2 (3.2 eV) and bulk rutile TiO_2 (3.0 eV) are related to the existence of the O 2p and Ti 3d states in VB and CB [20]. The one-dimension TiO_2 nanostructures usually display thickness-dependent bandgaps [103]. When the thickness of TiO_2 nanostructure is less than 2.5 nm, the bandgap is enlarged to a value above that of bulk anatase and bulk rutile TiO_2.

2.6.3 Optical Properties

The light absorption ability of a semiconductor is mainly related to interband electron transitions and is thus controlled by the bandgap.

Excitation of an electron to a point within CB occurs on absorption of a photon with energy equal to the sum of the bandgap energy and the energy within CB, minus the energy of the hole left within VB [28] these electron-hole pairs are those required for a photoreaction in a photocatalyst, or those extracted in a PV device.

2.6.4 Mechanical Properties

One important application of TiO_2 nanostructure is their use as building blocks for fabrication of various micro/nano devices such as various single belt-based sensors or electronics or solar cell. The advantages of TiO_2 nanostructure in this context are ascribed not only to their unique geometry and electronic and optical properties, but also to their excellent mechanical properties. Present studies on the mechanical properties of TiO_2 mainly focus on rutile TiO_2 nanostructure, and few works have reported the mechanical behavior of anatase TiO_2 nanostructure.

2.6.5 Surface Properties

The photocatalytic activity and selectivity strongly depend on surface properties. As an example, the chemical dissociation of water molecules is energetically favored on (001) plane; in contrast, water molecules are preferentially physically adsorbed on (101) plane of TiO_2 [44].

2.7 Zinc Oxide (ZnO)

ZnO is an attractive semiconducting oxide material owing to its large exciton binding energy (60 meV) and wide direct band gap (3.37 eV) at room temperature. As a wide band gap material, ZnO is utilized for highly efficient UV light-emitting devices, optoelectronic devices,

and transparent-conducting electrodes [102]. Owing to its superior physical and chemical properties, it has been widely used in fabricating gas sensors [103,104], light-emitting devices [105], solar cells [18,106,107], and catalysts [108,109], etc. Because of their morphological dependent properties in practical applications, many efforts have been done on the synthesis of ZnO with various morphologies, such as NRs, nanowires, etc. [19,110–112]. In addition, due to the long lifetime of free electrons and holes, ZnO can generate reactive oxygen species on its surface [113]. Furthermore, ZnO is classified to be a generally safe substance by FDA. This nontoxicity and compatibility with skin allow it to be used as an ingredient in sunscreens and cosmetics. Owing to its widespread application in cosmetics, ZnO NPs are produced worldwide in large amounts. According to the recent survey, the global production of ZnO NPs reaches about 550 tons per year [86].

2.8 TiO_2 – Dye Contact

Ruthenium Ru(II) based sensitizers have played a significant role in the development of the solar cells as a chromophore. DSSCs efficiency could be improved significantly if these dyes have absorption in the range of visible to near infra-red (NIR) of the solar spectrum [114]. Researchers have studied various chromophores including metal complexes and organic-based dyes. Among all dyes, Ru(II) polypyridine-based sensitizers, mainly black dye, N3, and N719, are the better chromophores for DSSCs due to their promising chemical and photochemical stability along with enhanced PV performance [23]. N719 Industry Standard Dye (Di-tetrabutylammonium cis-bis (iso-thiocyanato) bis (2,2′-bipyridyl-4,4′-dicarboxylato) ruthenium (II)) is a ruthenium complex dye modified

from the N_3 Foundation dye enabling to increase the device voltage. The Chemical formula of the N719 is $C_{58}H_{86}N_8O_8RuS_2$ as illustrated in Figure 2.5.

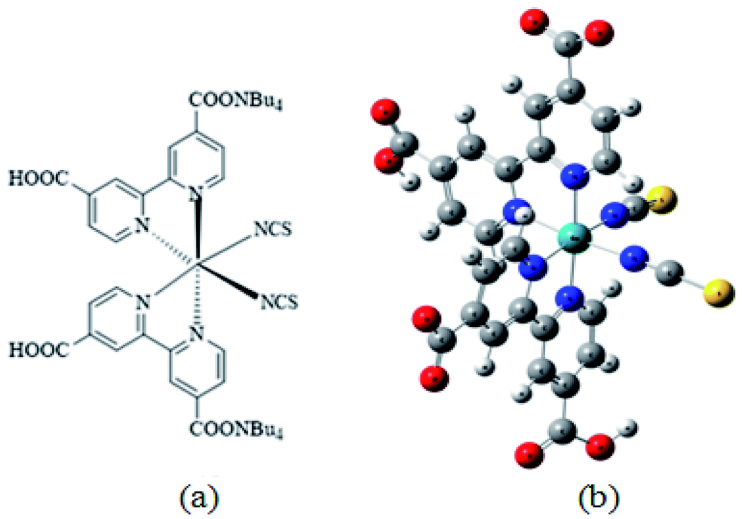

Figure 2.5. The chemical formula of the N719 [115].

The sensitizing dye molecules are attached to the metal oxide surface through chemisorption via the anchoring groups [116]. Indeed, the carboxylate groups provide a strong adsorption of the dye on the metal oxide surface, thus fully justifying by involving valence forces through the exchange of electrons between dye molecules and metal oxide as covalent forces. The various binding mechanisms of the dye molecule with TiO_2 surface are summarized in Figure 2.6 and elaborated as follows:

Figure 2.6.a shows the structure of N719 dye While Figure 2.6.b shows the first type of binding, known as ester type linkage, involves interaction of one or two oxygen atom of -COOH group with the Ti atoms of TiO_2 surface. The second type of binding involves the interaction of both the oxygen atoms of COOH groups with either one Ti or two Ti atoms resulting in bidentate chelating or bridging, as depicted in Figure 2.6 c and d. The third binding mechanism was also

proposed, the N719 dye binding to TiO_2 surface occurs through three carboxylic groups, one of which is attached to two Ti atoms in bidentate form while the other two are bound via monodentate mode as in Figure 2.6.e. Moreover, the fourth binding mechanism Figure 2.6.f, was also proposed where the N719 dye molecules interact with TiO_2 surface though the NCS group in addition to the bidentate bridging. Finally, the fifth binding mechanism proposed that the binding of the dye to TiO_2 occurs through two neighboring carboxylic acid/carboxylate groups via a combination of bidentate-bridging and H-bonding involving a donating group from the N719 dye and acceptor from the Ti-OH group Figure 2.6.g.

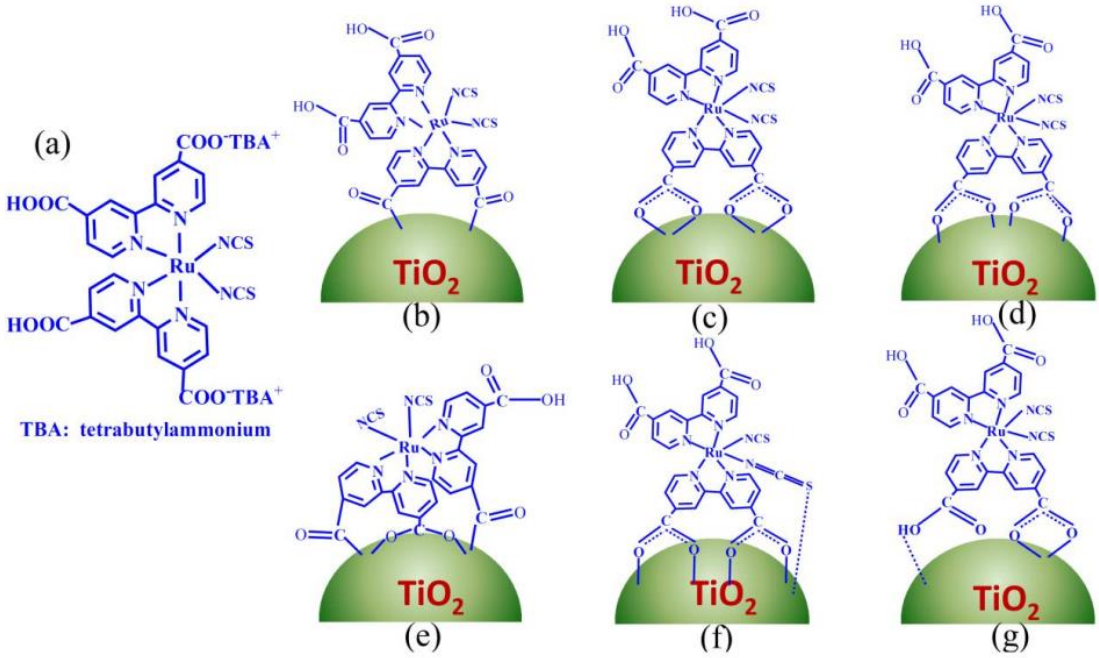

Figure 2.6. N719 dye molecules attached the metal oxide surface [116].

2.9 $TiCl_4$ treatment

A well-known method to improve the performance of solar cells is a post treatment of TiO_2 film in which an extra layer of TiO_2 is grown onto TiO_2 NRs constituting the film [117]. The $TiCl_4$ treatment has

been in use since 1993 when Nazeeruddin et al used it to improve the performance of the relatively impure Degussa P25 TiO_2 NPs [118]. The $TiCl_4$ treatment leads to the deposition of an ultrapure TiO_2 shell (~1 nm) on the mesoporous TiO_2 [119] which may contain impurities or have carbon residue at the surface [120]. Moreover, the different explanations of the working principle of this coating have been reported. These hypotheses concern increased surface area [121], improved electron transport [122], light scattering [71], TiO_2 purity [123], and dye anchoring [37]. Furthermore, the energy of acceptor levels in TiO_2, which can improve the injection efficiency [124]. It also improves electron lifetime significantly, leading to an increase in electron diffusion length [125]. The measurement of solar cell variables depended on the intensity of the current density and voltage (J-V) curve, examples incident photon to current conversion efficiency (IPCE) These variables were used to verify the performance of DSSCs in addition to J_{sc}, V_{oc} and FF, all these variables can be determined by J-V while J_{sc} variable depends on dye amount and chemical composition as well as the electrochemical properties of the thin films used as photoelectrodes for the DSSCs and electrolyte [140] .

2.10 Preparation of Photo-Anode Nanostructure Film

Many experimental works have been done to fabricate 3-D nanostructures and characterize their unique optical properties. In general, the fabrication methods for the arrayed nanostructures can fall into two major categories: top-down and bottom-up approaches [126]. Top-down approaches mainly refer to those that rely on lithographic patterning, or etching materials to shape nanostructures. On the other hand, bottom-up approaches refer to those methods involving growing/assembling nanomaterials from atomic scale. In practice, top-down approaches can be used to fabricate well-defined

nanostructures; however, the fabrication cost is typically high. While, bottom-up growth methods yield diverse nanostructures at relatively low cost, in some cases the shape of the nanostructures can be also well controlled [127–129].

2.10.1 Chemical Technique

In depth knowledge of individual particles and their interaction with other constituents of the system is prerequisite to understand the physico-chemical characteristics of materials. Desired material should have controlled properties with all aspects of size, shape, phase and population control. The chemical technique is one of the most method's that is used for fabricating thin films due to its low cost and simple fabrication. Many chemical techniques were developed to be used for depositing thin films, such as dip coating [131], screen printing [51], spray pyrolysis [132], doctor blade [106], Hydrothermal [133], and spin coating [49]. The chemical deposition methods had a many characteristics or features such as [130]:

a. High temperature or high vacuum equipment is no longer required.
b. The fabrication processes are easy to control and simple.
c. The fabricated thin films give uniform coverage.
d. The substrate shape is no highly restricted and give a big area for films fashioning.
e. Films formation occurs rapidly.

The chemical deposition methods also has same disadvantage like:

a. the fab

2.10.2 Hydrothermal Method

Hydrothermal method is conducted in autoclaves under controlled atmospheric conditions (pressure and temperature). The temperature

raised above 100 ℃ and reaches to saturated vapor pressure. In ceramics industry, this technique is usually used for synthesis of small particles. Many researchers have utilized this method to prepare TiO_2 NRs. The autoclave is placed inside an oven at a temperature that can reach 250°C. Due to the use of autoclave in this method, the temperature of the interaction can increase upon the boiling point of water, amounting to the saturated water vapor pressure. Two temperature regions were created inside the utensil. The material will dissolve in the lower part (hotter part) of the autoclave whereas the saturated aqueous sol is transferred to the upper part (colder part) of the autoclave. Therefore, the crystallization process starts. This method usually uses less temperature than the solid-state reaction. The amount of solution and the temperature that was added to the "autoclave" usually predestine the internal pressure created. The nucleation of nano crystals like (TiO_2, ZnO) is dependent on pH value and sintering temperature. The PH was the main reason of agglomeration and hence decreases of specific surface area. Synthesis PH also affects the size, anatase-rutile transformation and amount of brookite phases [64].

2.10.3 Spin Coating Mechanism

Decades ago, it became easy to obtain regular thin films by means of a spin coating technique [134]. These thin films are manufactured for a wide variety of applications especially in the semiconductor industries. Spin coaters can form thin films with thickness in range of micrometers (μm) and nanometer (nm), for application of devices such as, transistors [135], solar cell [136], gas sensors [137] and light emitting diodes [138]. The most fundamental advantage of spin coating over other methods is the production of fast and high quality films without engaging in complex procedures [139,140].

The spin coating deposition mechanism is done by dropping a certain amount of a specific solution manually or automatically onto the substrate center. The substrate in this machine is fixed with an aspirator. This step is followed by rotating the pile at high speed sometimes up to 10000 rpm with uniform acceleration [141]. After that, the thin film will be successfully formed by evaporation through this process [142]. Thin film made by spin coating technique depends on solution concentration and viscosity as well as rotational speed. Thicker films result from higher concentration. In contrast, thinner films result from higher spinning speeds. In addition, choosing higher solvent volatilities produce thicker films at a specific concentration and viscosity [143]. The following represents the four significant stages that are usually seen in the spin coating process [10,11]. First, before the rotation, few drops of a solution are placed on the substrate as in Figure 2.7.A. Next, by rotating the substrate at high speed, almost all of the solution is flung off the sides Figure 2.7.B. More specifically, centripetal force combined with the surface tension and viscous forces of the solution causes uniform film covering the substrate with the solution. Air flow during the process dries off most of the solvent and the residual solution is formed as a wet-plasticized film Figure 2.7.C. Finally, all the solvent dries out resulted in coating the substrate with the desired material Figure 2.7.D.

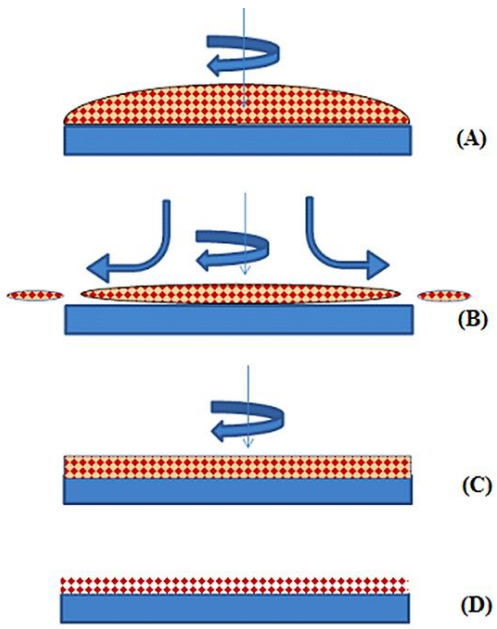

Figure 2.7. The mechanical process of spin coating technique.

Laboratory, before spin coating, the precursor solution must be filtered to remove dust and undissolved particles [105]. In general, the thickness of the spindle film is relative to the square root of rotation speed as in the equation below where (t) is the thickness and (ω) is the angular velocity [134]:

$$t \, \alpha \, \frac{1}{\sqrt{\omega}} \ldots\ldots\ldots\ldots\ldots\ldots (2\text{-}10)$$

This means that the film, which is woven at a rate of four times the speed, will be half its thickness.

2.11 Parameters of Solar Cells

The energy conversion efficiency of a solar cell is an important parameter in the characterization of the solar cell. This is defined as the percentage of power converted (from absorbed light into electrical energy) and collected when a solar cell is connected to an electrical circuit were estimated using J-V curve as shown in Figure 2.8. The overall solar conversion efficiency of DSSC (η) is determined by J_{sc}, V_{oc}, and cell FF, according to the total solar power incident on the cell,

P_{in}, 100 mW/cm^2 for air mass (AM) 1.5. It is given by the expression [146]:

$$\eta = \frac{P_{max}}{P_{in}} = \frac{J_{sc} \cdot V_{oc} \cdot FF}{P_{in}} \quad \text{. . . . . (2-11)}$$

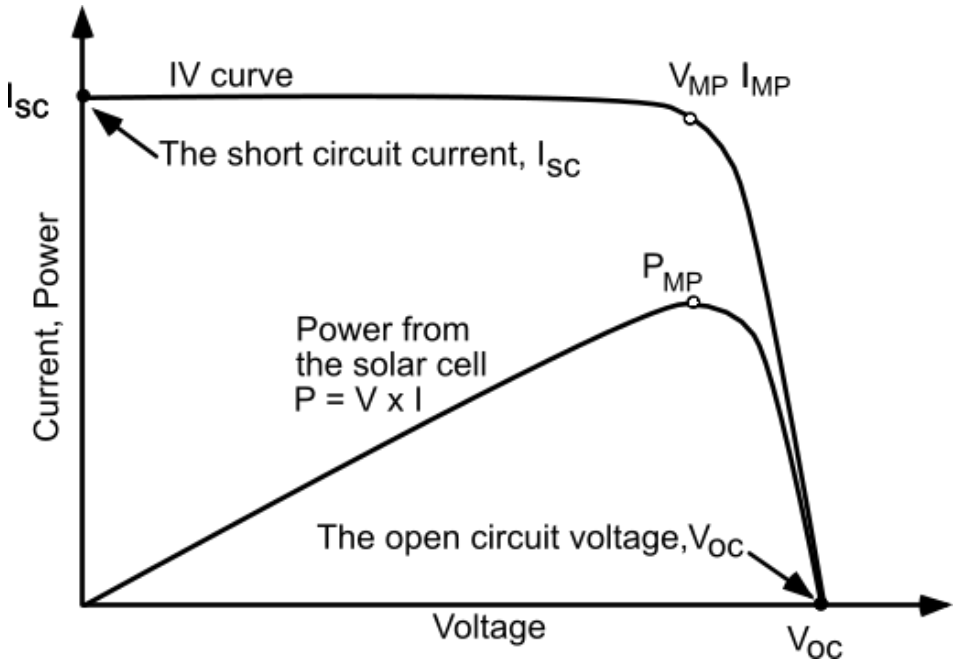

Figure 2.8. J-V curve of the solar cell [147].

2.11.1 Short-Circuit Current Density (J_{sc})

J_{sc} is the maximum current in a solar cell and occurs when the voltage across the device is zero. J_{sc} is used to avoid dependence on the area of the solar cell. There are two ways to improve the short-circuit current. One is to increase the overlap of dye absorption spectrum and solar spectrum. Some groups endeavor to develop dye sensitizers with wider spectra, containing IR or NIR regions [2.5-2.8]. The other method is to increase the absorption surface area of dyes by increasing the thickness of the sensitized nanostructured thin film.

2.11.2 Open-Circuit Voltage (V_{oc})

V_{oc} is the maximum voltage available from a solar cell when no current is drawn from the solar cell. V_{oc} represents the difference between the semiconductor CB thin film (photoelectrode) and the oxidation and reduction potential of the electrolyte.

2.11.3 The Filling Factor (FF)

The meaning of FF can be understood from its graphical representation. It indicates how much area underneath the J−V characteristic curve is filled by the rectangle described by V_mJ_m as shown in Figure 2.8 in relation to the rectangle $V_{oc}I_{sc}$. The theoretically maximum obtainable FF is a function of the open circuit potential, the higher the V_{oc} the higher FF.

$$\mathbf{FF} = \frac{J_m . V_m}{J_{sc} . V_{oc}} \quad \text{. . . . . (2-12)}$$

2.11.4 Parasitic Resistances (R_{sh}) and (R_s)

During operation, the efficiency of solar cells is reduced by the dissipation of power across internal resistances. These parasitic resistances are modeled as a parallel shunt resistance (R_{sh}) and series resistance (R_s), as depicted in Figure 2.9.

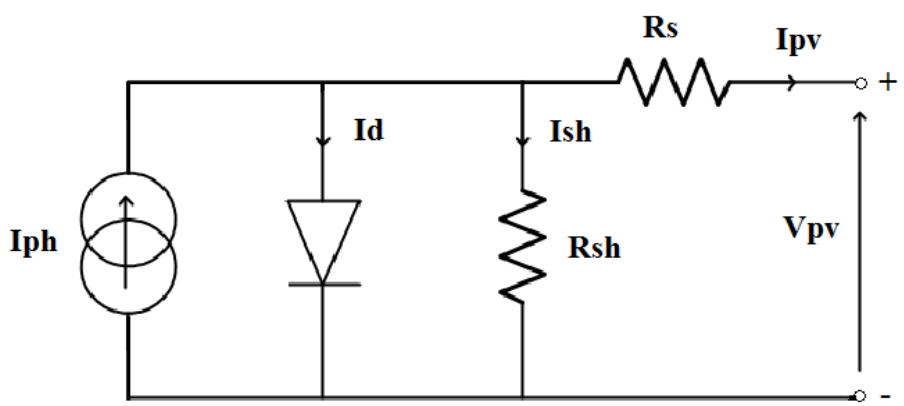

Figure 2.9. Electrical circuit model of a solar cell [148].

The R_s arises from the resistance of the cell material to current flow, particularly through the front surface to the contacts, and from resistive contacts. R_s is a particular problem at high current densities, for instance under concentrated light. Shunt resistance is typically due to manufacturing defects rather than the design of the solar cell. Power losses are a result of low R_{sh}, which provides an alternate current path for the photon-generated current [133,144]. Decreasing R_{sh} and increasing RS will decrease the FF and P_{max} as shown in Figure 2.10. If R_{sh} is decreased too much, V_{oc} will drop while increasing R_S excessively can cause I_{sc} to drop [17,145].

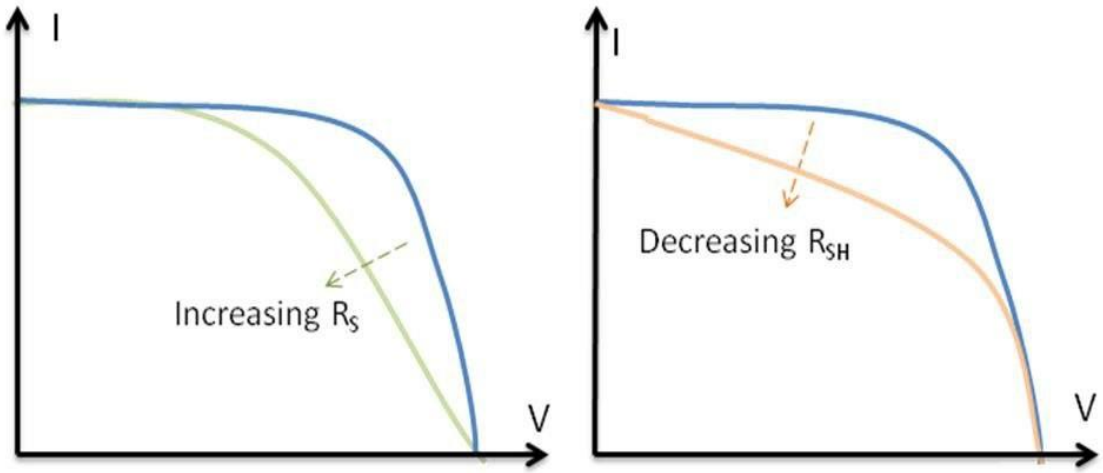

Figure 2.10. Effect of the parasitic resistances R_{sh}, R_s [146].

It is possible to approximate the series and shunt resistances, RS and R_{sh}, from the slopes of the I-V curve at I_{sc} and V_{oc}, respectively. R_{sh} is represented by the slope at I_{sc} while Rs is represented by the slope at V_{oc} [152].

Chapter Three

Experimental Part
(Materials and Equipment)

Chapter Three
Experimental Part (Material and Equipment)

3.1 Introduction

In this chapter, the details of design and construction of equipment: (spin coating, heating unit (electrical furnace), four-point probe device and J-V Characterization instrument). Moreover, producing of the FTO substrate, preparation of Pt films, TiO_2 NRs, MWCNT, ZnO NRs and measuring instruments are introduced. Figure 3.1 displays a flow chart of the experimental part of the present work in which the main are explained.

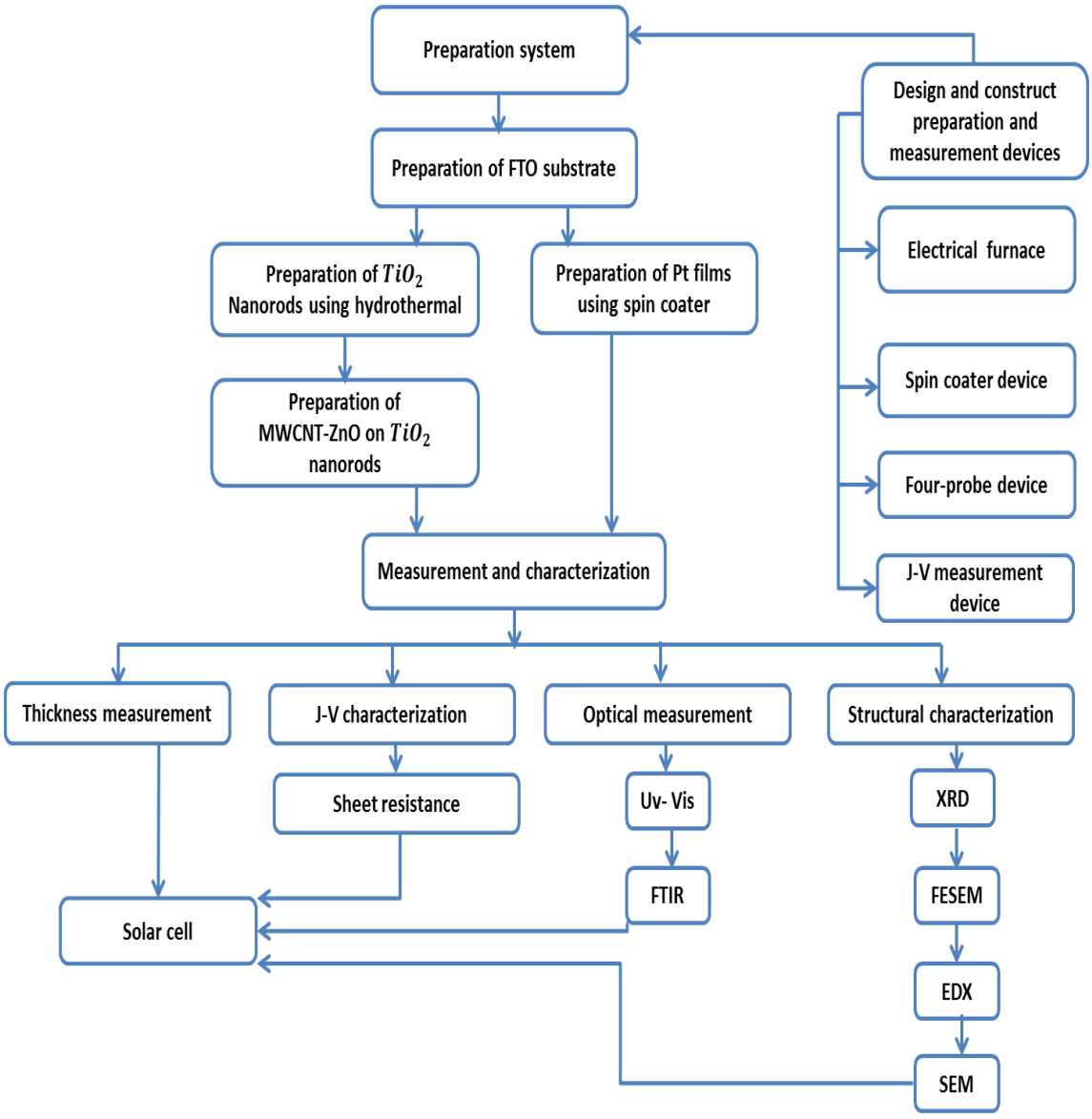

Figure 3.1. Flow chart of the experimental part of the present work.

3.2 The Raw Materials

The materials that used in this synthesis process are listed in Table 3.1. Hexachloroplatinic acid (H_2PtCl_6) utilized as a Platinum precursor material to fabricate the counter electrode. Titanium (IV) butoxide ($Ti(OBu)_4$, 97% Sigma-Aldrich) $Ti(OCH_2CH_2CH_2CH_3)_4$ was used as a TiO_2 precursor material. Zinc-nitrate $Zn(NO_3)_2$ and Zinc-acetate $Zn(CH_3CO_2)_2$ are used to synthesize ZnO NR.

Table 3.1. The raw materials selected for the experiments.

Materials		properties	Brand
Titanium (IV) butoxide		97 % $Ti(OCH_2CH_2CH_2CH_3)_4$	Sigma-Aldrich
FTO		(Sheet resistance~7 Ω) area = 30x30 cm^2	Sigma-Aldrich
Dye N719		$C_{58}H_{86}N_8O_8RuS_2$	Sigma-Aldrich
Platinum source		H_2PtCl_6	Sigma-Aldrich
Electrolyte		HI-30 iodine	Solaronix

Thermoplastic sealing		Meltonix 45 µm	Solaronix
Hydrochloric Acid		HCl 36.5-38	J.T. Baker
Absolute ethanol		CH_3CH_2OH	J.T. Baker
MWCNT	-	Diameter 10-20 nm	*Cheaptubes*
Zinc-nitrate	-	$Zn(NO_3)_2$	-
Zinc-acetate	-	$Zn(CH_3CO_2)_2 \cdot 2H_2O$	-

3.3 Fabrication of Electrical Box Furnace

The heating of prepared samples plays an important role in the industrial production cycle as the most important heating equipment. The electrical furnace is a material heating device that changes the shapes and characteristics of the material [147]. The electrical furnace was constructed (home-made) to anneal the prepared films. This furnace is also used in hydrothermal methods. Iraqi thermostone blocks were used as an isolated material. These blocks were built as a box shape with an empty interior dimension (15×20×40 cm). They were tied together using heat resistant silicon. The internal side of the thermostone was carved to make cavities in the form of channels to install heaters. Electrical quartz heater tubes were fixed in the channels of the furnace and the final design of the cabinet home-made electrical furnace as shown in Figure 3.2. All the heater tubes were connected with electrical switches. The

electrical furnace was controlled by a temperature step controller (GEMO PC109). GEMO PC109 can be controlled the temperature and the rising, stability and decline time as shown in Figure 3.3, where the number of steps is determined by user-programmable parameter codes. Mineral wool was used to cover the built thermostone box. Subsequently, the electrical furnace was placed inside a metal box. The temperature of the fabricated furnace can be raised to 500 degrees in 5 minutes as shown in the temperature profile Figure 3.4. Finally, all materials used are fire-resistant and fire insulation materials. Where the thermostone blocks, mineral wool, and heat resistant silicone were integrated with fire resistance, thermally insulating and heat separating functions. These materials have properties of no bonding formation, good resistance to tensile strength and a fibrous structure when used in a neutral, oxidizing atmosphere.

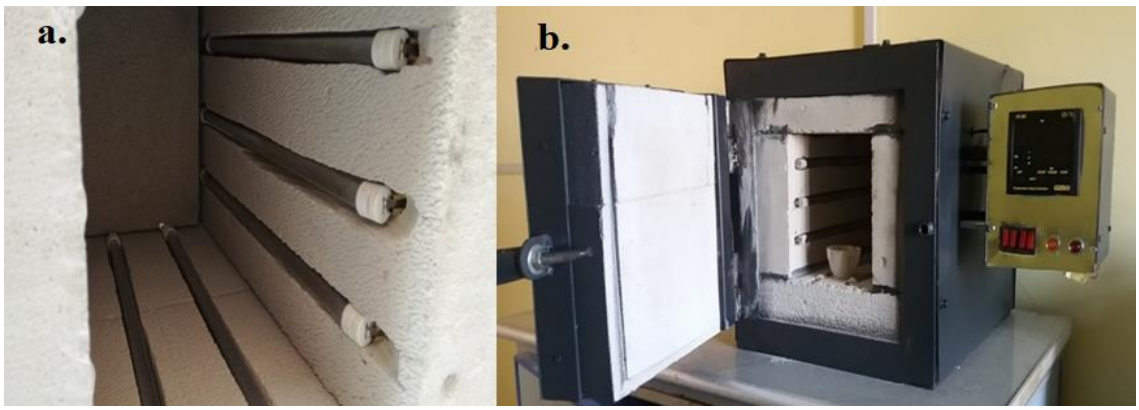

Figure 3.2. Heating unit home-made electrical furnace: a. electrical quartz heater tubes fixed inside the furnace, and b. cabinet fabricated furnace.

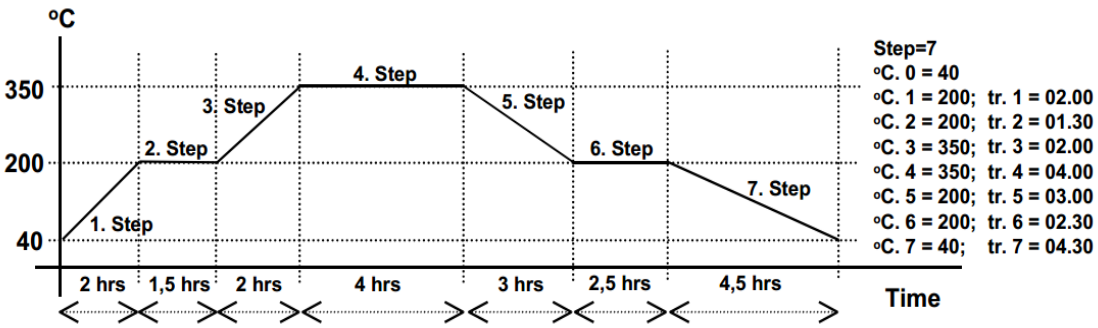

Figure 3.3. Schematic diagrams of the temperature-time steps.

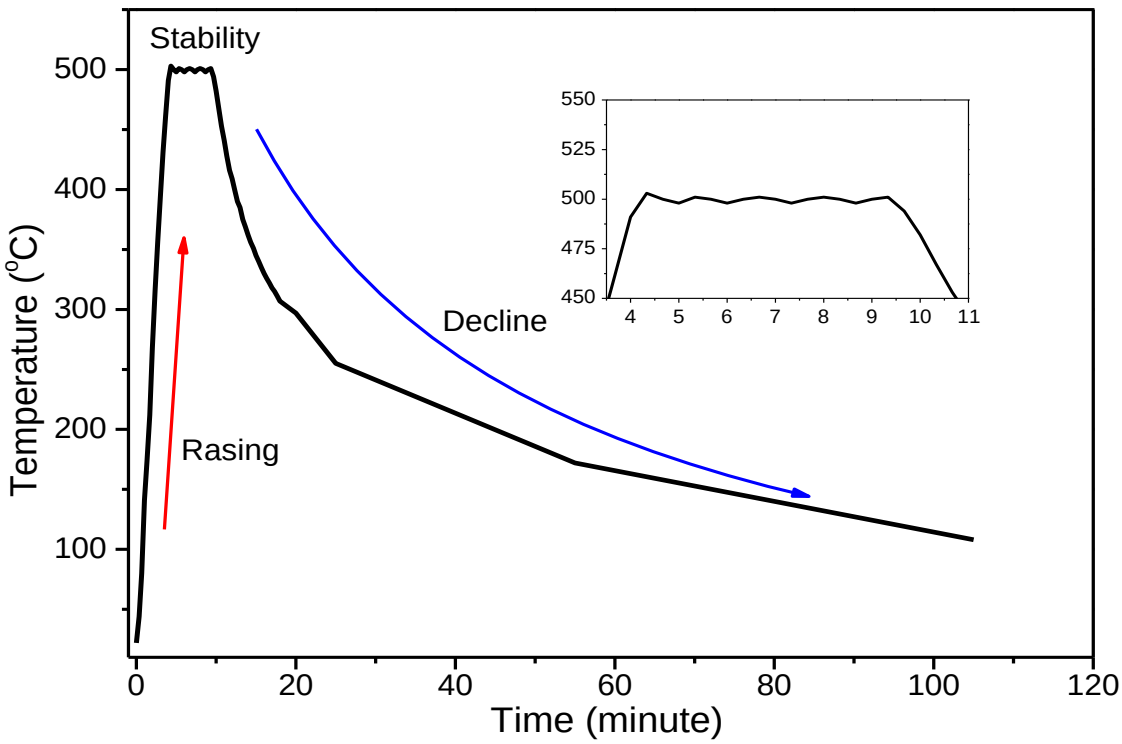

Figure 3.4. Standard curve shows the temperature as a function of time applied on the home-made electrical furnace (experimentally).

3.4 Fabrication of Spin Coater Device

Decades ago, it became easy to obtain regular thin films by means of a spin coating technique [134]. These thin films are manufactured for a wide variety of applications especially in the semiconductor industries. Spin coater device was fabricated to produce thin films of the CE (platinum) and the photoanode (ZnO). The main parts of designing spin coater in this work are hematocrit centrifuge, Arduino UNO, LCD screen, IR sensor and Vacuum rotary.

3.4.1Substrate Holder

Any machine works with nanoscale dimensions must be designed with high accuracy, so it is necessary to calculate the effect of rotation in this work on the thickness and homogeneity of the film [148]. As well, the spin coating machine needs to be free from the vibration effects to obtain films with high

homogeneity, regardless of the number of coating layers. The substrate holder was designed to avoid this problem. Figure 3.5 shows the schematic design of the substrate holder and its parts which will be explained in details. The substrate holder is made from rubber silicon to obtain good adhesion with the sample. Vacuum channel was placed on the motor to allow the air flowing from substrate holder to rotary. A rotary shaft was used for rotating the substrate holder which was sealed by two O-Rings. Finally, the vacuum channel connects with vacuum pump (Value Vi 220SV) by silicone pipe.

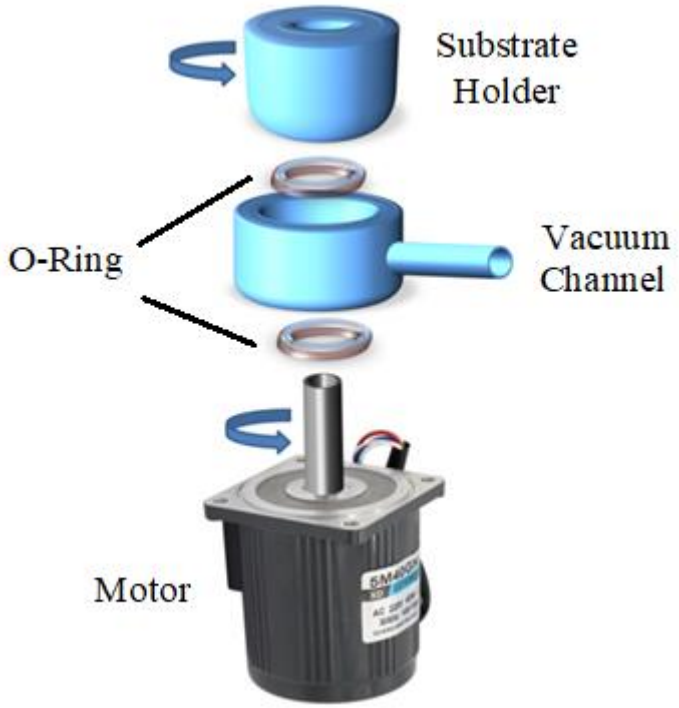

Figure 3.5. 3D design of fabricated spin coater substrate holder, O-ring, vacuum channel and motor.

3.4.2. Speed Controller

Hematocrit Centrifuge (HC – 12 A) has a manual speed rotation controller 0 – 12000 rpm. The crowbar of the manual speed rotation controller placed on variable resistance. The variable resistance was connected with electrical circuit to control the motor speed from 0 to

12000 rpm using single crowbar. The electrical circuit diagram of speed rotation controller is shown in Figure 3.6.

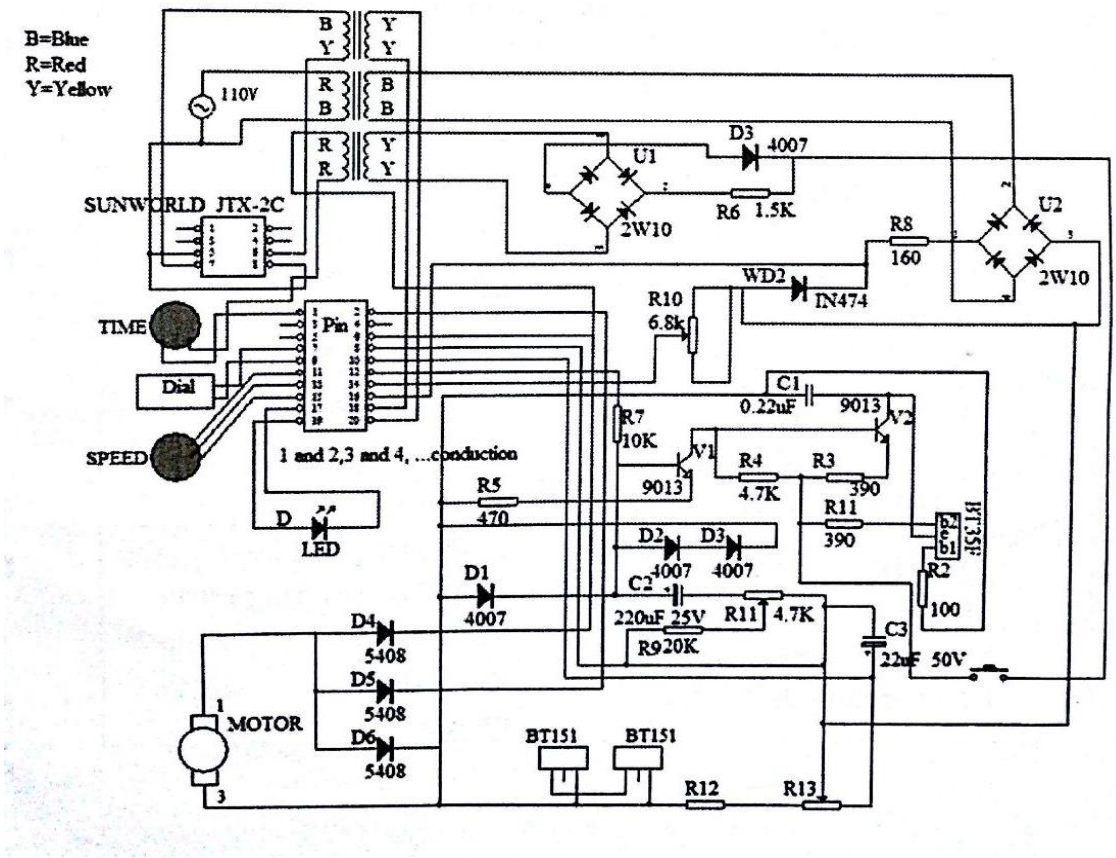

Figure 3.6. The electrical circuit diagram of rotation speed controller.

The Hematocrit Centrifuge provided a simple way to control the speed of the device. Arduino UNO with LCD screen and Infrared Speed Sensor (LM393) are used for observing directly the rotation speed of the device. IR sensor was placed on the motor beside the rotation shaft to sense the rotation speed. Arduino UNO has been programmed to calculate the speed rotation. (16×2) digit LCD display was connected with Arduino UNO and it was placed on the spin coater as shown in Figure 3.7. The final design and the substrate holder of the spin coater machine were shown in Figures 3.8.a and 3.8.b respectively.

Figure 3.7. Front view of the spin coater speed controller.

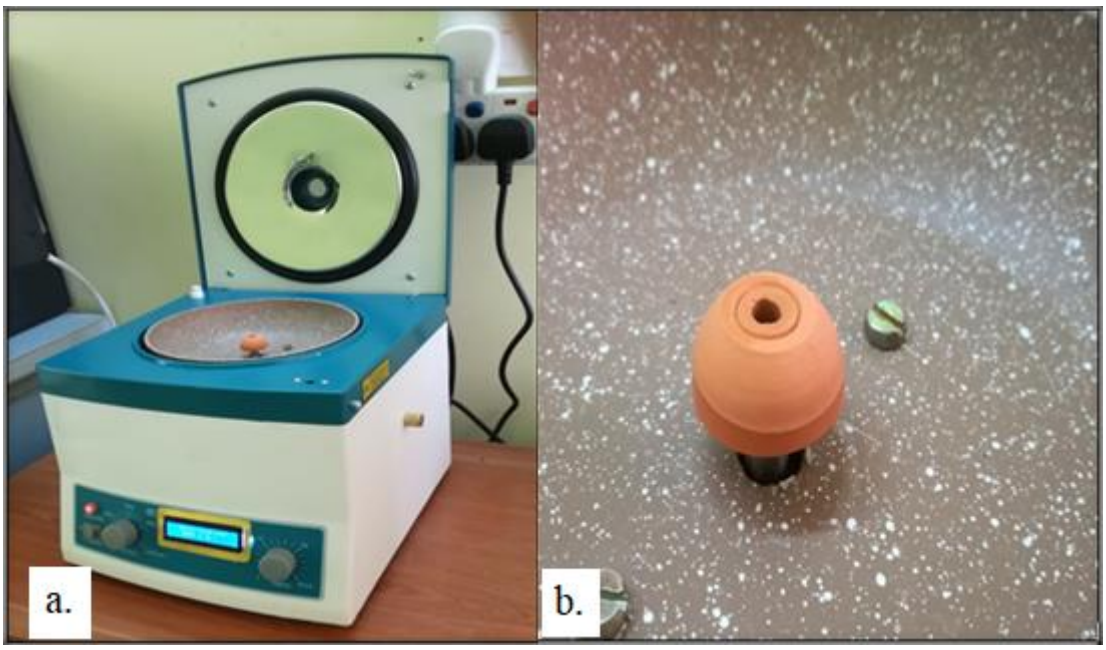

Figure 3.8. a. The final design of the spin coater, and b. substrate holder.

3.5 Substrate Preparation Procedure

3.5.1 Cutting and Cleaning

FTO substrate was used in whole prepared samples. The proper cleaning procedures depend on the nature and kind of the substrate since the thin films and junction properties are greatly influenced by the quality of the substrate surface. The cleaning process is very important to rid the dust and oil from the

surface of the substrate. In addition, FTO substrate cleaning was done in the following steps:

a. FTO substrate is cut into (2 x 2) cm^2.
b. FTO substrates were washed with detergent and a piece of gauze then rinsed many times in distilled water.
c. The ultrasonic was used to clean FTO substrate using alcohol.
d. The substrates were dried by blowing air.

3.5.2 Drilling of the FTO Substrate.

For the purpose of filling the solar cell with an electrolyte solution must make a hole in the cathode substrate. The following steps can be summarizing the drilling of the substrate:

a. Small piece of two face tape is put in the center of the petri dish.
b. Set the FTO substrate on the tape.
c. The conductor face must be kept at the bottom in order to protect it from scratching.
d. Filling the petri dish with water to maintain the substrate from overheating.
e. Use drill with 1mm glass title and put it vertically on the substrate.
f. Turn on the drill with very light compression.

3.6 Counter electrode Preparation.

Chloroplatinic acid hexahydrate H_2PtCl_6 (Platinum ≥ 37.50%) was used as a precursor to synthesis platinum thin films which was purchased from Sigma-Aldrich. FTO substrates with sheet resistances of ~7 Ω/sq were purchased from Sigma Aldrich. The samples were synthesized by chemical reduction in which they were achieved by dissolving H_2PtCl_6 in absolute ethanol to obtain the required thin films.

The precursor H_2PtCl_6 was dissolved in absolute ethanol due to its fast evaporation. Platinum thin films were prepared using a spin coater machine as shown in Figure 3.9. In addition, different parameters were used to verify the optimum conditions of preparation platinum thin film.

Thus, several platinum thin films were coated on FTO substrate as listed in Table 3.2. The first parameter is the rotating speed which was varied from (600 to 3600 rpm); samples PtL and PtS, respectively. In which the other parameters were maintained constant hence the acceleration was (6.28 rad/s^2) and precursor concentration was (15 mM). The second parameter is to control the acceleration hence it was increased from 6.28 to 37.79 rad/s^2 to prepare samples PtS and Pt15, respectively. This experiment was applied by maintain the speed at (3600 rpm) and the solution concentration at (15 mM). The third parameter is controlling the solution concentration which was varied in the range of 15 mM, 10 mM, 5 mM, and 2.5 mM to prepare samples Pt 15, Pt10, Pt5 and Pt2.5, respectively. In which all other parameters were maintained constant speed at 3600 rpm and acceleration 37.79 rad/s^2.

The rising time of the speed (the required time to reach the preferred speed) was maintained at constant value (10 s) for all the prepared samples unless sample (PtS) in which its rising time was (60 s). Each sample was spin coated for 10 min. The coated samples were dried at 373 K by using a hot plate then they were annealed in the fabricated furnace at 723 K for 30 min.

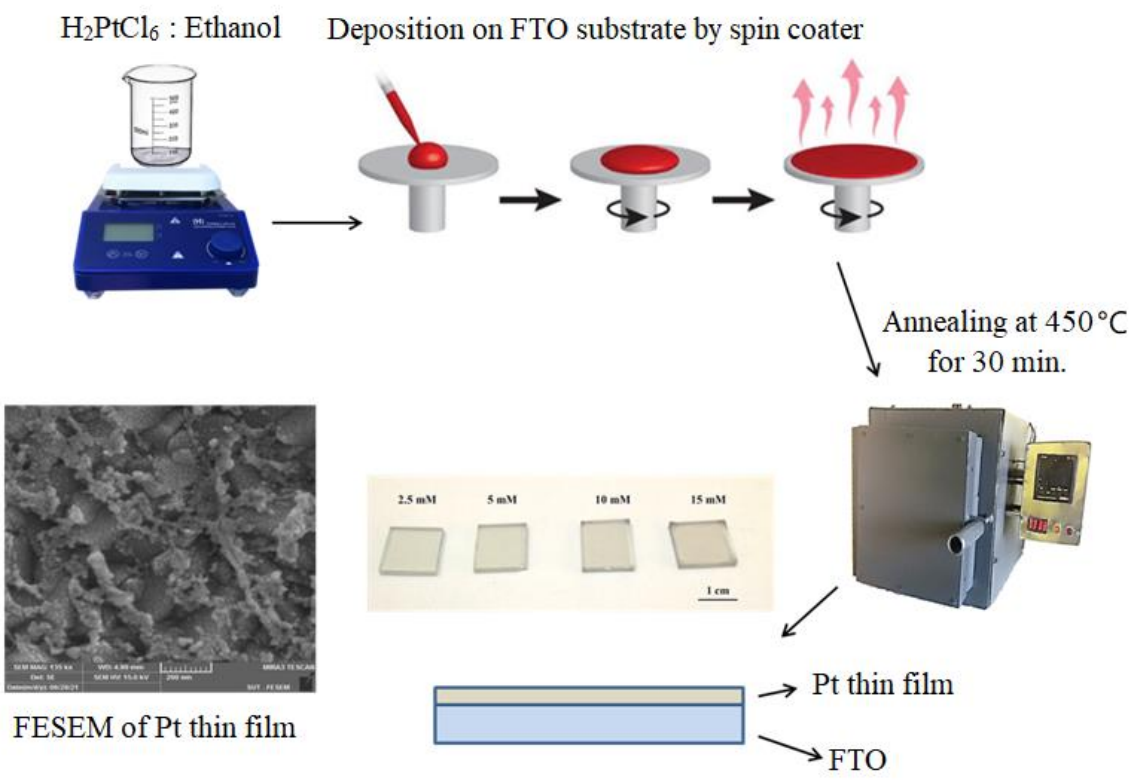

Figure 3.9. Schematic diagram presents the synthesis of Pt thin films

Table 3.2. Fabricated Pt thin films parameters.

Sample	Speed (rpm)	Acceleration (Rad/S^2)	Precursor content (mM)	No. of layers
PtL	600	6.28	15	Single layer
PtS	3600	6.28	15	
Pt15	3600	37.79	15	
Pt10	3600	37.79	10	
Pt5	3600	37.79	5	
Pt2.5	3600	37.79	2.5	
DPt15	3600	37.79	15	Double layers
DPt10	3600	37.79	10	
DPt5	3600	37.79	5	
DPt2.5	3600	37.79	2.5	

3.7 Preparation of photo anode

3.7.1 Preparation of /TiO_2/FTO

TiO_2 NRs were prepared with variation of volume of hydrochloric acid and the etching time using hydrothermal methods. TiO_2 NRs were prepared on FTO substrate using titanium butoxide ($Ti(OBu)_4$) as a precursor (starting material), hydrochloric acid (HCl) as a chelating agent, and DI as a solvent. Chelating agent is ligand that can form bonds (covalent bonding) at more than one point. It is a substance whose molecules can form a several bonds to a single metal ion. Meanwhile, DI acts as a function of adding the oxygen (O_2) element into $Ti(OBu)_4$ for hydrolysis process. First, hydrochloride solvent was prepared by diluting the hydrochloric acid in DI to be 20 ml. Then 0.3 ml titanium butoxide ($Ti(OBu)_4$) was added dropwise into the hydrochloric solvent until the homogeneous mixture was attained. After 20 minutes of stirring the solution will be transparent. The precursor solution was poured into a steel autoclave and followed by placing the FTO substrates vertically into a Teflon-lined stainless-steel autoclave. The autoclave was heated in the furnace maintained at 433K for 5 h. The experimental details were listed in Table 3.3.

Table 3.3. The preparation conditions of TiO_2 NRs.

Sample ID	Structure	HCl to DW ratio	Etching time	
AT	TiO_2/ FTO	7.5DW:12.5 HCL	Overnight	**Ti (OBu) volume for all sample 0.3 ml**
BT	TiO_2/FTO	10DW:10 HCL	Overnight	
DT	TiO_2/FTO	15DW:5 HCL	Overnight	
CT	TiO_2/FTO	12.5DW:7.5 HCL	Overnight	
ET	TiO_2/FTO	12.5DW:7.5 HCL	After 48 H	
FT	TiO_2/FTO	12.5DW:7.5 HCL	After 72 H	

After that, the autoclave was kept into the furnace and cooled down overnight to allow the stainless-steel autoclave to cool and touchable. The prepared samples were rinsed with DI water and left to dry at room temperature. Figure 3.10 summarized the preparation steps of TiO_2/FTO NRs.

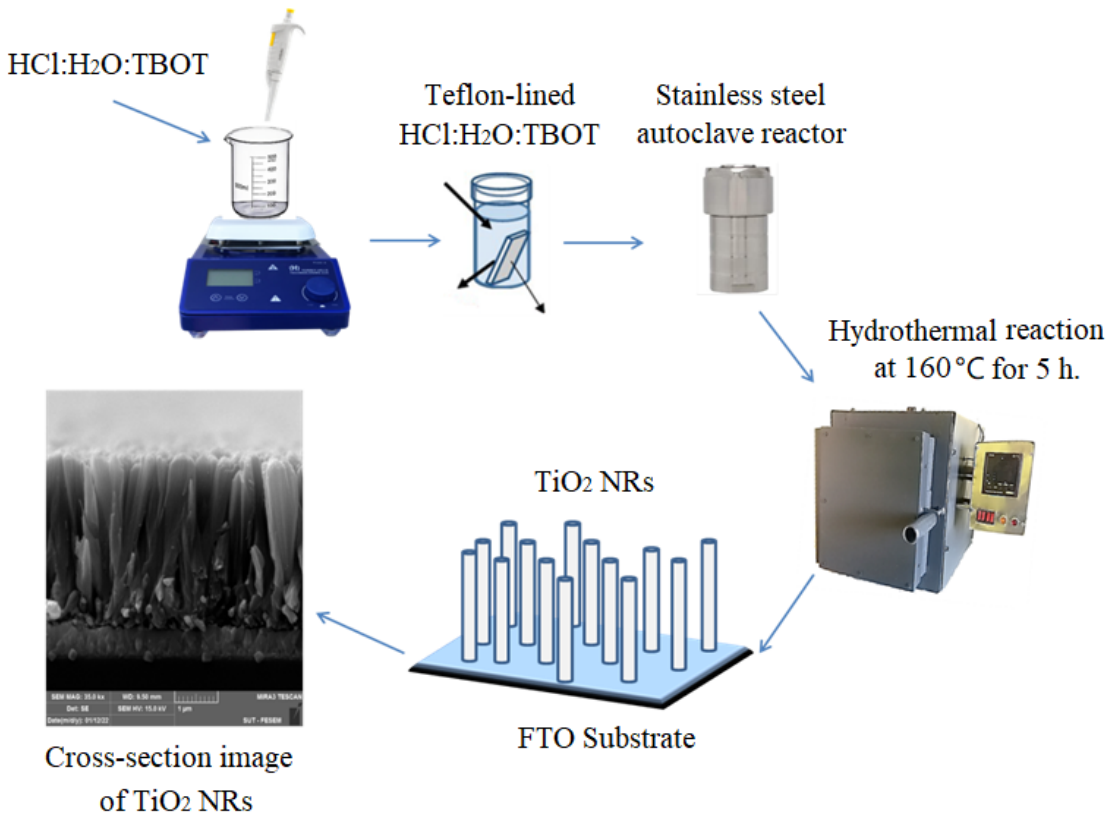

Figure 3.10. Schematic diagram presents the synthesis of TiO_2 NRs.

3.7.2 Functionalization of MWCNTs

The surface of MWCNT was functionalized and opened by oxidation with nitric acid [149]. The usage of the nitric acid in the Functionalization process causes both, purity improvement as well as partial oxidization of carbon. 0.2g of raw-MWCNTs (from CHEABTUBES diameter 10-20 nm) was dispersed in 50mL nitric acid (65% HNO_3) in a flask of 200 ml. The flask was placed in an ultrasonic bath for 60 min at a room temperature to separate the nanotubes aggregations.

Afterward, the mixture was then diluted with 100 mL of distilled water. The treated MWCNTs were washed with distilled water several times until the pH reached 7. Finally, the treated f-MWCNTs were dried at 363K for an overnight.

3.7.3 Preparation of MWCNT-ZnO/TiO_2/FTO

MWCNT and ZnO NRs were synthesized on the sample ET of TiO_2 NR. ZnO NRs were prepared using seed mediated growth method, which comprised two simple steps, namely seeding and growth process. Initially, 0.01 M seed solution was prepared by dissolving zinc acetate [$Zn(COOCH_3)_2 \cdot 2H_2O$] in 40 mL of ethanol under constant stirring at 333K for 2h. Then, TiO_2 NR are coated by ZnO seed layer using spin coater at 3000 rpm for 40 s. MWCNT are insetted into ZnO seed layer with different concentration as listed in Table 3.4.

Subsequently the substrates were heated at 373K for 15 minutes to form a thin layer of ZnO seed solution. The spin coating and heating procedures were repeated twice to achieve the desired thickness of the film. Then the samples were annealed at 623K for 1 h. The formation mechanism of the ZnO NRs can be explained as follows; 0.03M of zinc nitrate hydrate [$Zn(NO_3)_2 \cdot xH_2O$] and hexamethylenetetramine (HMT) ($C_6H_{12}N_4$) were dissolved in DI as an aqueous solutions.

The precursor solution was poured into a steel autoclave and followed by placing the coated substrates with the seed layer vertically into the autoclave. The stainless-steel autoclave was placed inside the furnace. The electrical furnace was maintained at 363K for 2 h. Finally, the samples were removed from the aqueous solution, rinsed with distilled water then left to dry at room temperature.

Table 3.4. The preparation conditions of MWCNT-ZnO/TiO_2.

Sample ID	Structure	MWCNT content	ZnO seed	ZnO
ETZ1	ZnO/TiO_2	0	zinc acetate concentration 10 mM	Zinc-nitrite concentration 30 mM
ETZ2	MWCNT-ZnO/TiO_2	0.5		
ETZ3	MWCNT-ZnO/TiO_2	1		
ETZ4	MWCNT-ZnO/TiO_2	1.5		

3.8 Fabrication of DSSCs Sample

3.8.1 $TiCl_4$ Treatments

The prepared photo anodes (TiO_2 and MWCNT-ZnO/TiO_2 nanostructure) were immersed in a 40 mM aqueous $TiCl_4$ solution at ice-cooled conditions for 30 min. Subsequently, the samples were washed with distilled water and rinsed with ethanol to remove any excess of $TiCl_4$ and finally dried. Then, the dried samples were annealed again at 673K for 20 min to crystallize attached NPs.

3.8.2 Dye Loading

Before solar cell fabrication, the prepared photo anodes (TiO_2 and MWCNT-ZnO/TiO_2 nanostructure) were immersed in 0.3 mM N-719 ($C_{58}H_{86}N_8O_8RuS_2$) dye solution for 24 h at room temperature. N-719 dye solution was synthesized by dissolved the dye powder in ethanol.

3.8.3 Cell Fabrication

The working electrode and CE were sealed using a film (Meltonix 45 µm hot melt foil from Solaronix). (Meltonix is an ionomer with a melting point of about 373K. The thickness of the foil

used in a standard DSSC was 45 µm. After putting Meltonix on top of the working electrode, CE was put onto the working electrode like a sandwich. Then the cell was exposed to heat using a hotplate at 110 ℃. The preparation process and the final shape of the DSSC cell are shown in Figure 3.11.

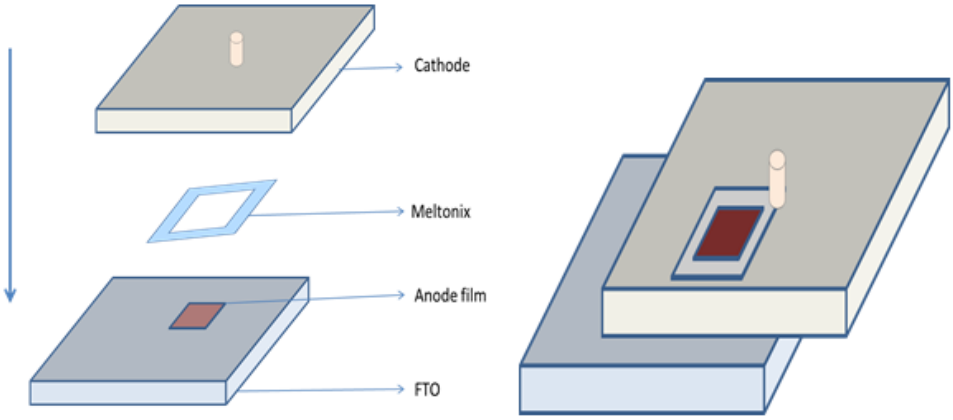

Figure 3.11. The preparation process and the final shape design of the DSSC.

3.8.3 Electrolyte Injection

After the sealing process, a small drop of electrolyte (Iodolyte HI-30) was injected into the groove. A Laboratory syringe was designed as in Figure 3.12 to evacuate the solar cell from the air and inject the electrolyte due to the pressure difference. Then the holes were closed using a piece of Meltonix foil. Figure 3.13 summarized the injection step of the electrolyte solution into the fabricated cell.

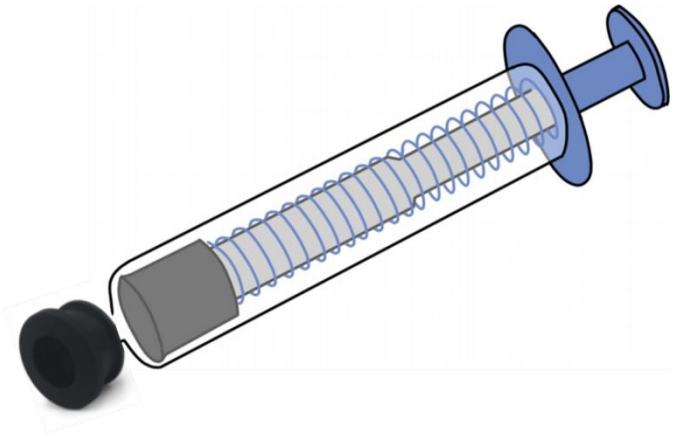

Figure 3.12. The designed Laboratory syringe.

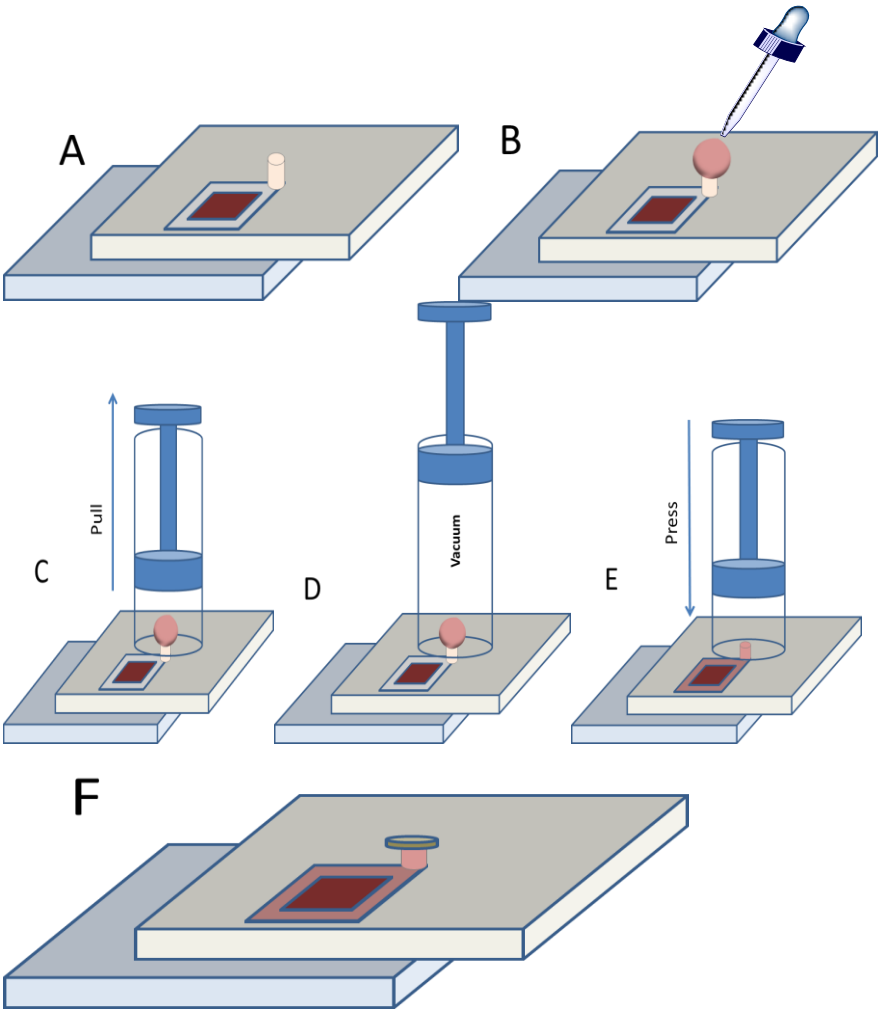

Figure 3.13. Schematic diagram of the electrolyte injection steps.

3.9. Measurements and Characterization

Different measurements were used to study the characterization of fabricated samples which can be classified into the main fields of the material properties such as (structural, optical, morphological, and optoelectronic). They include thickness measurements, x-ray diffraction (XRD) pattern, Energy-dispersive X-ray spectroscopy (EDX), field-emission scanning electron microscopy (FE-SEM), UV-Visible spectrum, sheet resistance, J-V characteristics and finally the characterization of the fabricated devices.

3.9.1. X-ray diffraction (XRD) analysis

The crystallographic information of all samples was investigated by XRD analysis technique. The structure of the TiO_2 and MWCNT-ZnO/TiO_2 nanostructure grown on FTO substrates have been examined using (Philips PW1730) X-ray diffractometer system. The intensity of the X-ray was recorded as a function of Bragg's angle of the samples. The source of radiation was cu (k_α) with wavelength λ=1.5406 Å, the current was 30mA and the voltage was 40 KV. The scanning angle 2θ was varied in the range of (9.8-80) degree with speed of (0.05) deg. /min. Moreover, the measurement temperature is 300K. X'Pert High-Score Plus software was used to match the peaks of the synthesized samples (TiO_2/FTO and MWCNT-ZnO/TiO_2/FTO) with the stander values JCPDS card. In addition, the interplanar distance d_{hkl} for different planes was determined using Bragg's law [150]:

$$n\lambda = 2d\sin\theta \quad \text{(3-3)}$$

Where n is the reflection order.

While, the average crystallite size of the prepared NPs can be estimated by the Scherrer formula using the full width at half-maximum (FWHM) value of the XRD diffraction peaks [151]:

$$D = \frac{0.9\,\lambda}{\beta cos\theta} \quad (3\text{-}4)$$

Where *D*, *λ*, *θ* and *β* are the crystallite size, X-ray wavelength, Bragg diffraction angle, and the parameter (*β*) is the peak FWHM.

3.9.2. Field emission scanning electron microscopy (FESEM)

A typical scanning electron microscope (FE-SEM) type (TESCAN $MIRA_3$) with different components was used. Scanning electron microscopy is basically a type of electron microscope. It is a technique where an image of a sample is created by scanning it with a beam of electrons. When the electron beam interacts with the atoms on the surface of the sample giving information about surface topography and composition will be provided [152]. Moreover, SEM was used for various purposes such as study the morphology properties, chemical composition, elemental mapping and determination of the particle size distribution on the surface of the sample. The morphology of the prepared samples was characterized using a field-emission scanning electron microscope. All samples were coated by gold using sputtering method before being imaged to avoid the effects of charge accumulation [153,154]. The morphological features were observed by taking top-view images. Furthermore, the side-view was carried out through the image of a cross-section where the samples were vertically broken to obtain the cross-sectional view directly.

3.9.3. Energy-dispersive X-ray spectroscopy (EDX)

EDX is a technique used for elemental and compositional analysis based on the energy spectra of the characteristic X-rays generated by electron beam irradiation. EDX is an optional instrument that often is attached to scanning electron microscopes (SEM). TESCAN $MIRA_3$ FESEM has a Thermo scientific EDX system. EDX is useful to measure the elemental composition of samples. The homogeneity, elemental distribution and changes in composition are obtained using the Pinnacle analytical software package.

3.9.4 Film Thickness measurement

The thickness of prepared samples thin films was measured by using SEM technique. TESCAN $MIRA_3$ was also used to obtain the side view of the sample where the prepared samples are mechanically broken to obtain the cross-sectional view directly. The thickness of the samples was carried out through the image of the cross-section using Image J software.

3.9.5. UV-Vis Spectroscopy

UV-Vis absorption spectroscopy is a simple technique to measure and characterize the optical properties of materials in liquid or film form, including their transmittance, absorbance, and reflectance. UV-Vis spectroscopy can provide useful qualitative or quantitative information regarding the optical parameters of the materials through analysis of the spectra obtained from measuring the light intensity as a function of wavelength. Shimadzu UV-Vis-1900i that used to measure the optical absorbance spectra of the synthesized samples (TiO_2/FTO and MWCNT-ZnO/TiO_2/FTO) film within the wavelength ranging

from (190-1100 nm) at room temperature. The optical Eg of the prepared samples was determined using the Tauc plots for allowed direct transition, by plotting $(\alpha h\upsilon)^2$ against the photon energy and best fit line intersects the energy photon axis at $(\alpha h\upsilon)^2$ equal to zero which represents the values of optical energy gap [89,155,156]. The direct transition in general occurs between top of VB and bottom of CB (vertical transition) at the same wave vector $\Delta k = 0$ for conservation of momentum [157]. The allowed direct transition refers is described by the following relation [158]:

$$\alpha h\nu = B(h\nu - E_g)^{1/2} \quad \text{..... (3-5)}$$

Where B is constant inversely proportional to amorphusity.

If the transition occurs also between states of the same wave vector, but the wave vector does not equal to zero, the transition is called forbidden direct transition, it obeys the following relation [159]:

$$\alpha h\nu = B(h\nu - E_g)^{3/2} \quad \text{.....(3-6)}$$

3.9.6 Sheet resistance

Sheet resistance is an important technology to monitor the electrodes or conductive surfaces of the dye-sensitized solar cell to avoid resistance rising [160]. Sheet resistance of CE Pt/FTO films were estimated using four-point probe technique. A home-made four-probe device has been fabricated using the Nokia N8 motherboard as shown in Figure 3.14. This motherboard has a four-metal probe with a spring and spherical head. The spherical shape of the tip provides a large contact surface area and protects thin films from scratch. The outer radius of each probe is 0.35 mm with an average spring force of 0.75 N.

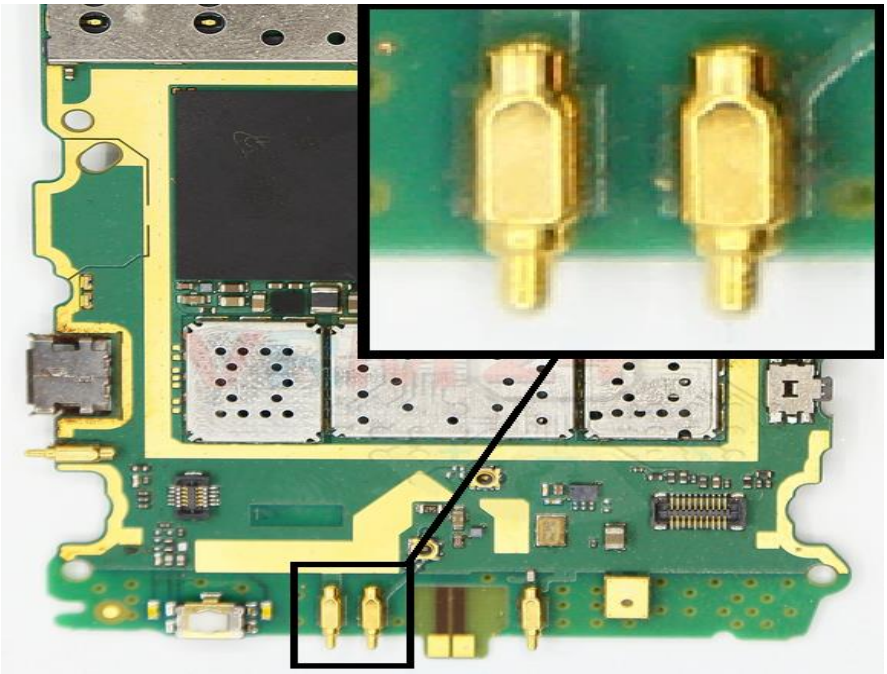

Figure 3.14. The selected part of probes in the mobile motherboard (Nokia N8).

The four-metal probes were separated from their original motherboard and located at a straight alignment. The separated space between each two successive adjacent probes is equal to 1.8 mm as shown in Figure 3.15. The final design of the four-point probe device is connected to Keithley 2450, as shown in Figure 3.16.

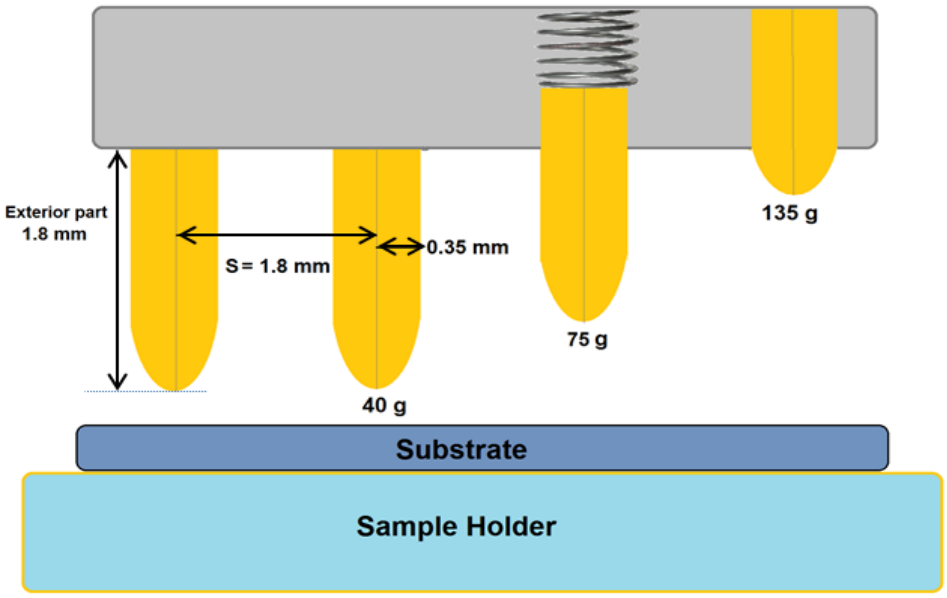

Figure 3.15. Schematic diagram of the four-point probe device.

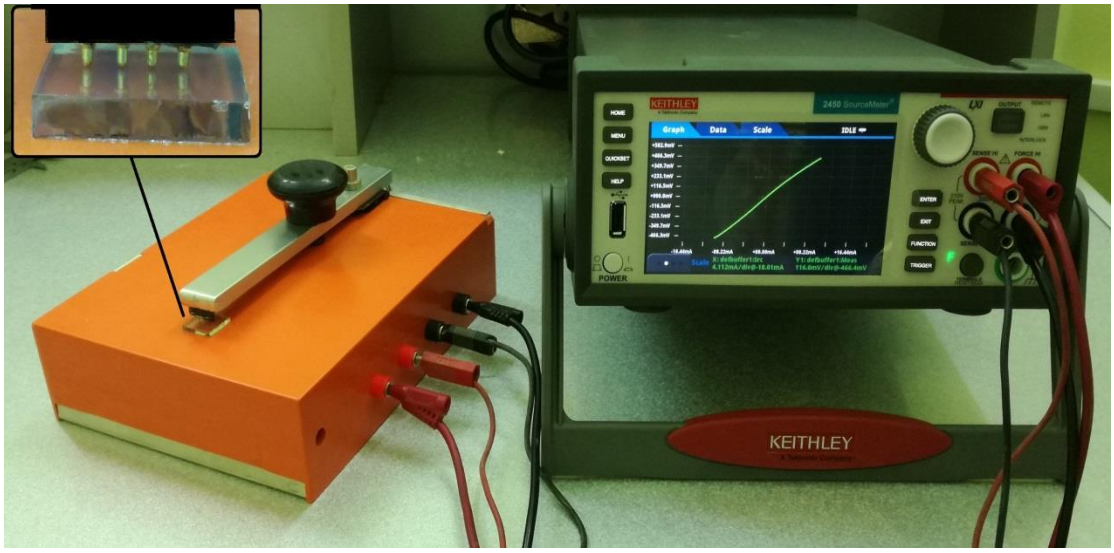

Figure 3.16. Four-point probe device connected with Keithley 2450.

In order to obtain the surface resistance, the four-point probe device with collinear arrays contacted a sample surface as shown in figure 3.17. The current is applied through two of the outer probes (1 and 4) and then measuring a voltage from the inner two probes (2 and 3). The I-V curve has been used to determine the four probe resistance of the sample from the slope of the resulting data [166], or directly given by Ohm's law R=V/I [167].

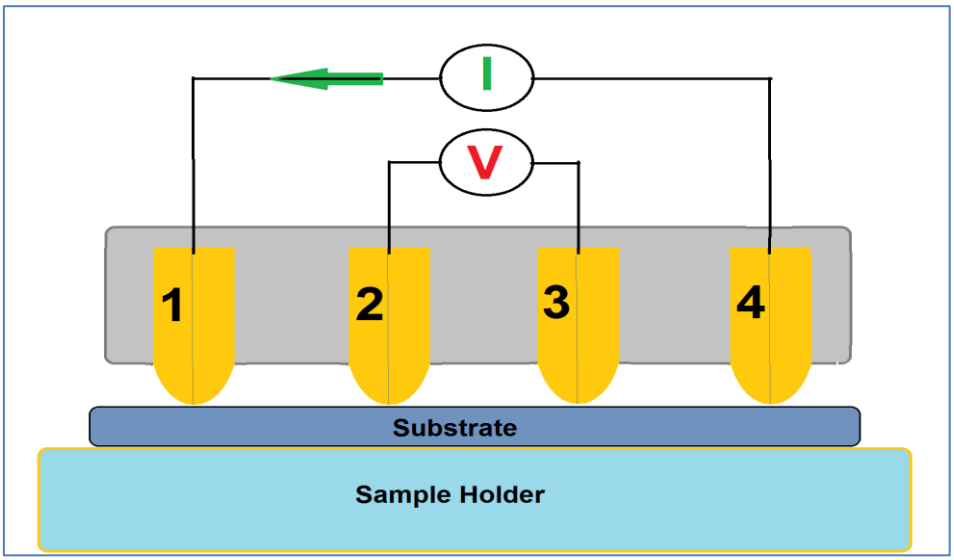

Figure 3.17. Schematic diagram of the collinear four point probe circuit

Equation (3.7) can be used to estimate the surface or sheet resistance [168–170]. Where Ks is the geometrical correction factor as shown in equation (3.8) [169].

$$RS = (V/I) * Ks \quad \ldots\ldots\ldots\ldots\ldots\ldots\ldots\ldots\ldots 3.7$$

$$Ks = F(D/S) * F(t/S) * F(T) * F(S) \quad \ldots\ldots\ldots\ldots 3.8$$

As see in equation 3.8 the geometrical correction factor Ks depending on four main factors. These factors can be described as a following:

1. F(D/S) is the correction factor based on the ratio of the probe to substrate diameter (D). were described and computed by J. Kang [169].
2. F(t/S) is the correction factor depending on the sample thickness and probe spacing (S). Furthermore, for thin films (t << S) therefore F(t/S) is equal to one.
3. F(T) is the temperature correction factor where it is computed using equation 3.9 [169].

$$F(T) = 1 - CT\,(T - 23) \quad \ldots\ldots\ldots\ldots\ldots\ldots 3.9$$

Where F(T) is equal to one at (23.0 ±0.5°C).

4. F(S) is the probe spacing correction factor given by equation (5) [171].

3.9.7 J-V Characteristics.

Current density-voltage (J-V) measurement under illumination is an important conventional measurement to quantitatively evaluate the efficiency of solar cells. The PV performance of the solar cells can be illustrated by a J-V curve. J-V characteristics of the DSSCs were measured under simulated AM 1.5 sunlight at a light intensity of 100 mW/cm^2. Xenon lamp was used as light source to simulate the standard AM 1.5 sunlight. The light intensity was calibrated using Solar Power Meter (SM206). J-V are measured using keithley 2450. This keithley is programmed to measure and plot the (J-V) curve automatically. J-V measurement system that used to measure the efficiency of fabricated solar cells is shown in Figure 3.18.

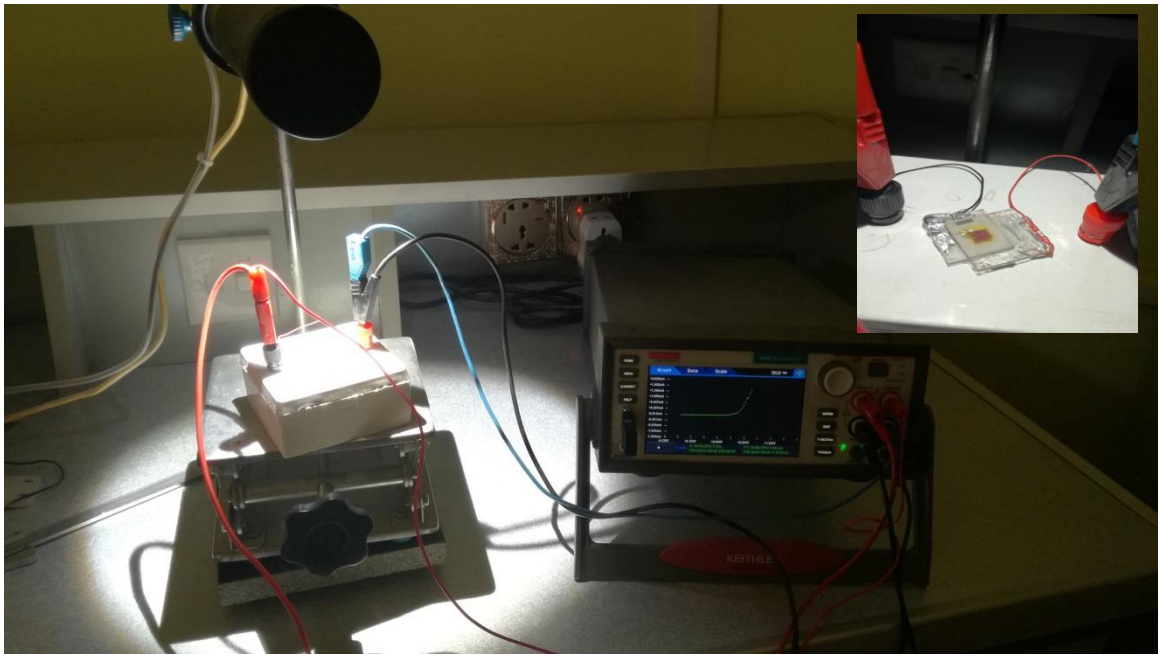

Figure 3.18. Photographs of Current density-voltage (J-V) measurement system.

Chapter Four

Results and Discussions

Chapter Four
Results and Discussions

4.1 Introduction

This chapter includes the results and the analyses of the experimental measurement, for the components of DSSC; photo electrode and a counter electrode. The morphological, and optical properties of the synthesized films were characterized by XRD, FESEM, EDX, and UV-Vis spectrum. Finally, the PV properties from J-V measurement and calculation efficiencies for several devices of dye sensitized solar cells will be presented and discussed.

4.2 Characterization Pt/FTO CE

Platinized counter electrodes were fabricated by depositing Pt thin films on conducting glass sheets (FTO) using spin coating device. Many factors will be studied such as speed and acceleration effect of the spin coating device, the effective of precursor concentrations H_2PtCl_6 and the produced layers on the physical properties of the Pt Films. Different parameters were used to prepare several platinum thin films which were coated on FTO substrate using a spin coater machine as listed in Table 3.2.

4.2.1 Speed and Acceleration Effect

Homogeneous thin films made by spin coater require a balance between rotational speed, acceleration, viscosity and other factors. To clarify the working mechanism of the machine, an aspirator is employed for the purpose of locating the substrate. Then, by rotating the plate, the chemical solution is uniformly spread over the entire surface of the substrate. In this work, the effect of rotation speed was studied. Thus, the thickness of the thin film can be reduced by controlling the rotation speed where high speed leads to thinner layers. The effects of the rotation speed and acceleration on platinum thin films are shown in Figure 4.1. Non-homogeneous thin film was produced at low

speed (600 rpm) as demonstrated in sample (PtL) Figure 4.1.a. A circle thin film was concentrated on the middle of the FTO substrate. This is due to low speed which leads to evaporate the solvent (Ethanol) before distributing the solution completely on the entire substrate surface. As well, sample (PtS) was exhibited nonhomogeneous thin film when prepared at high speed (3600 rpm) and low acceleration. A ring like Pt thin film was concerted on the center of the substrate. This is due to high speed with low acceleration which provided enough time for the precursor to evaporate before distributing the Pt uniformly. The perfect concurrence between the speed and acceleration is shown in sample (Pt15) where homogeneous thin film was obtained. These conditions afford the precursor to well distribute on the substrate before evaporating.

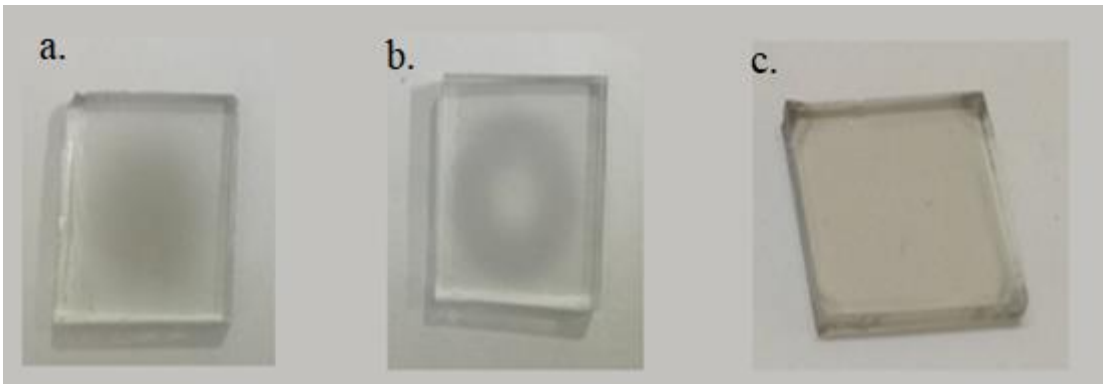

Figure 4.1. Pt/FTO photographs of: a. (PtL), b. (PtS), and c. (Pt15).

Figure 4.2 represents the modeling shapes that show the effectiveness of speed and acceleration on the platinum thin films distribution. When manufacturing a spin coating machine, the factors that determine the optical and physical properties of the film must be taken into consideration. One of the factors affecting the properties of coated thin films is the acceleration factor, in addition to the final rotational speed. As for the thickness of the film, it is also affected by the nature of the used resin according to the percentage of solid matter within the polymer, surface tension (the tendency of liquid surfaces), viscosity, drying rate at the beginning and during rotation and others. It is worth noting that thickness is often inversely proportional to speed and rotation

time. Approximately 50% of the solvent composed of the resin is lost at the beginning of the rotation due to evaporation. Therefore, it is important to control the rotational acceleration in a controlled and safe manner [141,161]. Moreover, the uniform shade of the resin over the topographical properties of the substrate determines the topography of the product, as the substrate sometimes retains the topographical properties during the operation of the machine. Because of the rapid rotation, radial forces are generated that disperse the resin around the terrain. Thus, in some cases, even small parts of the substrate are blocked from the liquid [161].

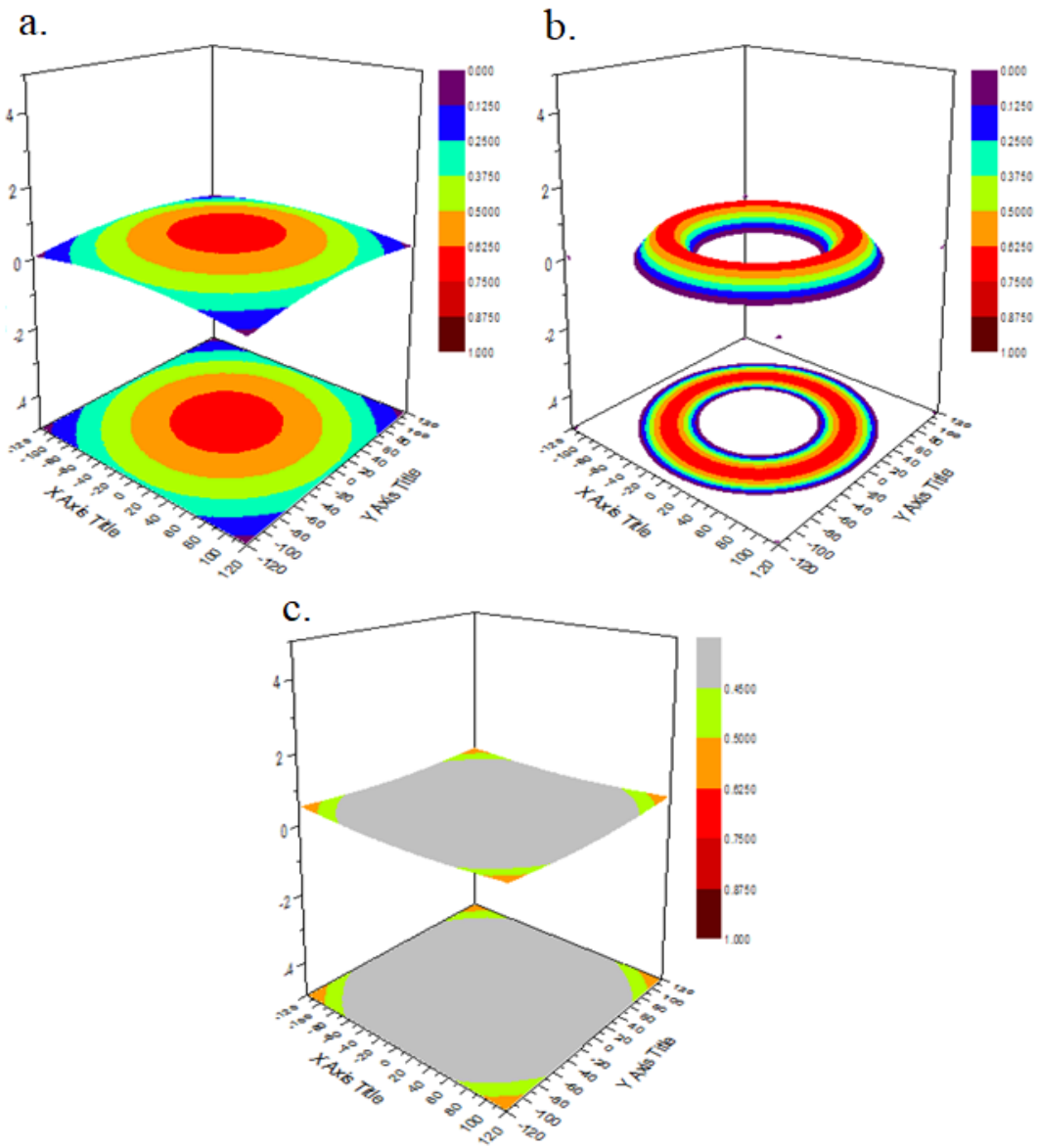

Figure 4.2. Distribution of platinum thin films: a. PtL, b. PtS , and c.Pt15 .

4.2.2 Morphological properties

A- One layer of Pt film

Figure 4.3 shows the prepared thin films using the spin coating machine with four platinum acid concentrations of Pt/FTO NPs, which are 2.5, 5, 10 and 15 mM. The Figure shows that the prepared Pt/FTO exhibited clear thin film at low concentration while by increasing the concentration a foggy film was obtained.

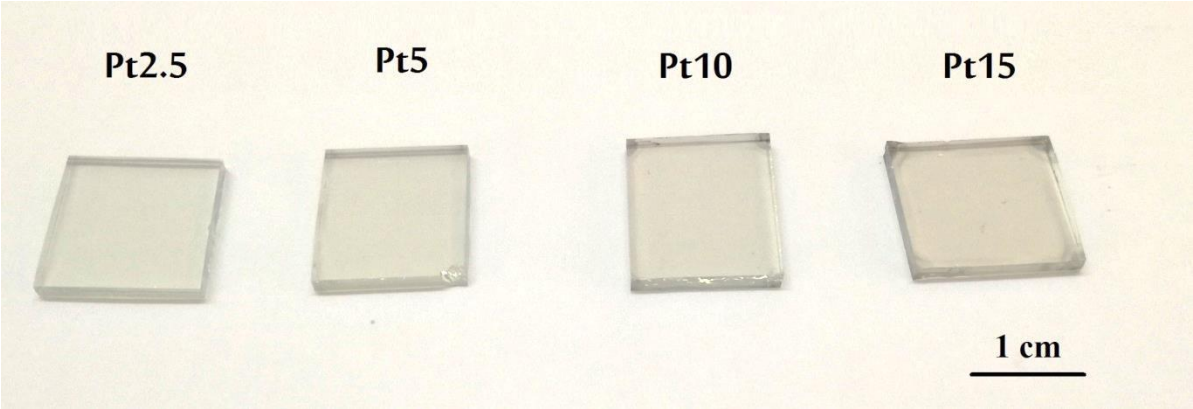

Figure 4.3. Pictures of single layer Pt/FTO thin films with different precursor concentration.

Figure 4.4 shows the FESEM photographs of bare FTO and Pt/FTO at the above precursor concentrations. It is evident that platinum nano particles (Pt-NPs) are homogeneously distributed on the FTO. It was observed that the morphological structure and the distribution of Pt-NPs on the surfaces of the films changed with changing the precursor concentration. The size of the Pt-NPs increased by increasing the concentration of the H_2PtCl_6 as shown in the Figures. The average particle size of Pt thin film was carried out using Image J software. The measured particle size of sample Pt15 is around 20 nm.

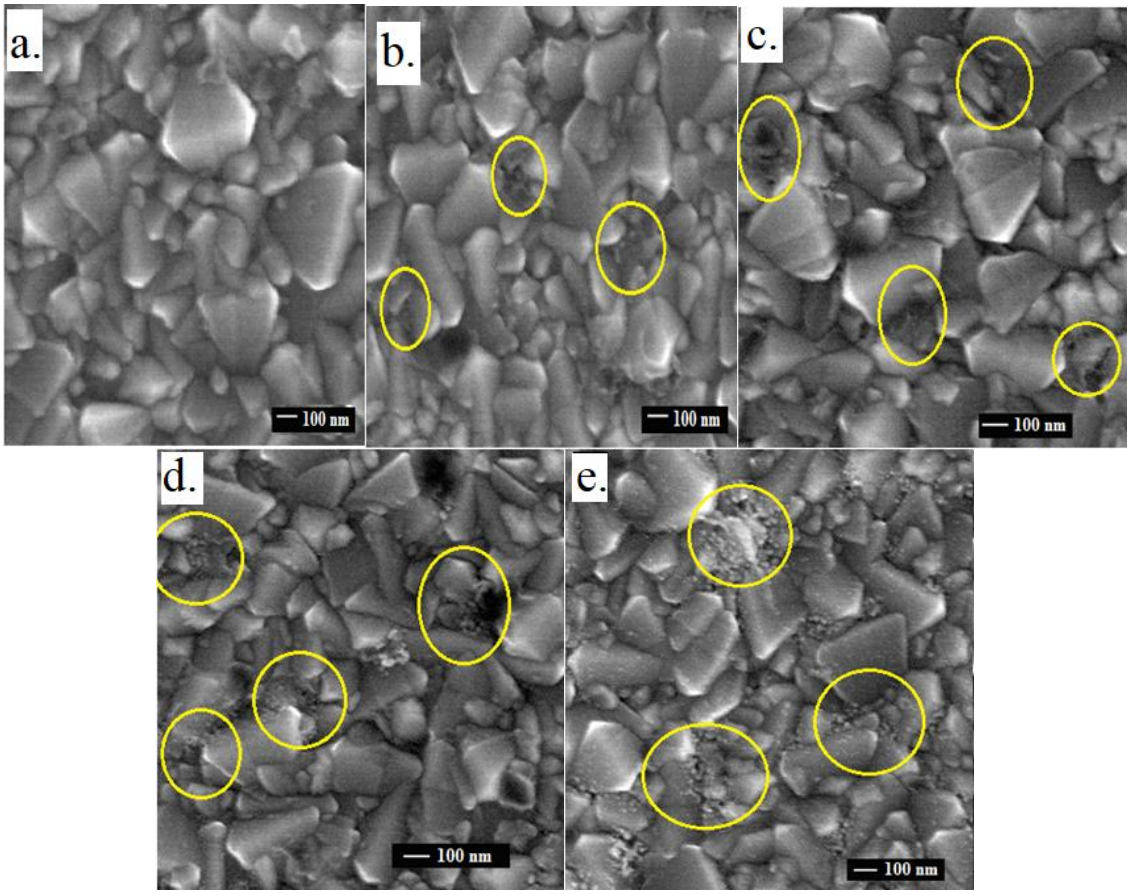

Figure 4.4. FESEM photographs of Pt/ FTO thin films: a. bare FTO, b. Pt2.5, c. Pt5, d. Pt10 and e. Pt15.

B- Two layers of Pt film

Figure 4.5) shows the FESEM images of Pt NPs prepared using the spin coating machine with four concentrations of Pt precursor solution which are 2.5, 5, 10 and 15 mM. The preparation process has been repeated twice to obtain two layers of Pt films on the FTO substrate. The sample DPt2.5 with concentration of 2.5 mM consists of uniform morphology with low agglomeration and very uniform thin layer of Pt. The grains are homogeneously distributed with the similar sizes on the surface. Furthermore, the average diameter of Pt-NPs increased with increasing of H_2PtCl_6 precursor concentration. The formation of larger particles at higher H_2PtCl_6 concentration could be explained by the fact that many more Pt atoms were formed in the aqueous phase and the

effective collision number was raised [162]. The histogram of diameter distribution of Pt-NPs is shown in Figure 4.6. It is clearly observed that the morphology of Pt films markedly depends on the precursor solution concentration [163–165].

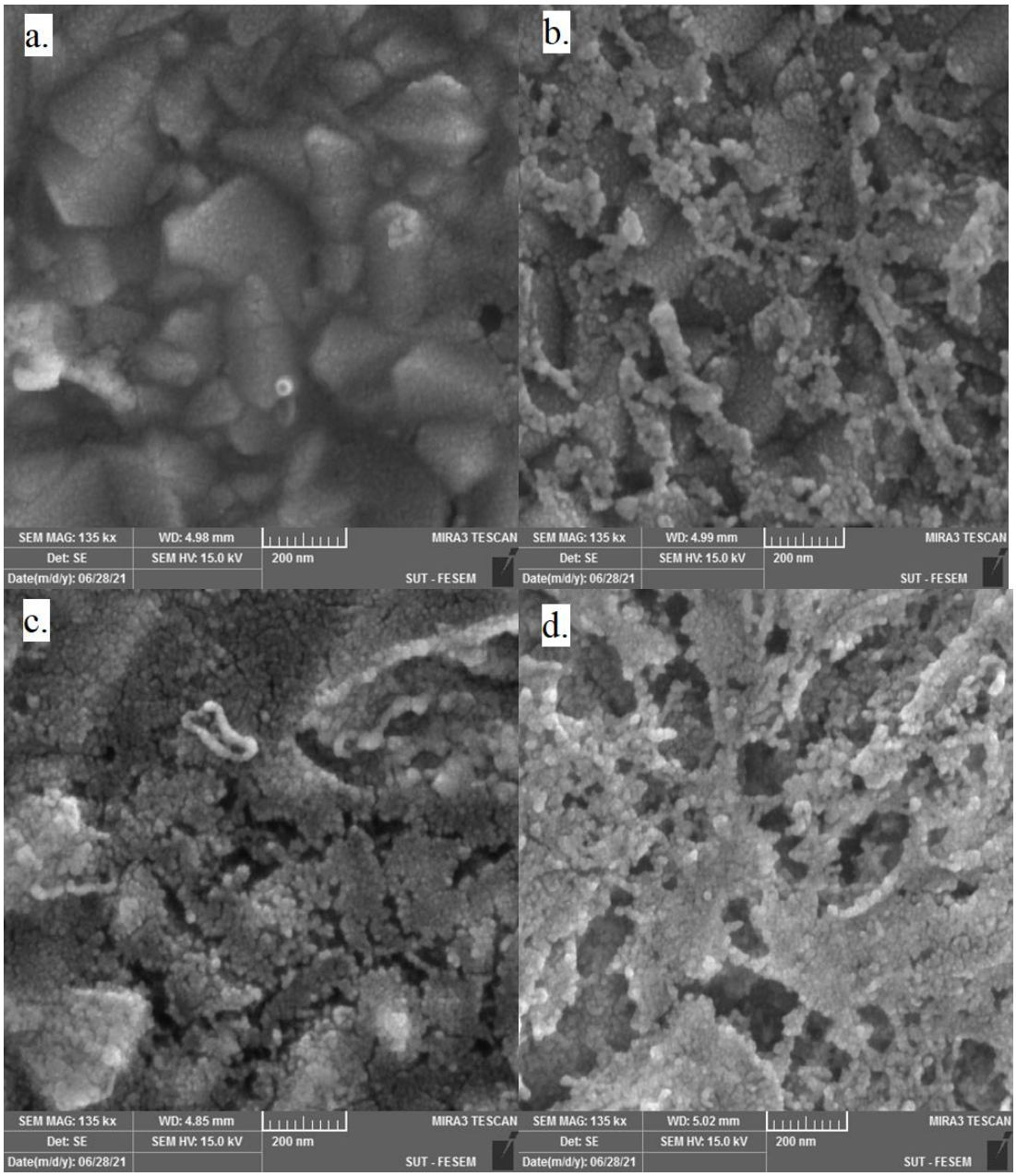

Figure 4.5. FESEM photographs of double layer Pt/ FTO thin films a. DPt2.5, b. DPt5, c. DPt10 and d. DPt15.

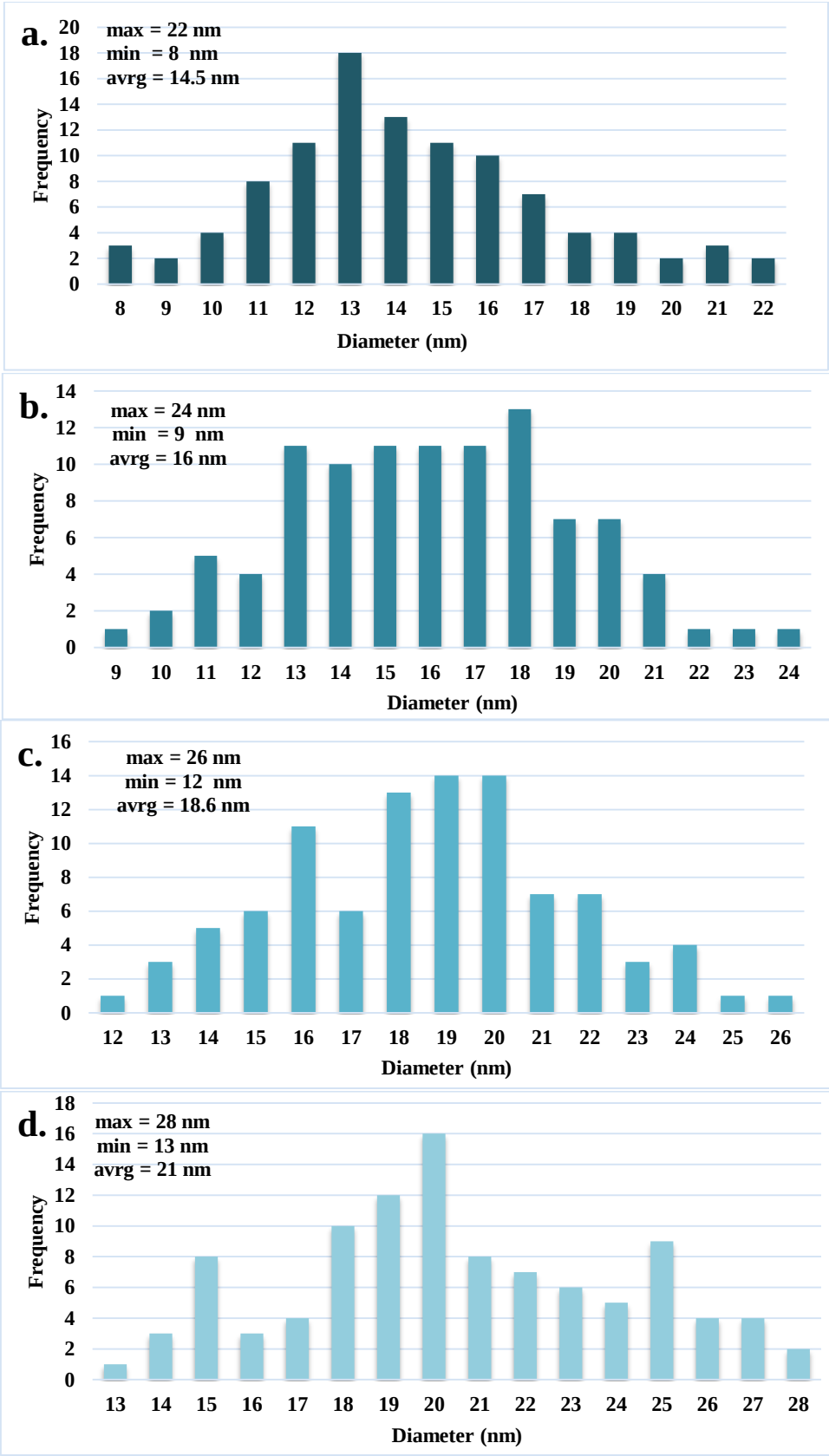

Figure 4.6. The histogram diameter distribution of double layer Pt/ FTO thin films A. DPt2.5, B. DPt5, C. DPt10 and D. DPt15.

4.2.3. Optical Properties

As it was observed from Figure 4.3, with increasing H_2PtCl_6 concentration, the produced films were not totally transparent so it is necessary to measure the light transmittance to determine their optical properties. Figure 4.7 shows the transmittance of Pt/FTO by EMC-LAB VIS-1100 spectrophotometer using the FTO as a reference.

The transparency of platinum thin films has been decreased with increasing of the precursor concentrations. These results are supported by FESEM characterization. In addition, it can be observed that platinum thin film has a highly transparency of about 98% a.u. at single layer of the lowest H_2PtCl_6 concentrations of 2.5 mM sample Pt2.5. It was reported previously that in DSSCs, the better the CE the highest the optical transparency at wavelength = 550 nm [166].

The transparency of single layer gradually increased from 90, 93, 96.1 to the highest percentage 98 a.u. and the double layers increased from 60, 68, 73.1 to the highest percentage 77 a.u.by decreasing the concentrations as 15 mM, 10 mM 5 mM, and 2.5 mM, respectively. The previous results are shown the validity of the Beer-Lambert law [167,168]. The increment of transparency leads to improve the efficiency. This is due to its low cost and the undesired reflection losses. Moreover, the DSSC can absorb light from the front and back [66].

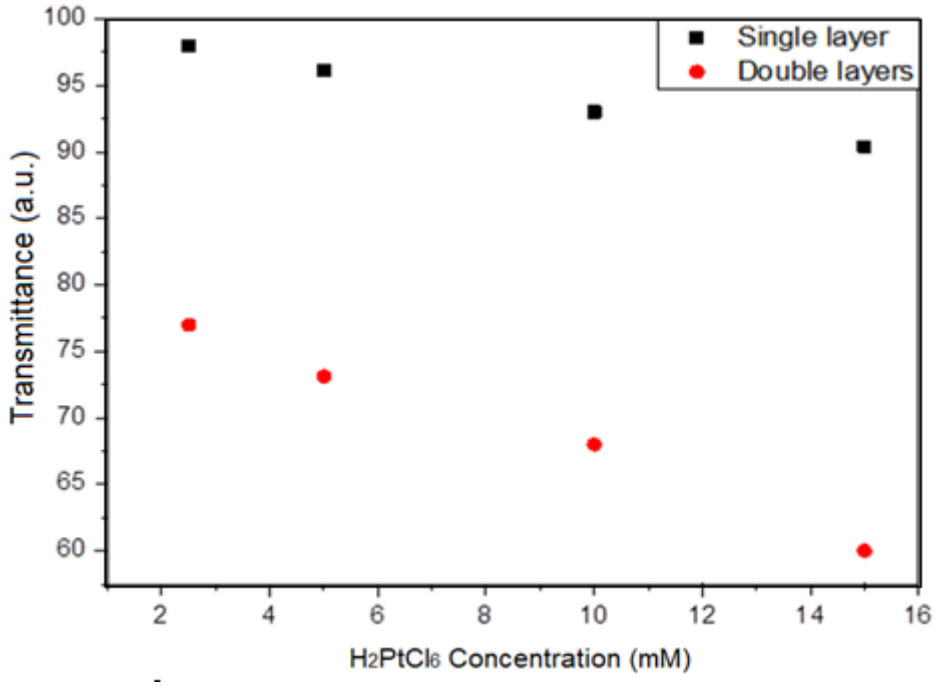

Figure 4.7. Transparence properties of Pt/ FTO thin Films.

4.2.4. The sheet resistance

I-V measurements of the collinear four-point probe are shown in Figure 4.8. From this Figure, it can be concluded that all the prepared samples have ohmic contact with the four-point probe. For single layer the lines of current-voltage curve are overlapped because of the similar values of surface resistance of the samples.

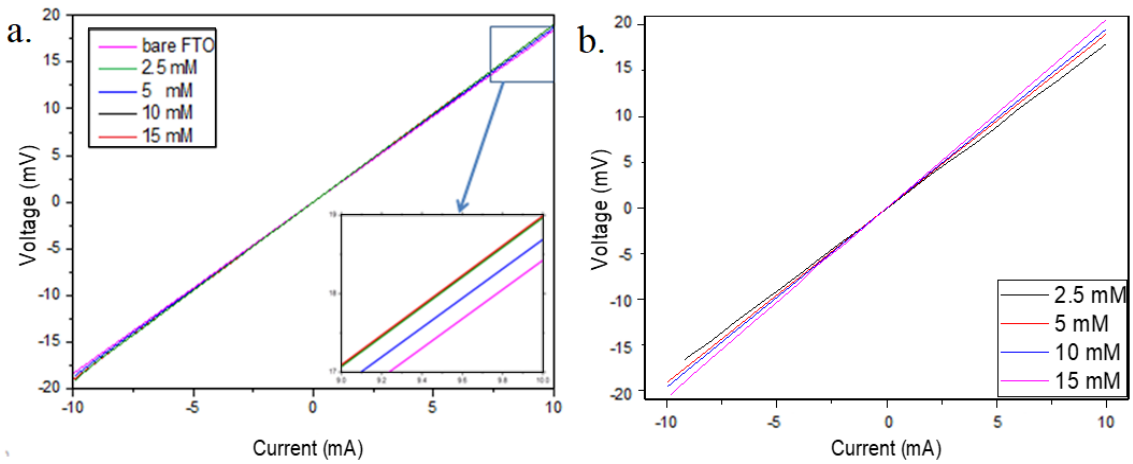

Figure 4.8. I-V Characterizations of: a. single layer, and b. double layer of Pt/FTO thin films measured by the four-point probe device.

The measured resistance, sample dimensions, correction factor, and surface resistance of the bare FTO and Pt/FTO thin films are listed in Table 4.1 and plotted in Figure 4.9. It is clearly observed that the sheet resistance of the bare FTO closes to the value of Sigma Aldrich (~7 Ω/sq). The single layer the Pt/FTO has a slight change in the surface resistance also closes to the value of Sigma Aldrich. The slight change was due to the fact that the Pt films with the lowest thickness are more suitable for discontinuity through the surface. The sheet resistance measurements were greatly effects when the conditions of simple connected area of the van der Pauw theorem are violated [169]. While the sheet resistance increases with an increase in the H_2PtCl_6 concentrations for double layers. The fact of increasing the sheet resistance may be due to an increase in the film thickness and vacancy between the Pt NPs. The vacancies play a role as ohmic resistance between the FTO and the probe where it obstructs the flow of the current. These results can support the results that obtained from FESEM image.

Table 4.1. Four-point probe method sheet resistance results.

Sample	**R (Ω)**	**D (mm)**	**D/S**	K_s [170]	R_s **(Ω/sq)**
bare FTO	1.79	19	10.56	4.22	7.55
DPt2.5	1.80	20	10.8	4.22	7.6
DPt5	1.90	20	10.8	4.22	8.03
DPt10	1.95	20	10.8	4.22	8.25
DPt15	2.06	20	10.8	4.22	8.69

❖ **Where S is the space between to probes = 1.8mm**

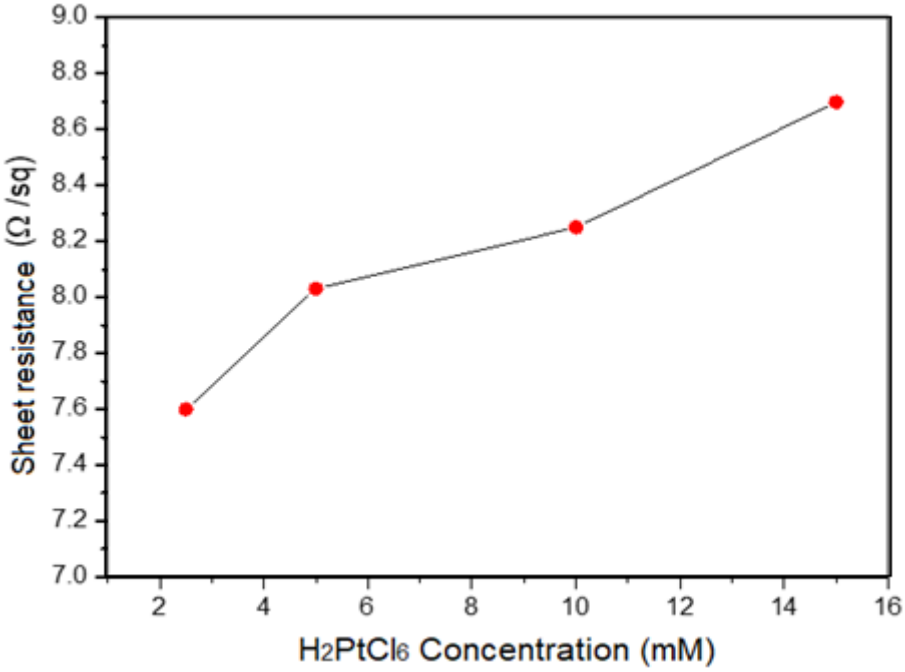

Figure 4.9. The sheet resistance of double-layers Pt/FTO thin films.

4.3 Characterization of MWCNT-ZnO/TiO_2/FTO PEs

TiO_2 NRs are fabricated on fluorine doped tin oxide (FTO) by hydrothermal technical at 433K for 5 h. The structural, morphological and optical properties have been studied with various factors. These factors are listed in Table 3.3. The next process is the synthesized of MWCNT and ZnO NRs on the sample ET of TiO_2 NR layer. At first the TiO_2 NR are coated by ZnO seed layer. MWCNT are insetted into ZnO seed layer with different concentration. ZnO seed layer was deposited using spin coater device. Hydrothermal are used to prepare ZnO NRs at 363K for 2 h. ZnO/TiO_2 with different MWCNT weighting percentage are listed in Table 3.4. After synthesis of the semiconductor, the next step is to characterize the properties. These functional properties and characterization methods include crystallographic and phase analysis by film XRD, morphology studies by FESEM and Eg determination by UV-Vis Spectroscopy.

4.3.1 Structural properties TiO_2

The XRD analysis of the prepared samples was done using X-Ray Diffractometer (Philips PW 1730), Cu-Kα X-rays of wavelength (λ)=1.54187 Å and data was taken for the 2θ range of 9.7° to 79.9° with a step of 0.05°. Crystallographic and phase analysis of photoanodes were done by X'Pert HighScore Plus and drawn it using Origin software. The x-ray diffraction investigation has been carried out for the prepared thin films by the hydrothermal method that is deposited on FTO conductive glass slides. X'Pert HighScore Plus software was used to match the peaks of synthesized TiO_2/FTO with the stander values JCPDS card. For example, Figure 4.10 shows the matching of sample BT.

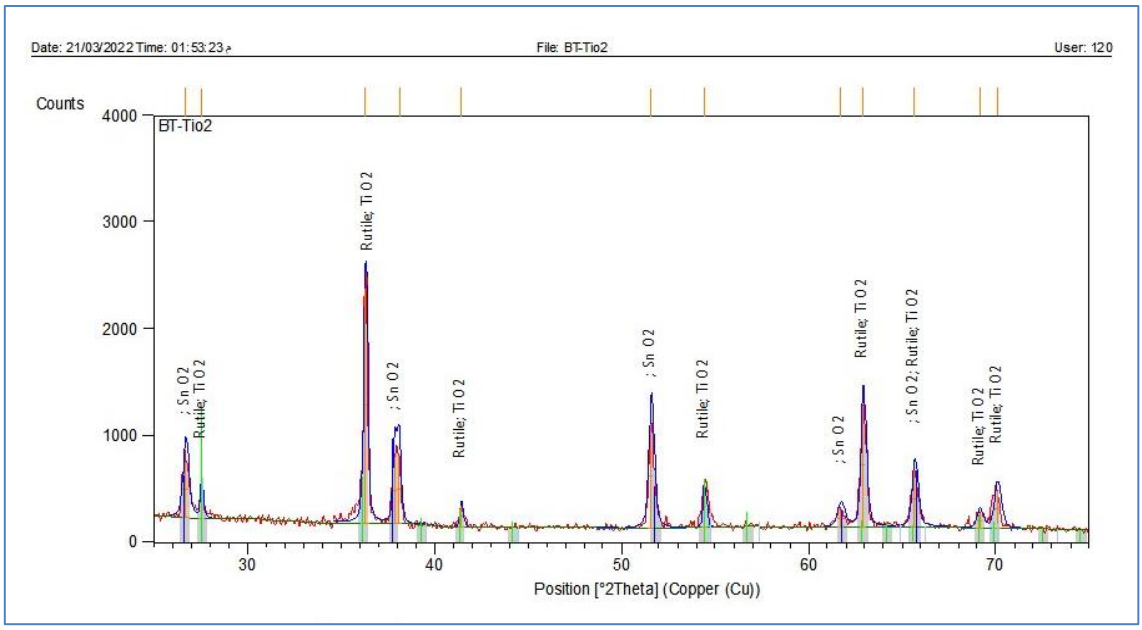

Figure 4.10. The matched result of XRD pattern of sample BT using X'Pert HighScore Plus software.

The main peaks of the glass slides FTO that attributed to SnO_2 (JCPDS card number 46-1088) are (110), (101), (200), (211), (310) and (301) at 2θ = 26.65°, 33.7°, 38°, 51.65°, 61.6° and 65.7° which corresponds to [38]. Sample (AT) shows a white film was formed on the FTO substrate at a high HCl concentration. This white film is fragile, non-adhesive and can be simply

erased. For this reason, sample (AT) cannot be used for the DSSC application so it was excluded. Figure 4.11 shows the crystalline phases of synthesized TiO_2 on FTO substrate with different HCl concentration and etching time. From this Figure it was observed that all TiO_2 samples appear in the rutile phase where the rutile phase is grown in an acidic solvent [58]. The peaks of TiO_2 NRs are attributed to JCPDS card number 01-076-0649. The rutile phase of TiO_2 was a tetragonal crystalline system with a,b = 4.593 and c= 2.959 and $\alpha,\beta,\gamma = 90°$.

The peaks of sample BT are (110), (101), (111), (211), (002) and (112) located at 2θ = 27.55°, 36.29°, 41.46°, 54. 47°, 62.95° and 70.08^o which corresponds to [172]. Sample DT has same peaks of sample BT except the two peaks (110) and (111) which were absent while the peak (210) has been appeared at 2θ = 44.05° when decrease the acid concentration. At a low acid concentration, the peak (112) of sample CT vanishes. TiO_2 nanostructure was grown in the same direction as FTO film, which means the FTO film plays an important role as a seed layer to grow TiO_2. The result can be confirmed because at the synthesis procedure the TiO_2 NRs just adhere on the FTO surface while no film is formed on the other side of the substrate bare glass. At next the etching time will not change the structure properties [176].

The following peaks intensity (101) and (002) decrease with increased of etching time. These peaks may determine the length of TiO_2 NRs because the height of TiO_2 NRs is directly proportional to the intensity of the previous peaks. This suggests that TiO_2 NRs grow in the [101] and [001] direction with the growth axis vertical to the FTO substrate [175] . This result can be confirmed by FESEM images. The grain size of TiO_2 nanostructures is listed in Table 4.2. The grain size of main peaks (101) and (003) of TiO_2 nanostructures are reduced with decrees the HCl concentration whereas has same behavior

with increasing the etching time. These behaviors will be explained in FESEM section.

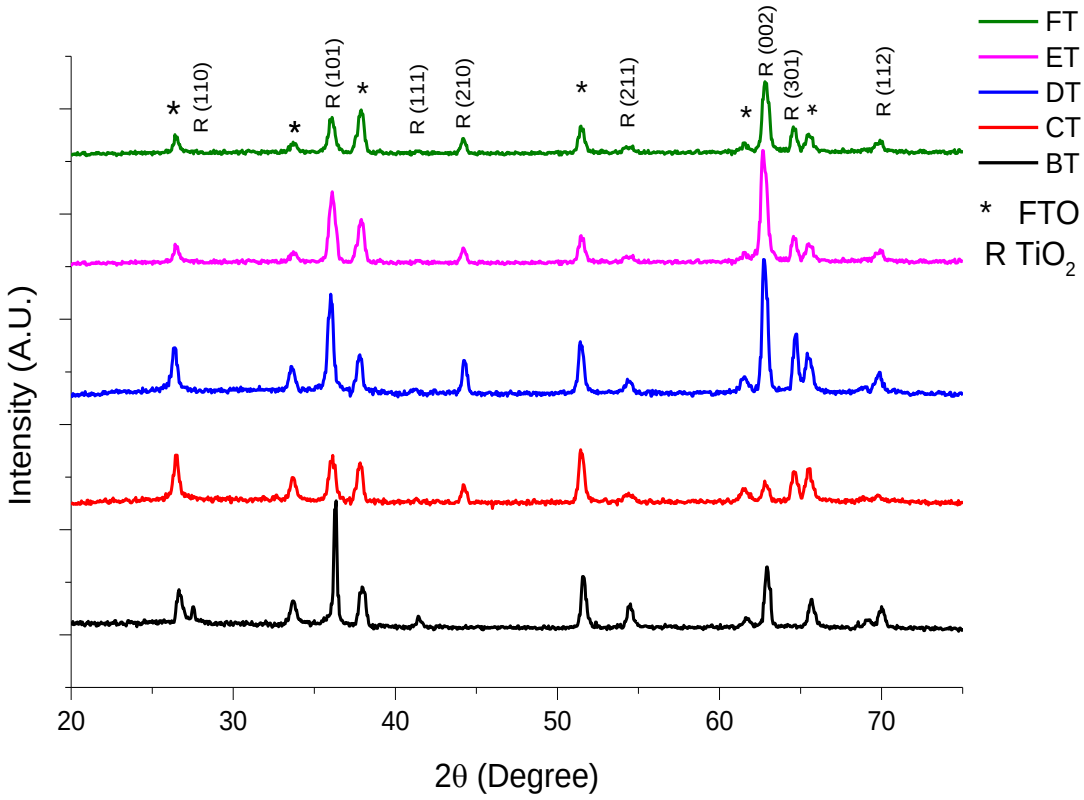

Figure 4.11. XRD pattern of all synthesized sample of TiO_2 NRs.

Table 4.2. The structural analysis of TiO_2 NRs.

Sample	2θ° Degree	d-spacing (nm)	FWHM (rad)	hkl	Particle size nm
BT	27.540	3.415	0.295	110	27.708
	36.298	2.608	0.197	101	42.481
	41.470	2.293	0.590	111	14.388
	54.469	1.771	0.394	211	22.700
	62.910	1.551	0.246	002	37.857

	70.082	1.408	0.344	112	28.174
CT	36.097	2.622	0.316	101	26.441
	44.199	2.157	0.256	210	33.493
	54.483	1.771	0.600	211	14.882
	62.795	1.554	0.336	002	27.700
	64.613	0.295	0.543	301	17.310
DT	36.073	2.624	0.226	101	36.919
	44.199	2.157	0.232	210	36.958
	54.429	1.772	0.600	211	14.879
	62.839	1.553	0.274	002	34.025
	64.462	1.517	0.492	301	19.077
	69.823	1.413	0.447	112	21.653
ET	36.103	2.622	0.296	101	28.228
	44.199	2.157	0.239	210	35.875
	62.811	1.554	0.279	002	33.326
	64.096	1.525	0.504	301	18.585
	69.875	1.412	0.477	112	20.299
FT	36.101	2.622	0.256	101	32.639
	44.199	2.157	0.250	210	34.283
	62.747	1.555	0.327	002	28.420
	64.156	1.524	0.551	301	17.007
	69.913	1.411	0.509	112	19.036

4.3.2 Structural properties MWCNT-ZnO/TiO_2

The X-ray diffraction investigation has been carried out for the synthesized ZnO via hydrothermal method deposited on TiO_2 NR with different MWCNT concentrations. The MWCNT was added to the ZnO seed layers. The structure properties of MWCNT-ZnO/TiO_2 are shown on Figure 4.12. The XRD spectra of the MWCNT-ZnO/TiO_2 NRs indicate that structure of TiO_2 NRs unchanged because the ZnO was grown on the surface of the TiO_2 NRs. The ZnO seed layer was grown in TiO_2 (002) direction which led to taking ZnO same direction.

Therefore, ZnO NRs were grown in the (002) plane. Furthermore, there is no distinct MWCNT peak, indicating no phase separation. Perhaps that the MWCNT is well integrated into the ZnO seed layer and the crystal structure for all investigated compositions. Another reason, the small amount of MWCNT perhaps cannot be detected. However, the MWCNT concentration led to shaft the ZnO peak position [103]. This is due to the growth of ZnO nanostructure onto MWCNT. The XRD analysis shows the grain size of ZnO NRs are increased with increasing of the MWCNT concentration.

This is another evidence of the growth of ZnO nanostructure onto MWCNT which leads to an increase in the grain size of ZnO. The grain size of MWCNT-ZnO/TiO_2 nano structures are listed in Table 4.3.

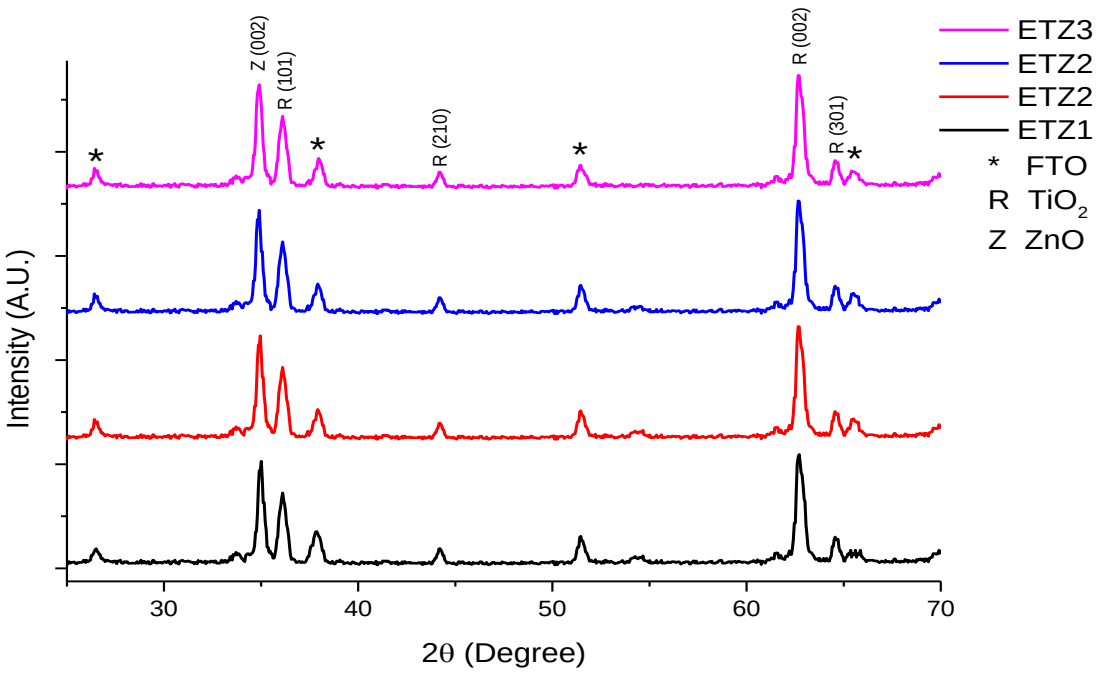

Figure 4.12. XRD pattern of synthesized MWCNT-ZnO/TiO_2.

Table 4.3. The structural analysis of MWCNT- ZnO/TiO_2.

Sample	2θ° Degree	d-spacing (Å)	FWHM (rad)	hkl	Particle size (nm)
ETZ1	34.981	2.5629	0.394	002	21.141
ETZ2	34.959	2.5645	0.386	002	21.577
ETZ3	34.945	2.5655	0.377	002	22.092
ETZ4	34.916	2.5676	0.337	002	24.712

4.3.3 Morphological and composition properties of TiO_2 NRs.

The morphology and particle size distribution of TiO_2 NRs were assessed by SEM analysis technical. Figure 4.13 shows the SEM Images of TiO_2 samples synthesized using hydrothermal methods on FTO substrate with different HCl concentration and etching time. These images show that TiO_2 NRs grown on the FTO surface. TiO_2 NRs were evenly distributed over FTO

substrate. On the other hand, the EDX results shows the contents of the optical electrode of all synthesized samples are clear from the impurities as shown in Figure 4.14.

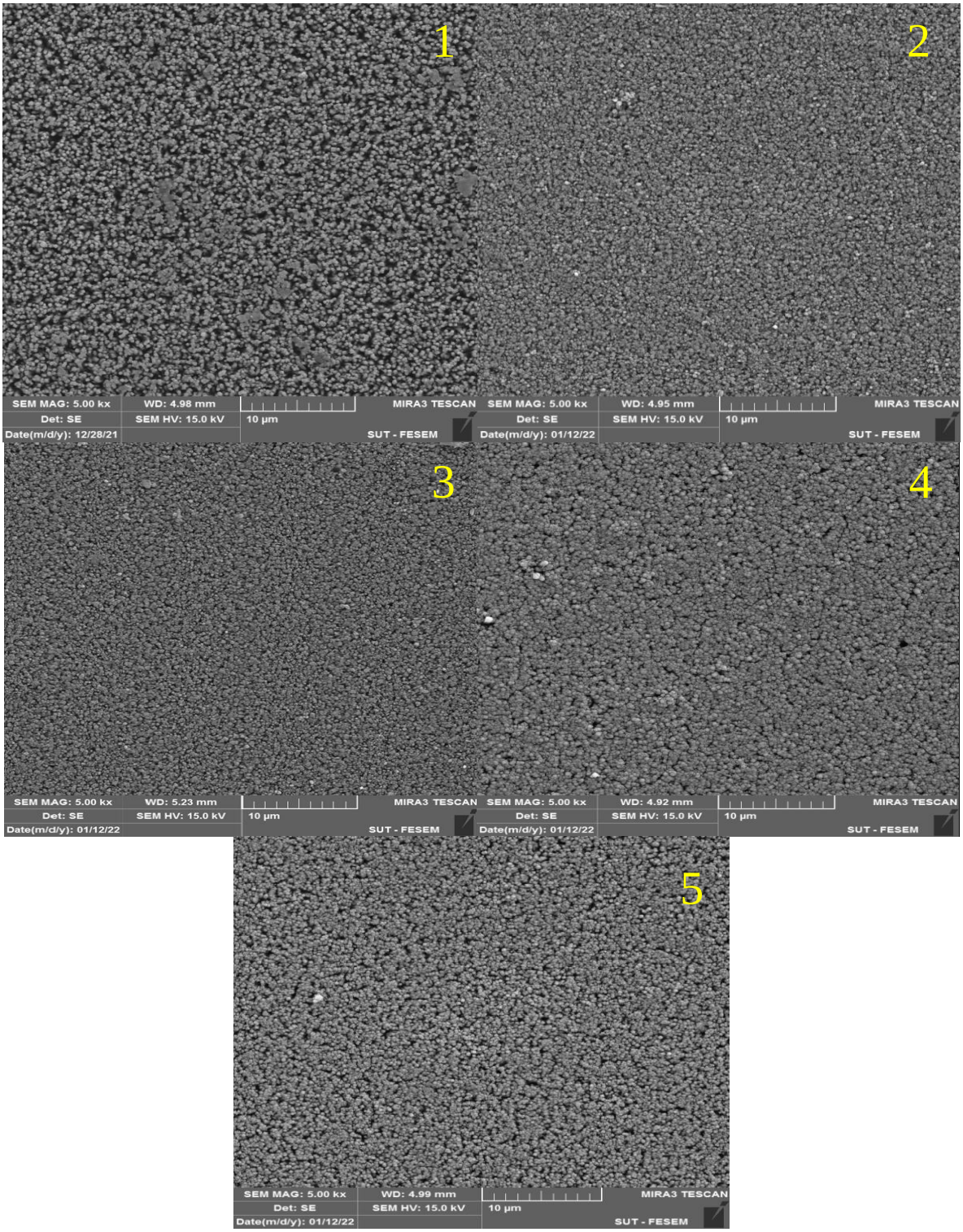

Figure 4.13. The SEM Images of TiO_2 samples with (5Kx) magnification 1. BT, 2. CT, 3. DT, 4. ET and 5. FT.

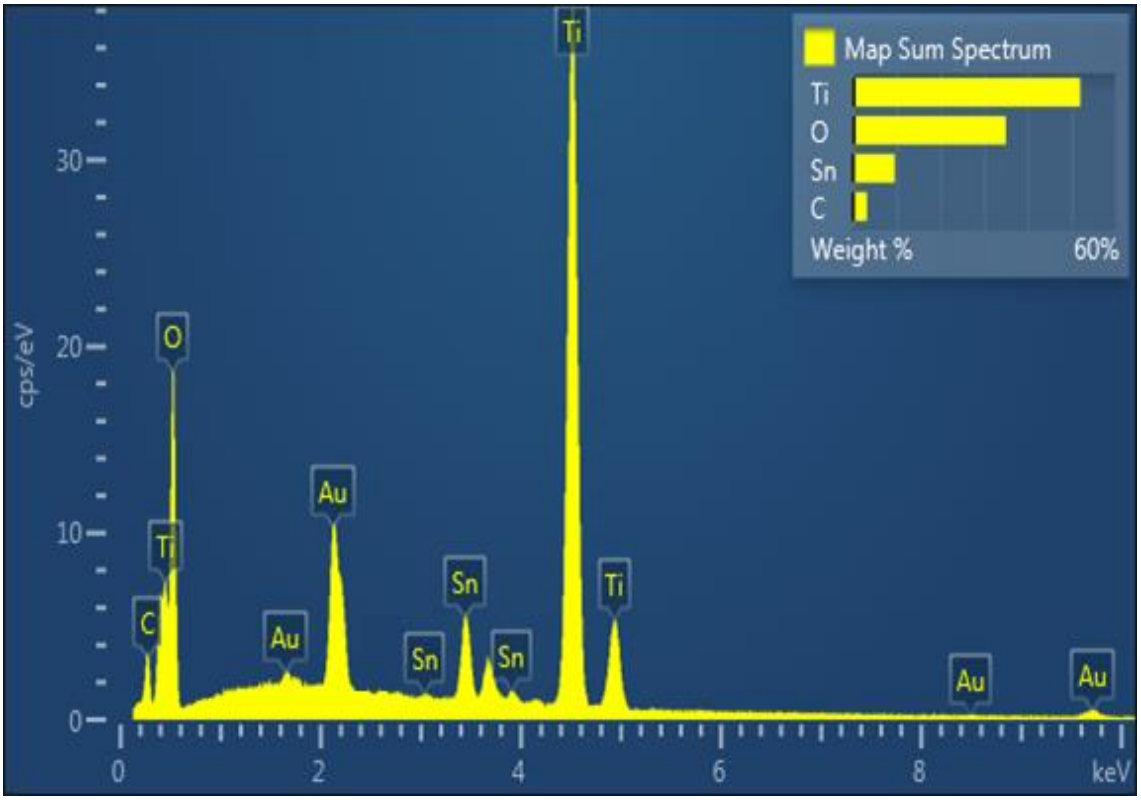

Figure 4.14. EDX results of TiO_2/FTO.

Figure 4.15 shows the cross-section and SEM Images of sample BT. The diameter of TiO_2 is very low and close together. Consequently, large clumps were formed of TiO_2 NRs. The NRs are tetragonal in shape with square top facets, the expected growth habit for the tetragonal crystal structure. The average diameter and length are 170 nm and 4.0 µm, respectively were exhibited in Figure 4.20 and listed in Table 4.4.

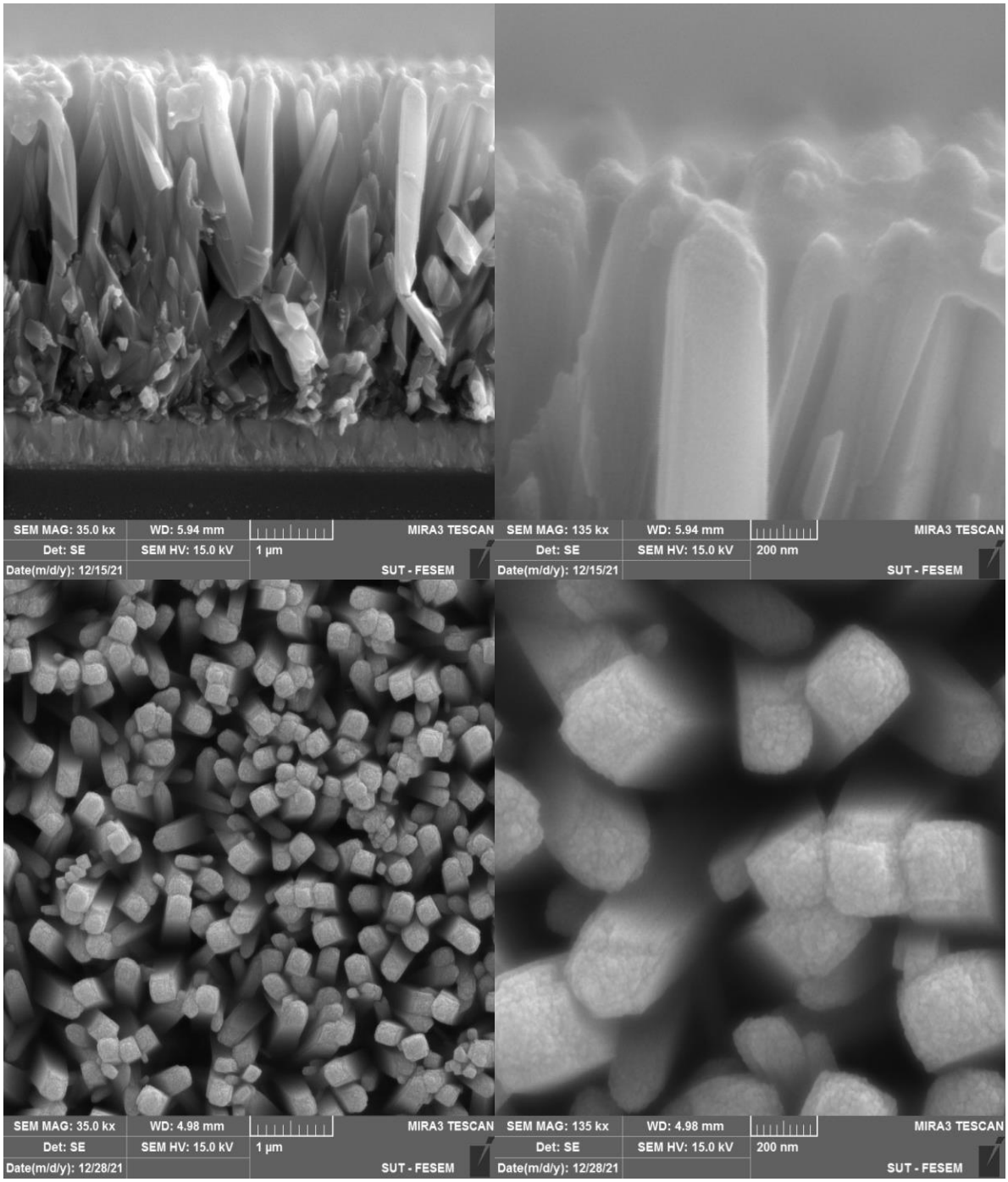

Figure 4.15. The cross-section and FESEM Images of sample BT.

The cross-section and FESEM images of sample CT and DT are shown in Figures 4.16 and 4.17, respectively. From these Figures, it was obtained that the distance between TiO_2 NRs increased with decreased HCl concentration. Furthermore, the lengths of TiO_2 NRs decreased and the average diameter are increased.

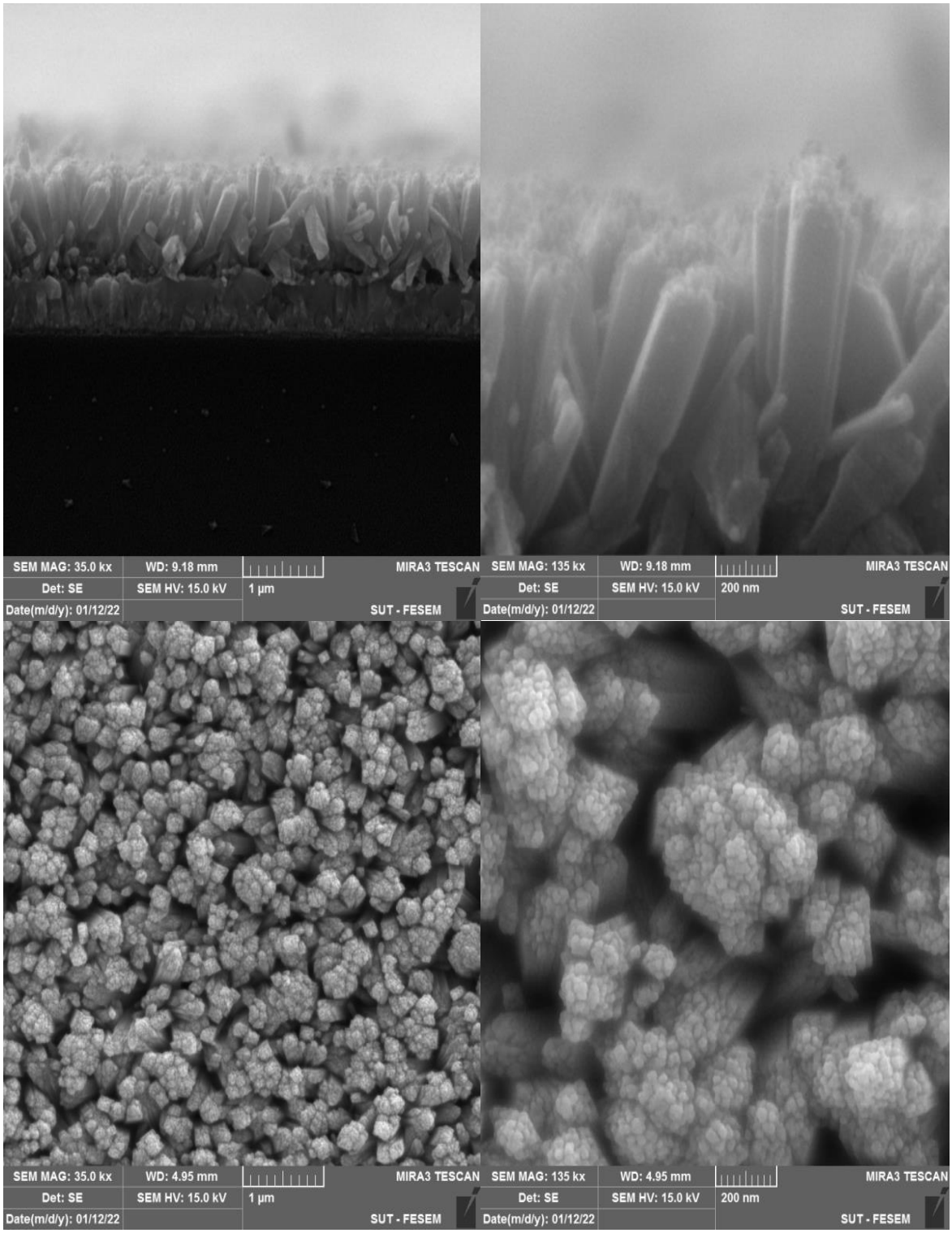

Figure 4.16. The cross-section and FESEM Images of sample CT.

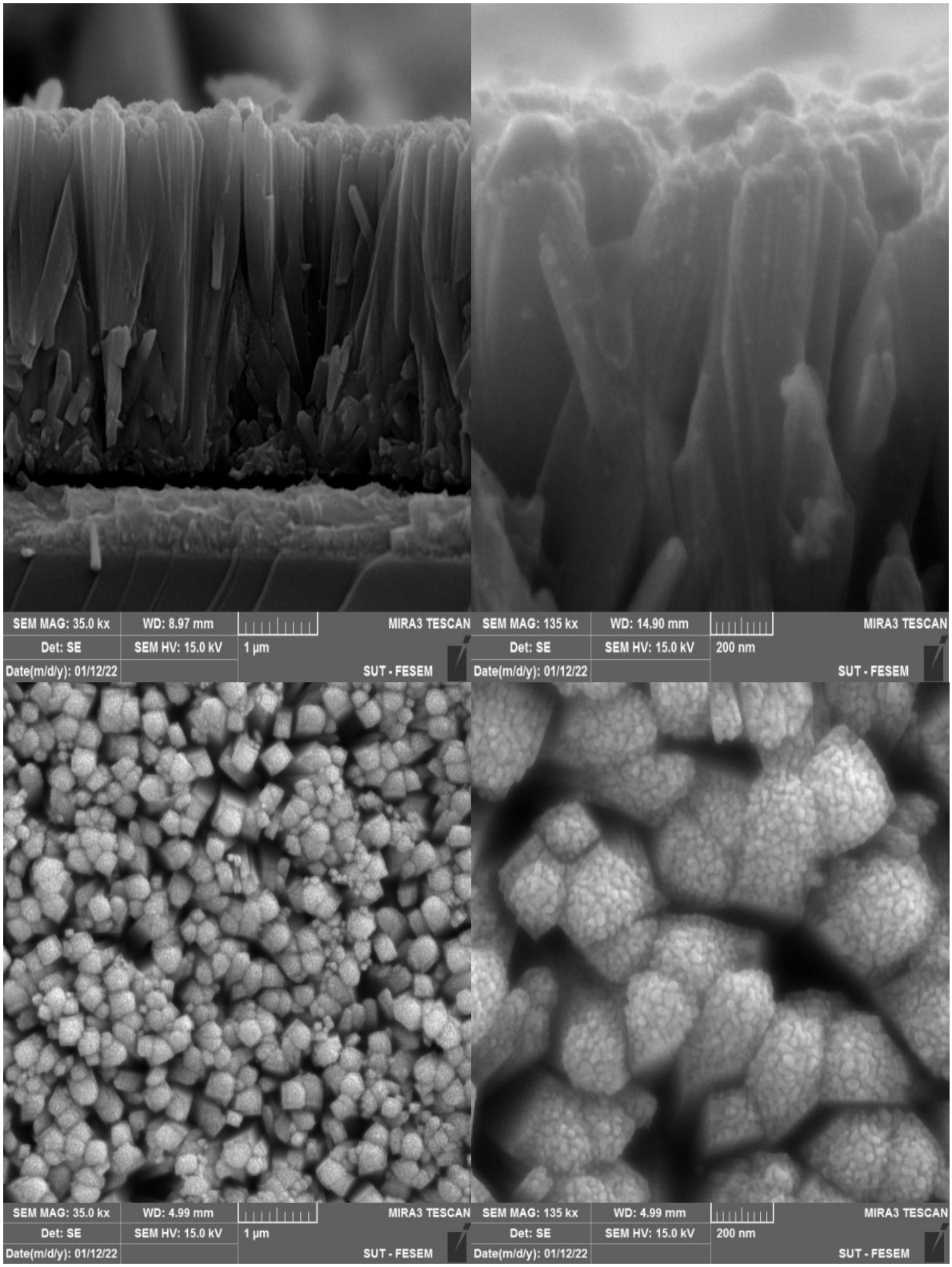

Figure 4.17. The cross-section and FESEM Images of sample DT.

The lengths and the average diameter of TiO_2 NRs are changed with different HCl volume. So, to discuss the effect of HCl concentration on the structure and morphological properties of TiO_2 NRs, it is necessary to study the chemical reaction between HCl, H_2O and Ti(OBu).

The formation of rutile crystal nucleus in $Ti(OCH_2CH_2CH_2CH_3)_4$ strongly acidic precursor solution can be described by the following process:

First, single polymer $[TiO(OH_2)_5]^{2+}$ forms by the hydrolysis of $Ti(OCH_2CH_2CH_2CH_3)_4$.

Then the single polymer $[TiO(OH_2)_5]^{2+}$ combine through dehydrating each other to form straight chain polymer by the edge connection.

Finally, the straight chain polymers connect through points to form rutile crystal nucleus.

On the other hand, titanium (IV) butoxide react with water as a fallowing [177]:

$$C_{16}H_{36}O_4Ti + 2H_2O \rightarrow TiO_2 + 4\,(C_4H_{10}O) \quad \ldots\ldots\ldots\ldots (4.1)$$

Where $C_4H_{10}O$ is (2-Butanol)

Basing on the heterogeneous nucleation of crystalline phase in solution, TiO_2 NRs nanocrystal particles coated onto FTO followed by heat treatment can be served as the seeds of heterogeneous nucleation. The NRs can be formed via the deposition and reorganization of TiO_2 seeds during the dynamic chemical dissolution and deposition processes. In addition, a strong hydrochloric acid plays a significant role when TiO_2 growth units deposit on TiO_2 crystal seeds, and it can promote TiO_2 crystal to grow into rods instead of particles [175]. It can be concluded that the high HCl concentration, water content is not enough to produce TiO_2 to produce seed layer coated on FTO.

Therefore, the non-adhesion of TiO_2 NRs on FTO in sample (AT) was caused by the missing of the seed layers. In contrast, when HCl decrease and the H_2O volume is increased therefore TiO_2 seed layers are formed onto the FTO substrate. This leads to grow of TiO_2 NRs onto the FTO surface as in sample (BT). Finally, when the water concentration increase, it may lead to increase the seed layer diameter. This fact may explain the inverse proportion between HCl concentration and TiO_2 NRs diameter [178].

Although good TiO_2 NRs were obtained, But the FESEM images show the presence of lumps and agglomerate between TiO_2 NRs. These conglomerates may lead to reduce the surface area of the photo-electrode. Therefore, the etching strategies are expected to improve the photo-electrode performance [179]. Figures 4.18 and 4.19 present TiO_2 NRs after etching time (48 and 72) h at room temperature. The etching time leads to a decrease in the TiO_2 diameter and length. The etching process removes the agglomerated particles on the top of the sample (DT). Where the top of the etched sample (ET) appeared as a brush compared with the untreated surface sample (DT).

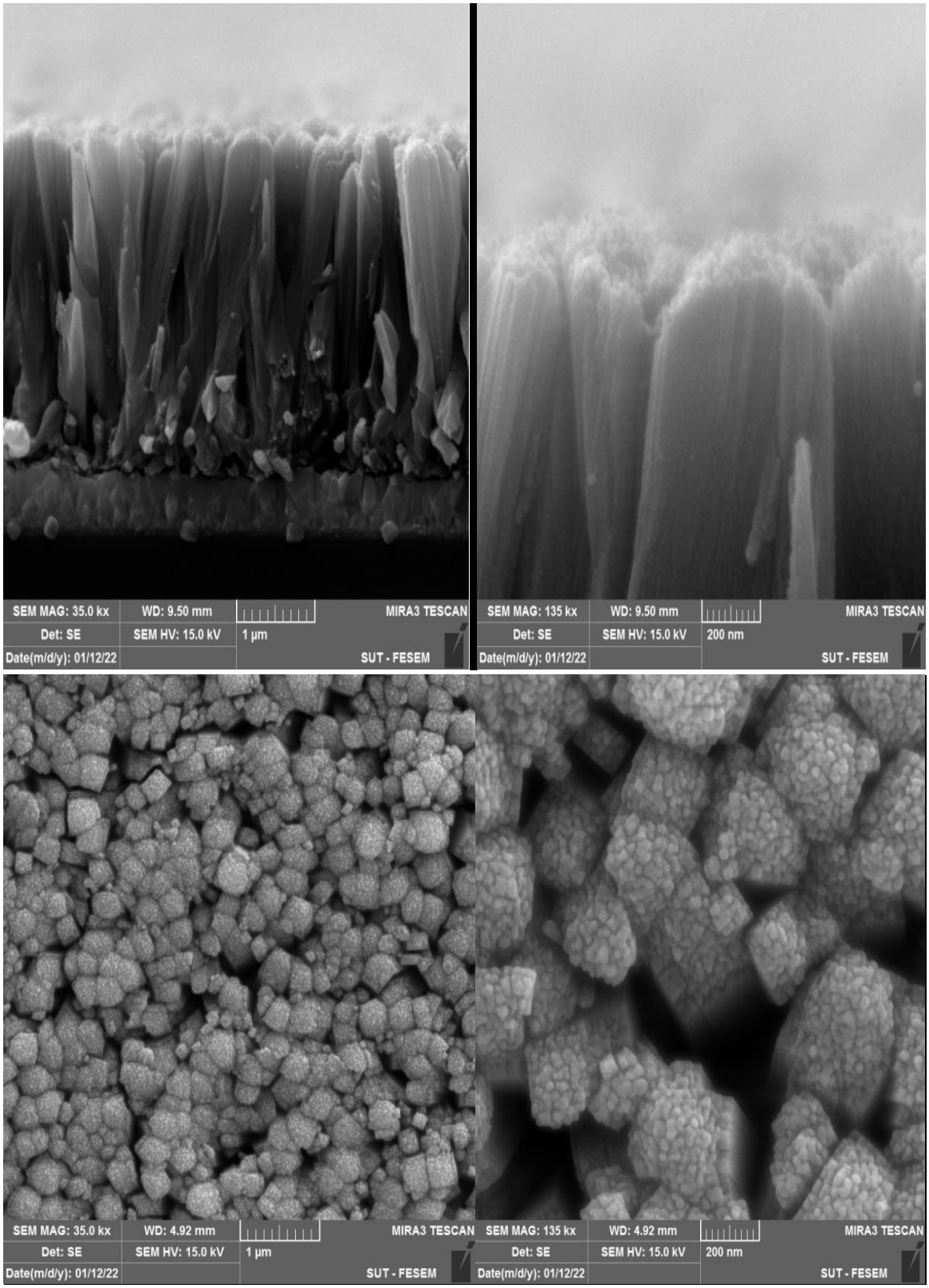

Figure 4.18. The cross-section and FESEM Images of sample ET.

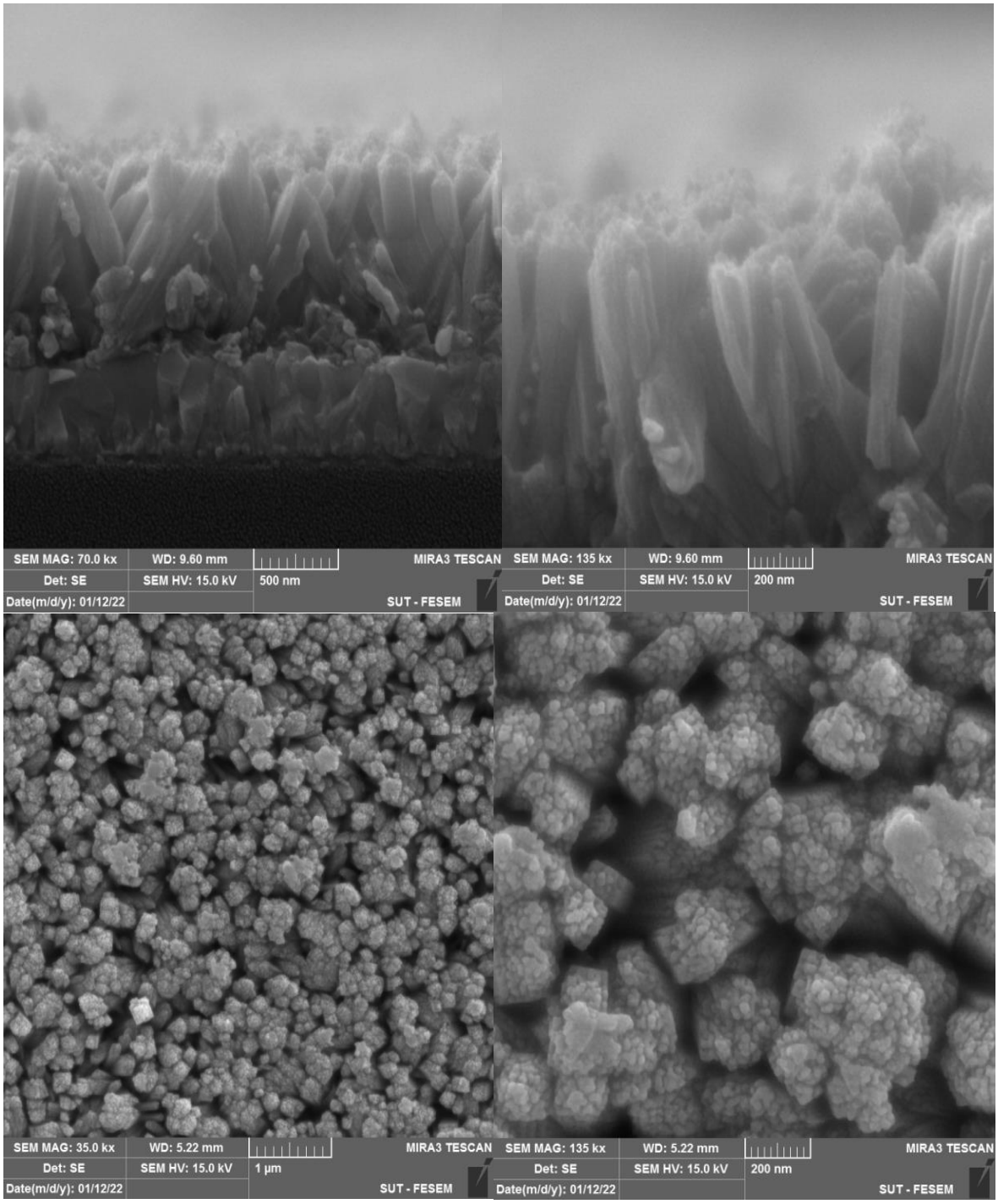

Figure 4.19. The cross-section and FESEM Images of sample FT.

Figure 4.20 display the histogram chart of the diameter distribution of the TiO_2 NRs. The diameter distribution of TiO_2 NRs is obtained from the FESEM result using ImagJ software. The diameter distribution of TiO_2 NRs is strongly affected by HCl concentration. Diameter distribution of TiO_2 NRs was discussed in previous.

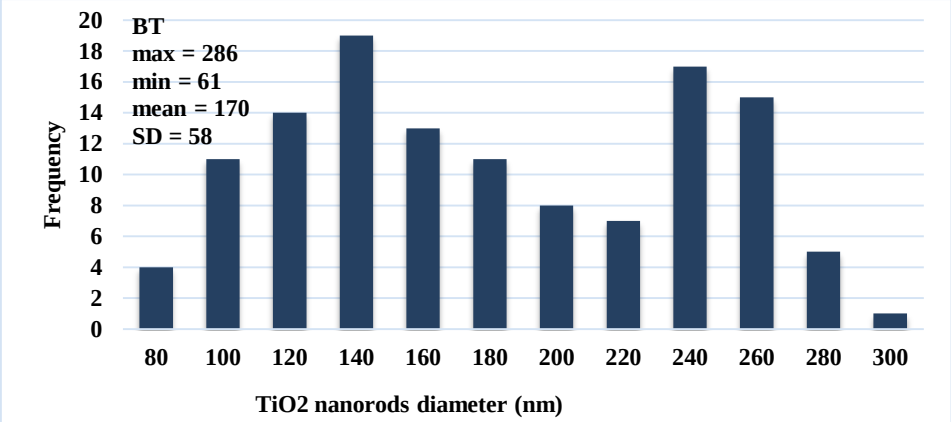
BT
max = 286
min = 61
mean = 170
SD = 58
Frequency
0
2
4
6
8
10
12
14
16
18
20
80
100
120
140
160
180
200
220
240
260
280
300
TiO2 nanorods diameter (nm)

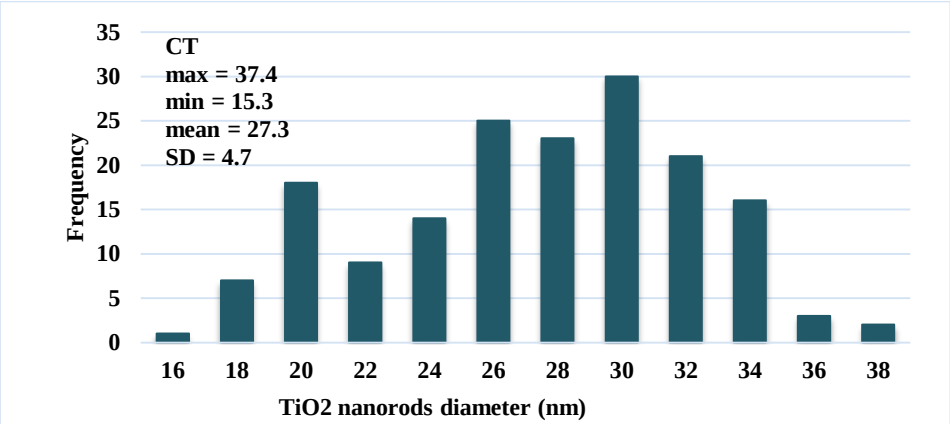
CT
max = 37.4
min = 15.3
mean = 27.3
SD = 4.7
Frequency
0
5
10
15
20
25
30
35
16
18
20
22
24
26
28
30
32
34
36
38
TiO2 nanorods diameter (nm)

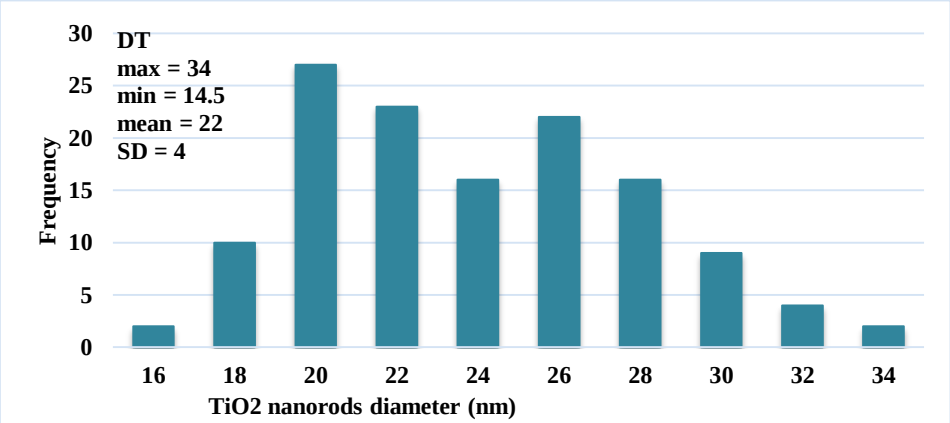
DT
max = 34
min = 14.5
mean = 22
SD = 4
Frequency
0
5
10
15
20
25
30
16
18
20
22
24
26
28
30
32
34
TiO2 nanorods diameter (nm)

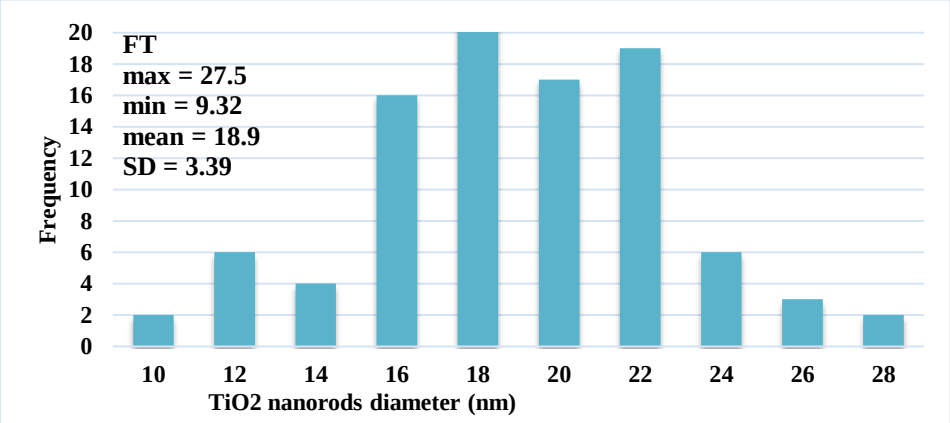
FT
max = 27.5
min = 9.32
mean = 18.9
SD = 3.39
Frequency
0
2
4
6
8
10
12
14
16
18
20
10
12
14
16
18
20
22
24
26
28
TiO2 nanorods diameter (nm)

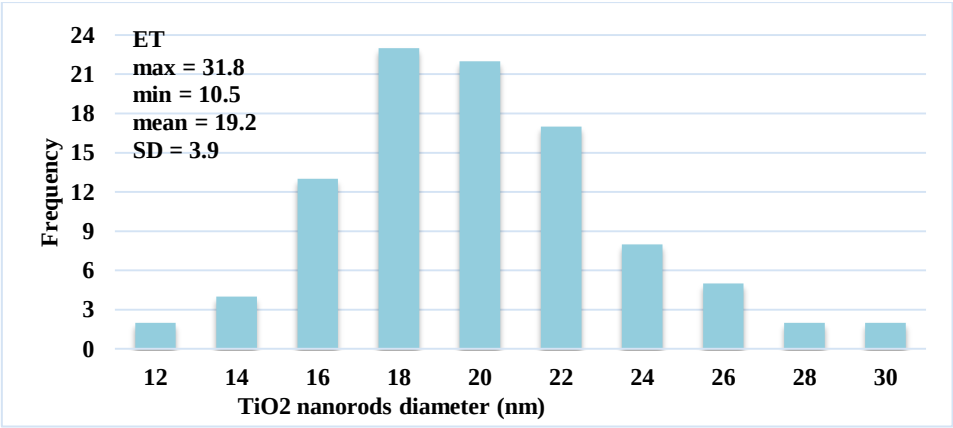

Figure 4.20. The histogram chart of the diameter distribution of TiO_2 NRs.

Table 4.4. Lengths of TiO_2 NRs and the average diameter.

Sample	high (µm)	Average diameter (nm)
BT	4	170
CT	1.68	27.3
DT	3.85	22
ET	3.8	19.2
FT	1.43	18.9

4.3.4 Morphological and composition properties MWCNT-ZnO/TiO_2

Sample ET of TiO_2 NRs was selected to the next stage duo to the exhibited unique properties. Sample ET was Distinguished from the other sample because it has a perfect length and diameter. So sample ET was nominated to obtain high efficiency of DSSC. ZnO seed layer was prepared on sample ET of TiO_2 NRs using spin-coater device. MWCNT are incorporated into ZnO seed layer with difference concentration.

Figure 4.21 shows the ZnO seed layer was agglutinated on TiO_2 NRs surface. MWCNT wires cannot be displayed in Figure 4.21, due to a lower content of carbon nanotubes in zinc acetate-MWCNT precursor solution (0.5%, 1% and 1.5%, respectively) [180]. Furthermore, the MWCNTs dropped into the interspaces between TiO_2 NRs.

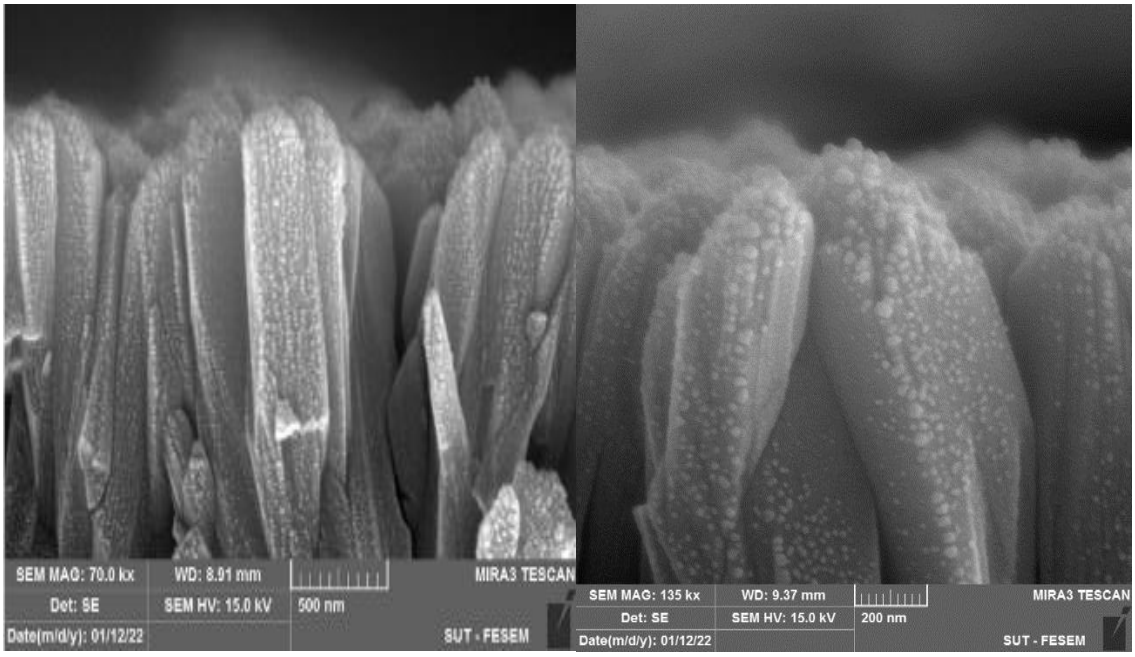

Figure 4.21. FESEM image of ZnO seed layer on TiO_2 NRs.

Figure 4.22 carried out the EDX analysis to identify the elemental composition of the prepared optical electrode (MWCNT-ZnO/TiO_2). EDX results shows the contents of the optical electrode of after prepared the ZnO seed layer are clear from the impurities. EDX results appear a small amount of the ZnO compared with other contents because the ZnO seed layer is a thin layer on the TiO_2 NRs. Moreover, MWCNT cannot be indicated by EDX due to the small amount where maximum concentration of the MWCNT 1.5 % of zinc-acetate concentration. In addition, carbon is present in the substrate structure.

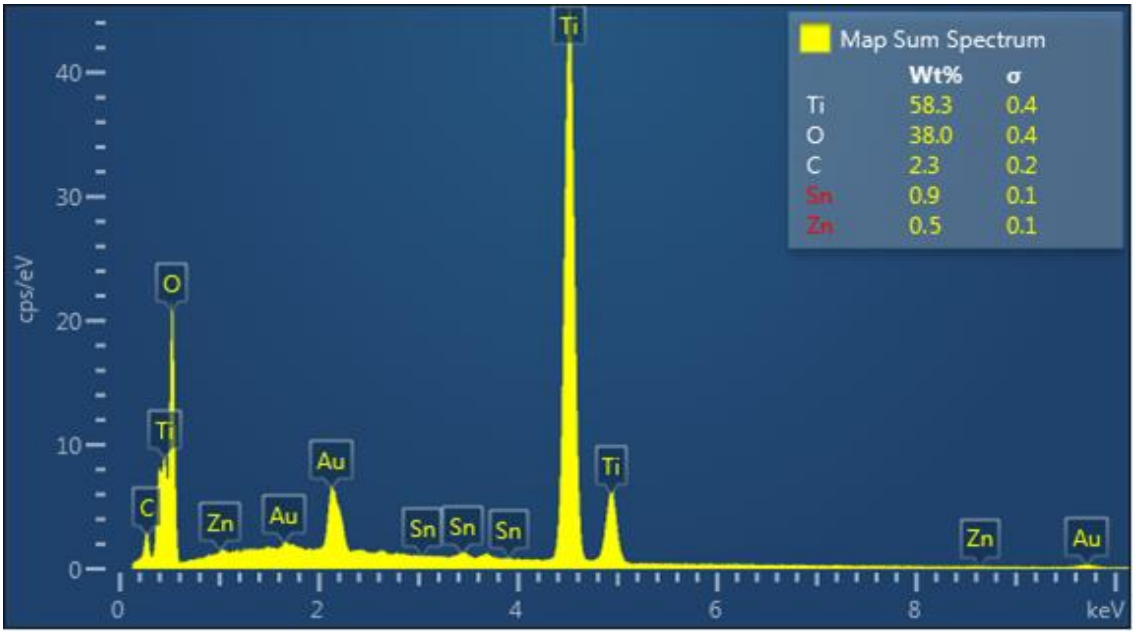

Figure 4.22. EDX result of ZnO seed layer on TiO_2 NRs.

ZnO NRs were growth on the ZnO seed layer using hydrothermal methods at 363K for 2 h. The EDX analysis is carried out to identify the elemental composition of the prepared optical electrode, and the EDX spectrum has been shown in Figure 4.23 The optical electrode is clearly shown in the EDX spectrum and no other impurities were found. Zn concentration was increased compared with Figure 4.22.

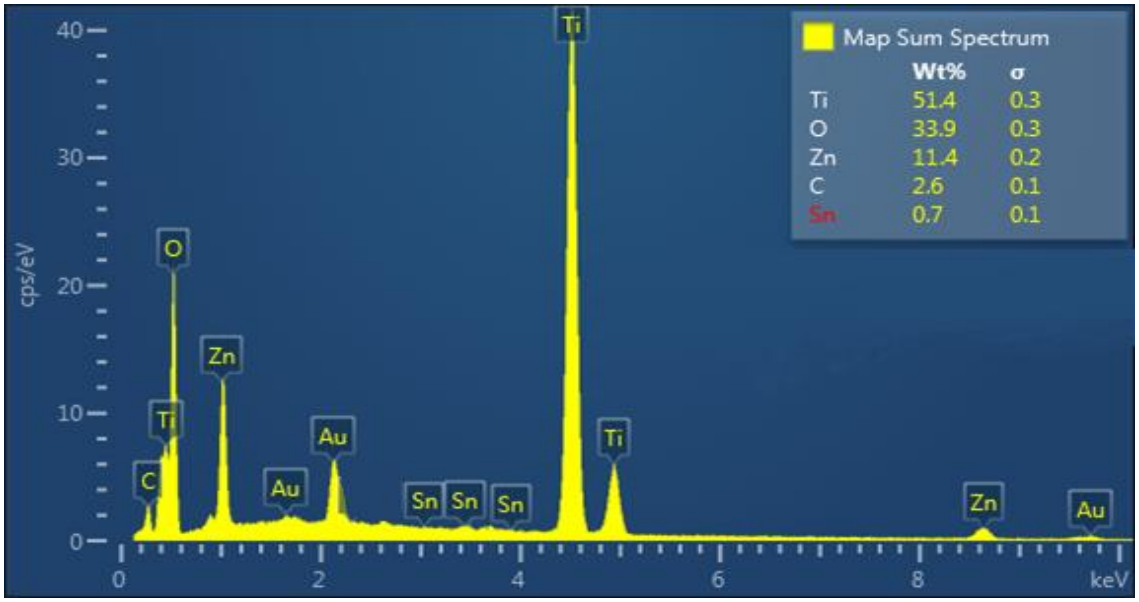

Figure 4.23. EDX result of MWCNT-ZnO/TiO_2 NRs FTO.

SEM image of MWCNT-ZnO/TiO_2/FTO sample is depicted in Figure 4.24, revealing the typical ZnO NRs. It was observed that the morphology of ZnO is a rods shape and the crest of the ZnO NR has a hexagonal shape. It can also be shown that the NRs have an average diameter of 94.9 nm and an average length of 1.98 µm in all four samples. Moreover, the ZnO NRs were uniform distributed on the tops of TiO_2 NRs which lead to increasing the thickness of the optical electrode as presented in Figure 4.25.

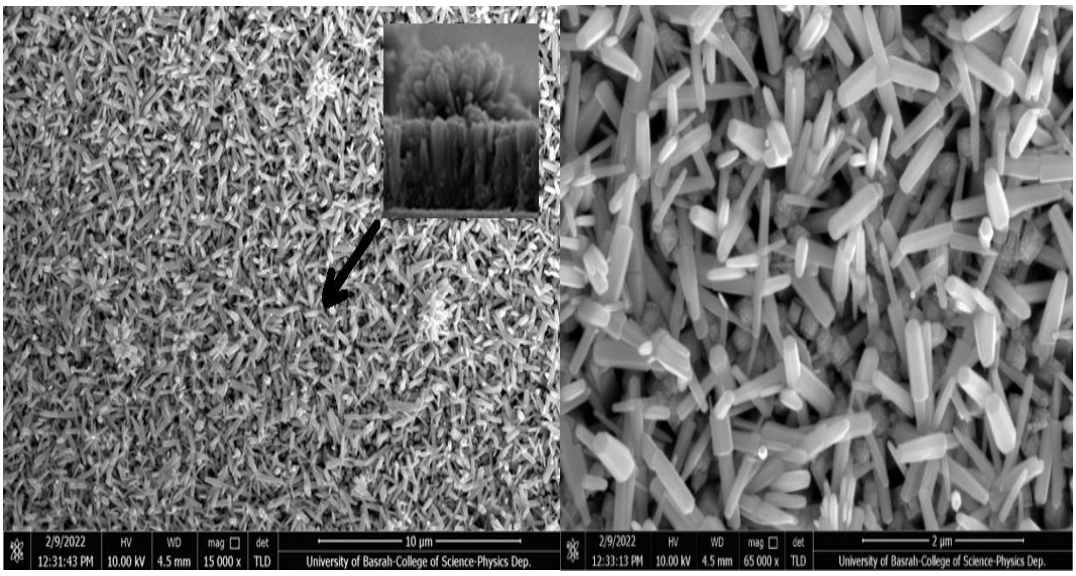

Figure 4.24 SEM image of MWCNT-ZnO/TiO_2/FTO.

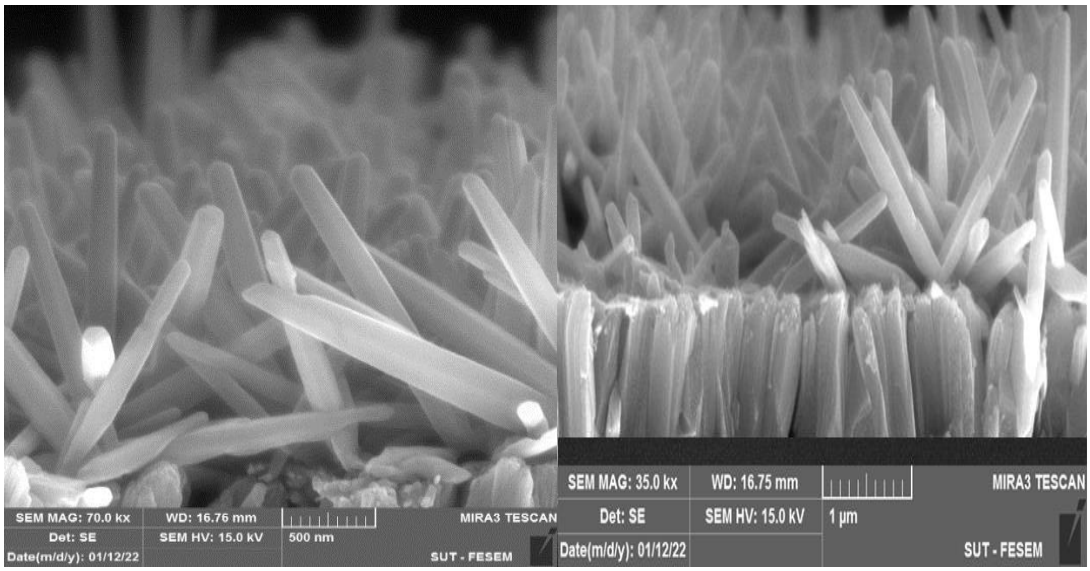

Figure 4.25. Cross section of MWCNT-ZnO/TiO_2/FTO.

Figure 4.26 depict the histogram chart of NRs diameter distribution. The minimum, maximum, and mean diameter of the ZnO in all four samples are (25.1, 213.9 and 94.9) nm respectively.

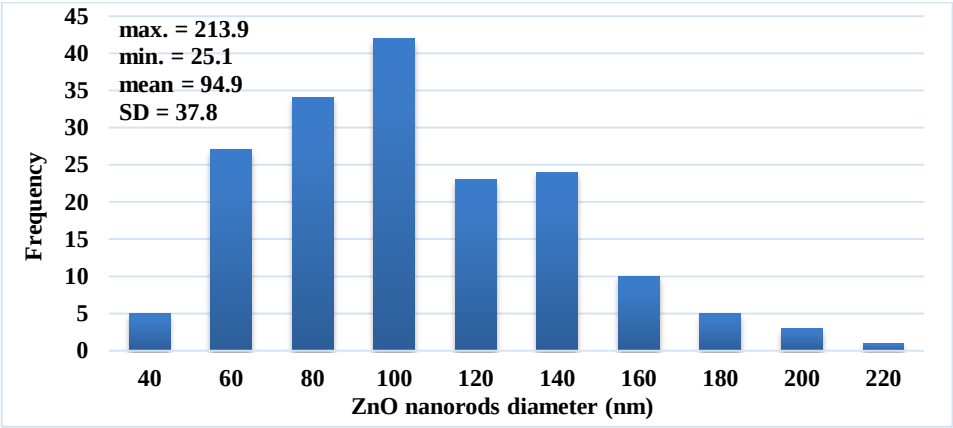

Figure 4.26. The histogram chart of ZnO NRs diameter distribution.

4.3.5 Optical properties of TiO_2 NRs

The optical properties of synthesized TiO_2 NRs on FTO substrate are shown in Figure 4.27 using a hydrothermal method with different HCl concentration. It was reported that the absorbance of TiO_2 films decreases with increasing the HCl concentration and the etching time. The absorbance of TiO_2 depends on the film thickness and particle size. Where the absorbance of material increases with increasing the film thickness [182,183]. The presence of absorption spectrum for prepared TiO_2 films is well agreement with the Mahadik report [184]. The findings in this work showed that TiO_2 NRs absorbance decreases with increasing the incident photons wavelength. Wherefore, the absorbance spectra of TiO_2 can be classified into three regions: The first one at $\lambda<390$ nm is called the high absorption region [56,185]. The second one is the optical window of the optical electrode, located at $\lambda > 400$ nm. The optical electrode must be high transparency in the optical window. Finally, the absorption edge was placed between ($390 < \lambda < 420$) nm [185]. The threshold of charge transition between VB and CB corresponds to the

absorption edge of semiconductors. The optical band of the films can be estimated using Tauc equation, according to inter-band absorption theory [186,187].

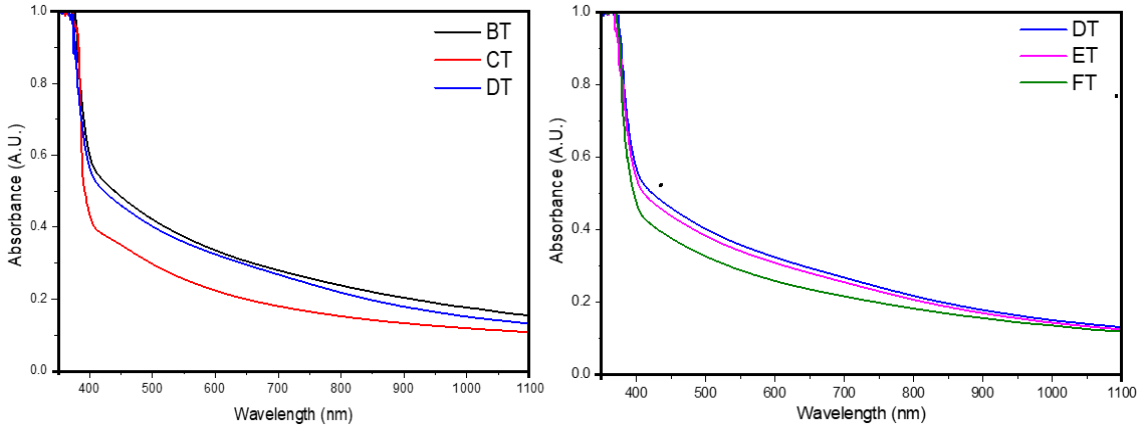

Figure 4.27. Absorbance spectrum of TiO_2 NRs/FTO.

Figures 4.28 and 4.29 show the physical relation of $(\alpha h\nu)^2$ with photon energy ($h\nu$). These curves data were calculated and plotted depending on TiO_2 NRs film transmittance spectrum. For example, it can be extracted by the start of TiO_2 NRs optical transition near the band edge, which is equal to the value of intercept of fitted line. This figure shows the comparison of Eg values of TiO_2 NRs films with different HCl concentration and etching time. TiO_2 NRs Eg obtained to be 3.07 eV increased to 3.127 eV with decreasing the HCl concentration while the etching led to increase the optical band gap from 3.13 eV to 3.156 eV as listed in Table 4.5. As reported in XRD and FESEM results, the HCl concentration and the etching led to decrease the particle size of TiO_2 NRs. Eg is inversely proportional to the particle size [188], so there is systematic blue shift in the absorption edge with the decrease in particle size due to quantum size effect of TiO_2 NPs [189,190]. These results confirmed the XRD and FESEM results. Also, it was agreeing with values reported by other researchers in literature.

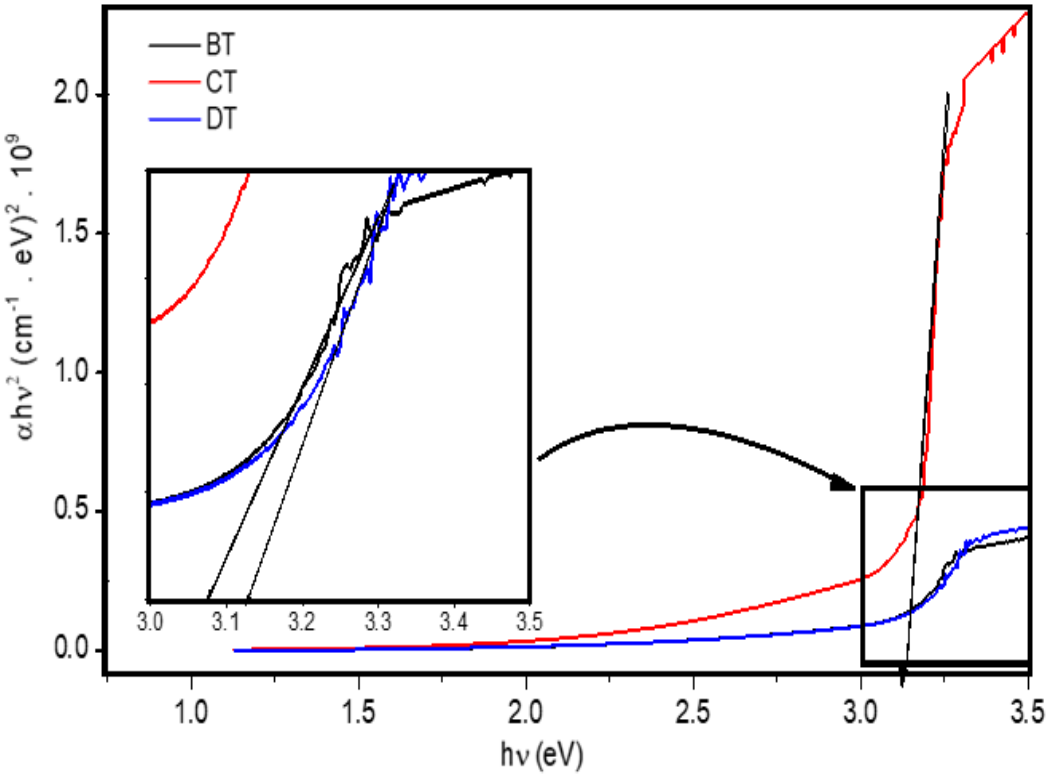

Figure 4.28. Direct band gap plot of TiO_2 films with difference HCl concentration.

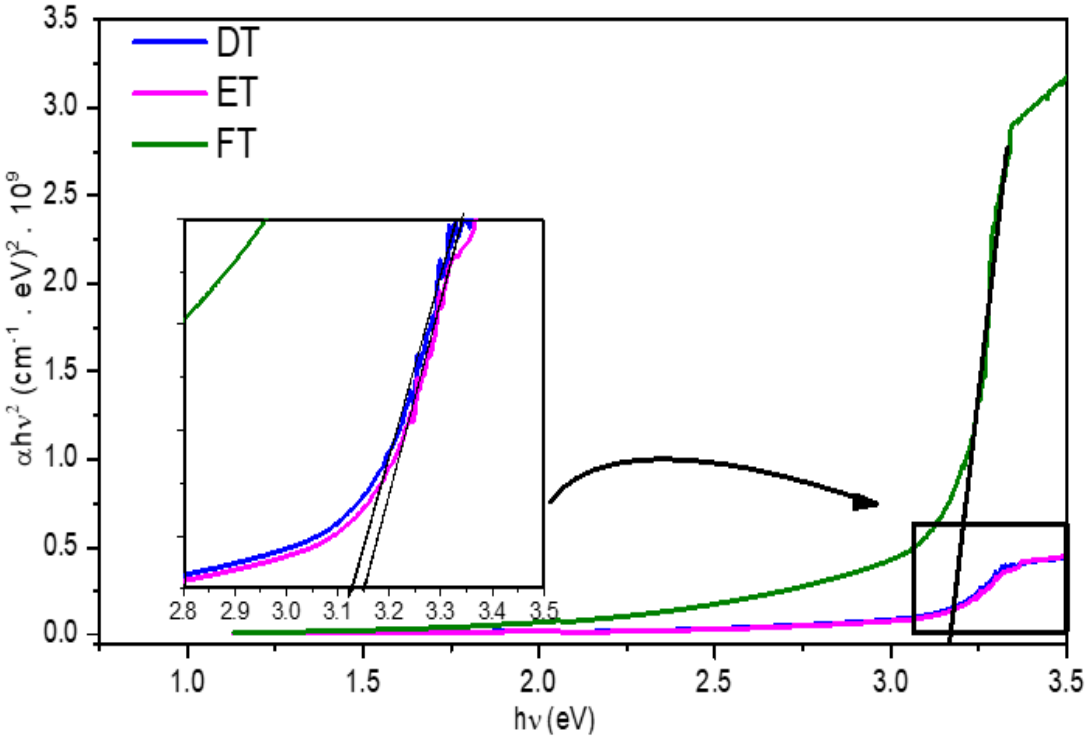

Figures 4.29. Direct band gap plot of TiO_2 with different etching time.

Table 4.5. Optical energy gap of TiO_2 NRs films.

Sample	Optical energy gap (eV)
BT	3.078
CT	3.143
DT	3.127
ET	3.146
FT	3.156

4.3.6 Optical properties of MWCNT-ZnO/TiO_2

The absorbance spectra of TiO_2/FTO (sample ET) and ZnO/TiO_2/FTO with different MWCNT weighting percentage 0, 0.5, 1, 1.5 % is shown in Figure 4.30. The figure displays TiO_2 sheets absorption bands which exhibited obvious changes after ZnO coating. The absorbance on the optical electrode increased with increasing of the MWCNT weighting percentage. In addition, it seems that by increasing the MWCNT content in the optical electrode films the threshold absorption wavelength increased.

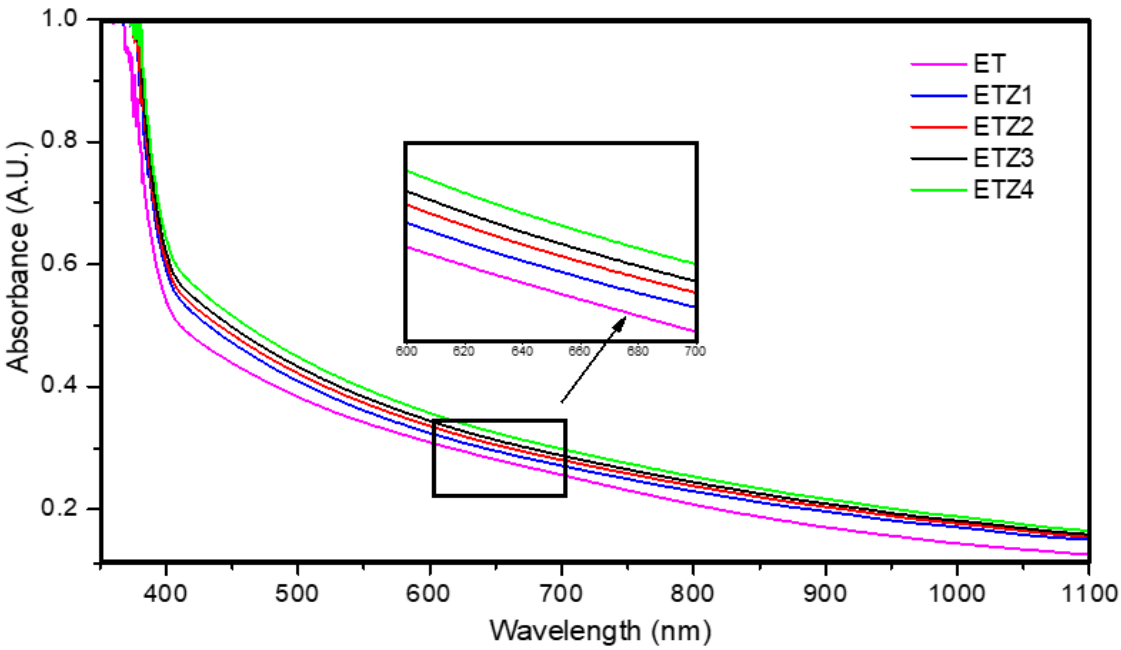

Figure 4.30. UV-vis absorbance spectra of MWCNT-ZnO/TiO_2.

MWCNT-ZnO/TiO_2 films Eg values were calculated by *Tuac'* relation. The previous reports indicated that the direct transitions are possible for these samples [191–193]. Figure 4.31 shows $(\alpha h\nu)^2$ versus hν plots. It is clearly observed that the ZnO growth on TiO_2 NRs leads to increase the optical electrode Eg. The increase in band gap may be attributed to the formation of new energy levels due to incorporation of ZnO NRs onto TiO_2 NRs which can be explained by the band theory [194]. A spectral shift in the band gap of the ZnO/TiO_2 NRs can be caused by the presence of native defects. Where Zn is more electronegative 0.14 eV versus ~0.07 eV which is higher for ZnO than rutile TiO_2 [195]. This difference in electronegative may lead to the above native defects and oxygen vacancies extended defects levels which shift CB upward and VB downward resulting in a bandgap expansion [193]. It is obvious that the optical electrode Eg reduces with MWCNT content increases. The decrease in energy gap is due to increasing the disorder degree in the MWCNT matrix [57]. The obtained values of the energy gap are tabulated in Table 4.6. In another way, it can be studied the effectiveness of insetted the MWCNT into ZnO seed layer on defect tail.

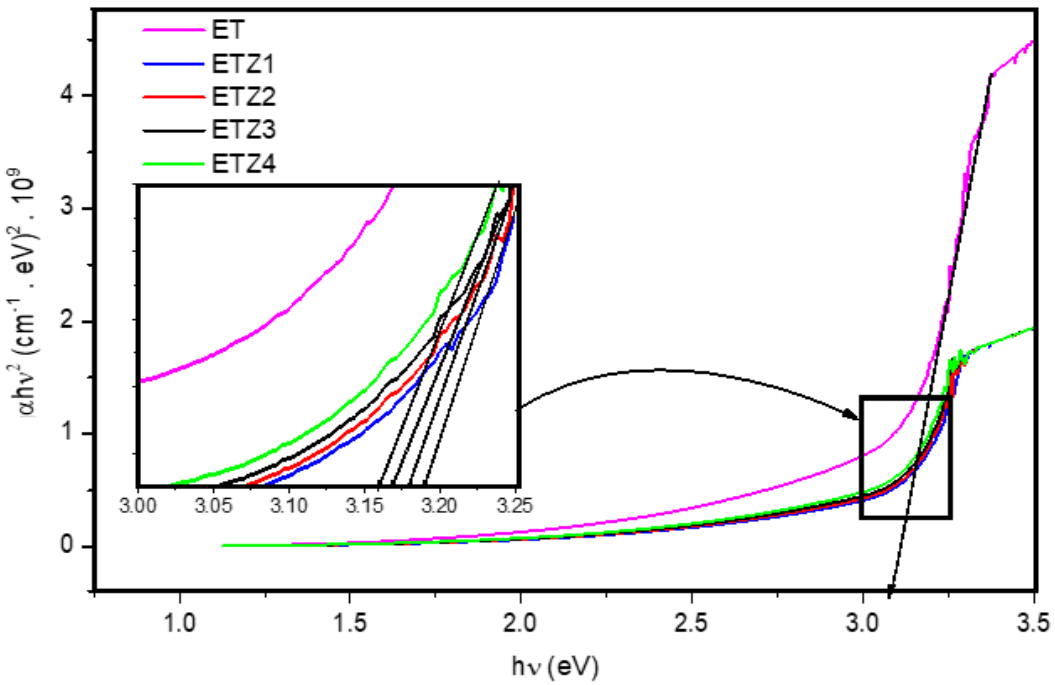

Figures 4.31. Direct band gap plot of MWCNT-ZnO/TiO_2 films.

Table 4.6. Optical energy gap of MWCNT-ZnO/TiO_2 films.

Sample	Optical energy gap (eV)
ET	3.146
ETZ1	3.189
ETZ2	3.18
ETZ3	3.168
ETZ4	3.159

The defect tail is known as the Urbach tail, and the energy associated with this defect tail is referred to as Urbach energy (E_U) [196]. The Urbach tail (E_U) of the composites is determined from the linear slope of the curves Lnα vs the photon energy (hυ), and by using the equation [193,197,198].

$$\alpha = \alpha_o \mathrm{EXP}(\frac{E}{E_U}) \qquad (2)$$

Where α , E_U and E are the absorption coefficient, Urbach energy, and photon energy respectively [199,200].

Urbach energy (E_U) was calculated for the MWCNT-ZnO/TiO_2 samples by plotting ln α vs. photon energy as shown in Figure 4.32. The inverse of the slope of the line below the band gap of the material provided the value of Eu.

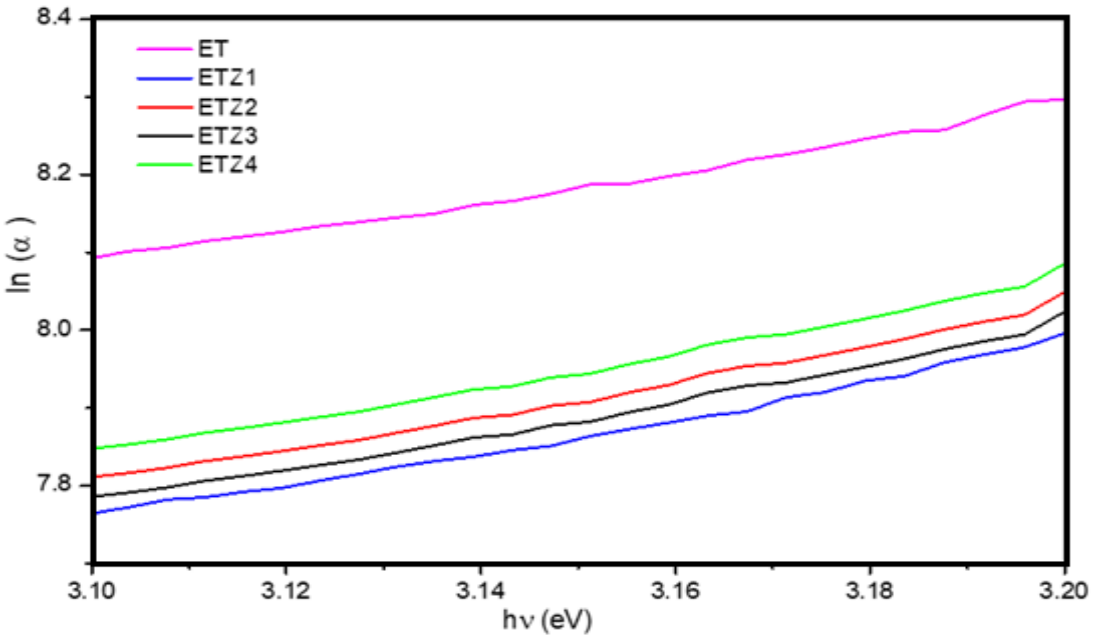

Figures 4.32. Plots of ln(α) vs. Photon energy (hυ) of MWCNT-ZnO/TiO_2 samples.

MWCNT-ZnO/TiO_2 Urbach energy is inversely proportional with the optical energy gap as listed in Table 4.7. The insetted of the MWCNT inside ZnO NPs leads to create sub-band state inside Eg. Therefore, the magnitude of defect energy increases then sub-band state increased. These behaviors play an important role to decreases the band gap energy. This clearly supports our argument that sub-band states formed between the valence and CBs result in the narrowing of the band gap.

Table 4.7. Urbach energy (E_U) of MWCNT-ZnO/TiO_2 samples.

Sample	E_U (meV)
ET	444
ETZ1	381
ETZ2	385
ETZ3	389
ETZ4	394

4.4. Fourier Transform Infrared Spectroscopy

FTIR Analysis provides information on molecular structure and oxygen functional groups formed on MWCNTs surface. The comparative spectra for MWCNTs and F-MWCNTs are shown in Figure 4.33, where typical FTIR spectra of them can be clarify briefly. There are three bands at 749, 879 and 1149 cm^{-1} associated with the vibration of the carbon skeleton (C-C) of CNT. Also, two bands at 1396 and 1446 cm^{-1} are associated with the vibration of (C=C-C) Aromatic ring stretch. The two bands at 1637 and 1670 cm^{-1} are corresponding to vibration of (C=C), originated from the surface of tubes (12). While f-MWNT revealed a different surface chemistry of MWCNTs. It can be observed the weak peak around 3170 cm^{-1}, which can be assigned to stretching vibrations of O-H stretch groups [201]. Moreover, another weak peak around 1728 cm^{-1}, which can be assigned to stretching vibrations of N-H bend groups Compared with the IR spectra of MWCNTs, the two bands around 1637, 1670 cm^{-1} are lower in the composite than those of pure MWCNTs. The result suggested that the surface of MWCNTs has been covered almost of surface-active sites by O and NH_3. Furthermore, the peak observed at about 3560 cm^{-1} in Figure 4.33.b is assigned to NH_3 formation. Furthermore, the use of nitric acid in the process causes a purity improvement. Number of functional groups should decrease after purification with a stronger power of nitric acid. The washeing with distilled water several times leads to decrease the 400 -600 cm^{-1}. Also reducing the intensity of peak elucidates presence large number of asymetrical hexagonal carbon.

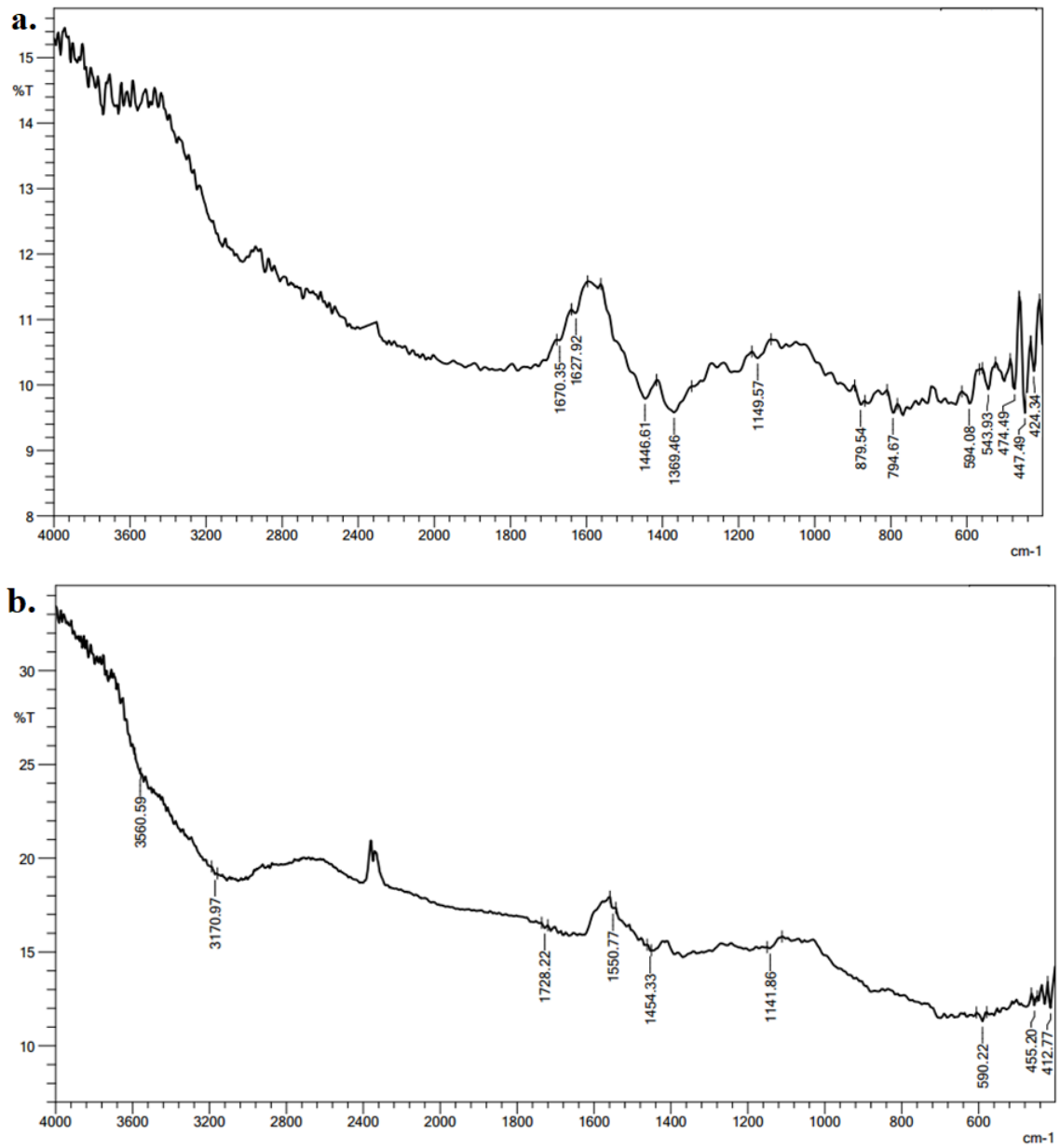

Figure 4.33. FTIR spectra of (A) MWCNT, (B) f-MWCNT.

4.5 Performance of DSSCs

DSSCs performance has been obtained using a solar cell system under simulated AM 1.5 sunlight at 100 mW/cm^2 light intensity. The solar cell performance system consists of a Xenon lamp used as a light source and Keithley 2450 to measure I-V curve. The active area of photoanode was appointed to be 0.16 cm^2 for all samples. Furthermore, all J-V results were obtained at room temperature.

4.5.1 J-V characterization of TiO_2 with different Pt concentrations

J-V characterization of TiO_2 with different Pt CEs was measured initially to select the optimum results of CE. Also, these results are important for reducing production costs by reducing the required amount of expensive platinum. Moreover, higher transmittances recorded for the photo fabricated Pt CEs make them suitable for use in bifacial DSSCs. Bifacial DSSCs can be deployed as building windows and integrated electronic devices.

A. Single layer front illumination

The fabricated solar cells J-V results with different Pt precursor concentrations (single layer) are shown in Figure 4.34. This figure illustrates that the increase in the Pt precursor concentration leads to an increase of the solar cell efficiency 1.666, 2.067, 2.96 and, 2.96 for Pt2.5, Pt5, Pt10 and, Pt15, respectively. V_{oc} of all samples remained constant at 0.7 V hence it depends on e^- transition in the photoelectrode CB, HOMO and LUMO level of dye and Fermi potential of electrolyte [107,202]. Whereas, the major contribution of efficiencies enhancement was obtained from the photocurrent. The fabricated solar cells I_{sc} was increased with increasing Pt precursor concentrations 3.555, 4.413, 6.011, 6.224 mA for Pt2.5, Pt5, Pt10 and, Pt15, respectively as listed in Table 4.8. Meanwhile, higher J_{sc} is obviously due to the higher catalytic ability for I_3^- reduction for Pt thin film, resulting from increasing the surface area with an increase Pt precursor concentration [203]. As well as platinum is properly dispersed on the surface of FTO.

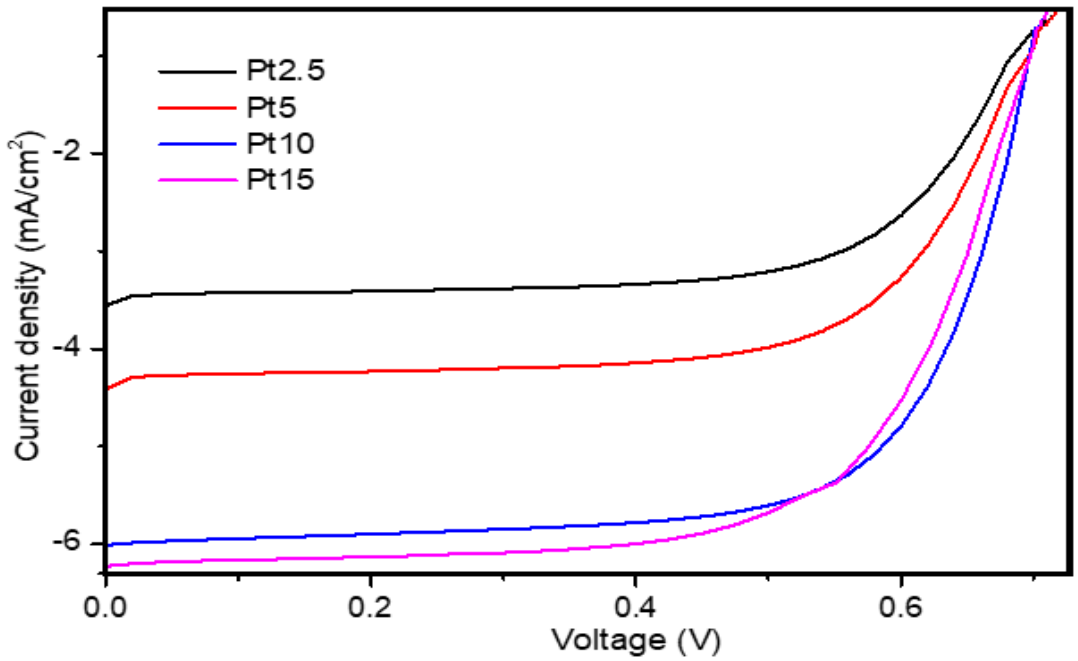

Figure 4.34. J-V curves of the DSSCs based on TiO_2 NR PEs with single layer Pt CEs for front illumination.

Table 4.8. PV properties of DSSCs made of single layer Pt CEs for front illumination.

Sample ID	J_{sc} (mA/cm^2)	V_{oc} (V)	η	FF
Pt2.5	3.555	0.700	1.666	0.669
Pt5	4.413	0.700	2.067	0.669
Pt10	6.011	0.700	2.960	0.703
Pt15	6.224	0.700	2.960	0.679

B. Single layer rear illumination

The transparency of the photo fabricated Pt CE can be determined using the rear illumination test. Figure 4.35 shows the curves of J-V results of the fabricated Pt thin film with different H_2PtCl_6 precursor concentrations. From this Figure it was found that the efficiency of the

fabricated cell in the rear illumination decreased as compared with the front illumination which is due to decrease the photocurrent density.

This reduction in photocurrent density can be ascribed to the incident light radiation from CE to the dye sensitizer where the electrolyte layer in the cell will behave as a barrier between the incident light radiation and the dye sensitizer. The electrolyte is known to reflect incident light away, thereby reducing the amount of light available for the photoexcitation of the dye molecules.

Moreover, the efficiency of the fabricated solar cell in the rear illumination was increased with increasing Pt precursor concentrations. Whereas, the ratio of the rear illumination efficiency to the front illumination efficiency (η_R) was decreased as given in Table 4.9. This is due to the reduced photocurrent density of the rear illuminated where the Pt films act as the mirror. The light-reflecting properties of the metallic Pt layer were increased with an increase in the Pt precursor concentrations. These results were confirmed by the transmittance properties of the Pt films.

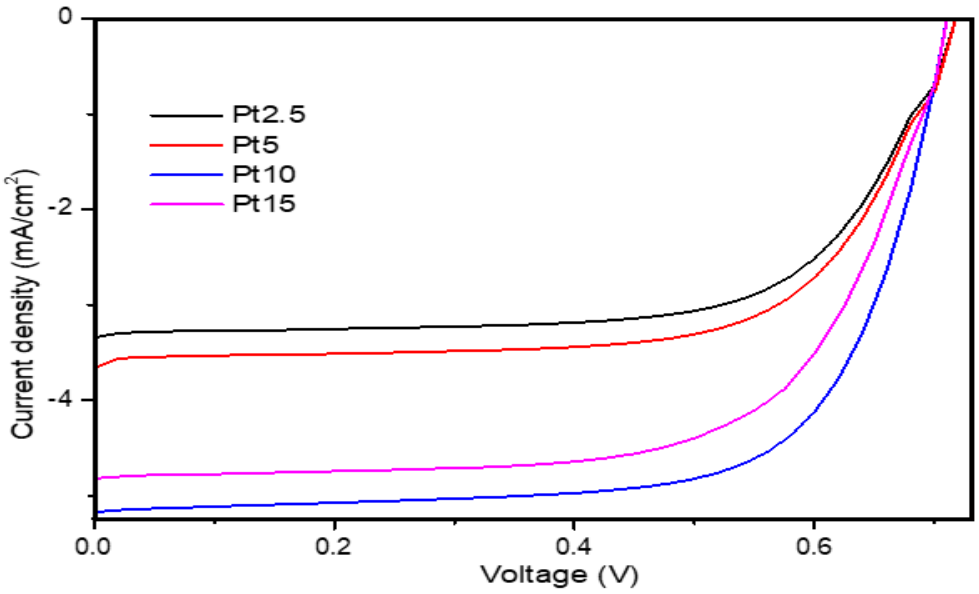

Figure 4.35. J-V curves of DSSCs based on TiO_2 NR PEs with single layer Pt CEs for rear illumination.

Table 4.9. PV properties of DSSCs made of single layer Pt CEs for rear illumination.

Sample ID	J_{sc} (mA/cm^2)	V_{oc} (V)	η	FF	η_R
Pt2.5	3.341	0.700	1.481	0.633	0.889
Pt5	3.663	0.700	1.716	0.669	0.830
Pt10	5.169	0.700	2.440	0.674	0.824
Pt15	4.817	0.700	2.259	0.670	0.763

C. Double layers front illumination

J-V results of fabricated solar cells with different Pt precursor concentrations (Double layer) are shown in Figure 4.36. This figure shows that the increase in the Pt precursor concentration leads to gradually decrease the solar cell efficiency 2.956, 2.938, 2.891 and 2.816 for DPt2.5, DPt5, DPt10 and, DPt15, respectively. Where V_{oc} remained constant at 0.7 V in each sample. I_{sc} of fabricated solar cells was increased with increasing Pt precursor content (3.555, 4.413, 6.011, 6.224) mA as listed in Table 4.10. The light reflecting properties of the metallic Pt layer reflects the unabsorbed light to the photoanode may lead to enhance the I_{sc}. Another reason for the increase in I_{sc} is the increase of surface area with an increase in Pt precursor content. They would exhibit higher charge transport ability and better electrocatalytic activity for I_3^- to I^- reduction [77]. I_{sc} has increased as the cell efficiency decreased. This behavior can be explained by increasing the surface resistance of the Pt films, which leads to increasing R_s. The effect of R_s on FF and the solar cell efficiency is very strong, but I_{sc} is unaffected by R_s stance. Moreover, R_s does not affect the solar cell at V_{oc} since the overall current flow through the solar cell, and therefore

through R_s is zero. However, near V_{oc}, I-V strongly affected by R_s [145,204].

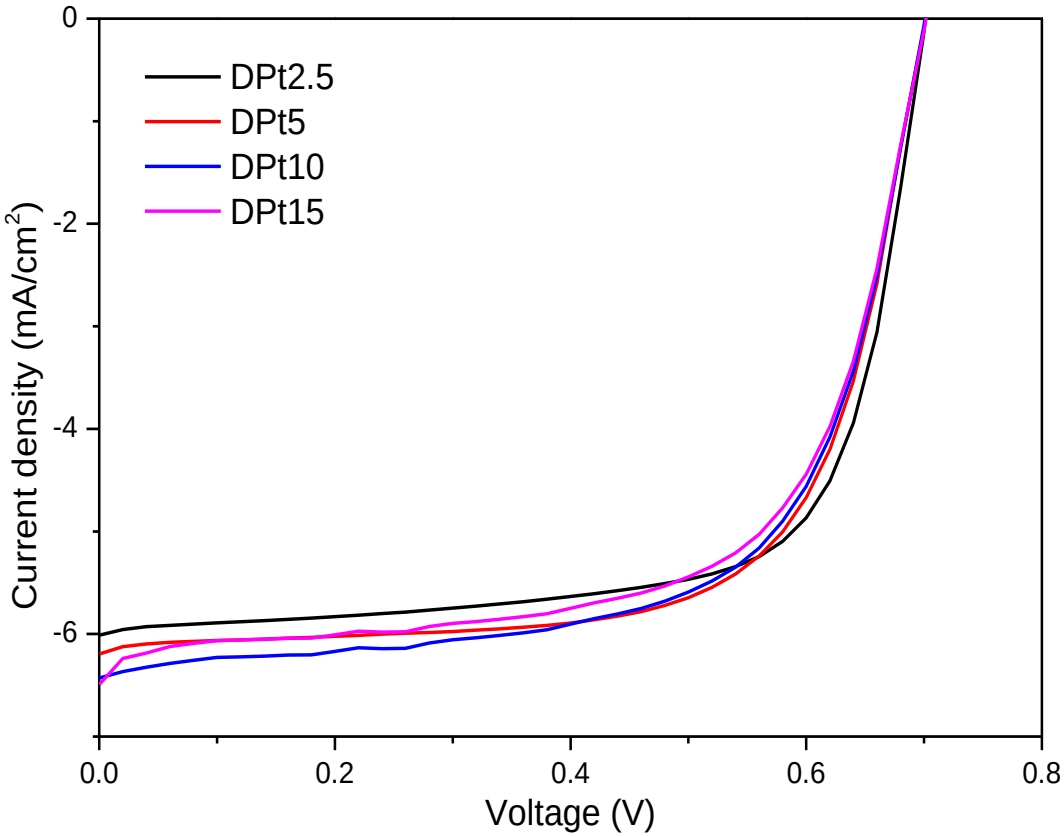

Figure 4.36. J-V curves of the DSSCs based on TiO_2 NR PEs with double layers of Pt CEs for front illumination.

Table 4.10. PV properties of DSSCs made of double layers Pt CEs for front illumination.

Sample ID	J_{sc} (mA/cm^2)	V_{oc} (V)	η	FF	R_s (Ω)
DPT 2.5	6.011	0.700	2.956	0.702	124.017
DPT 5	6.194	0.701	2.934	0.676	129.563
DPT 10	6.440	0.700	2.891	0.641	133.208
DPT 15	6.492	0.701	2.816	0.619	137.789

D. Double layers rear illumination

Figure 4.37 shows the J-V results of fabricated Pt thin film with different H_2PtCl_6 precursor concentrations. From this Figure, it was found that the efficiency of the fabricated cell in the rear illumination decreased as compared with the front illumination which is due to a decrease in the photocurrent density. In addition, the increase of the precursor concentrations leads to decrease the ratio of the rear illumination efficiency to the front illumination efficiency (ηR) as listed in Table 4.11.

These results correspond with the transmittance of the Double layers Pt films where it was decreased with an increase in the Pt precursor concentrations. Therefore, the transmitted light intensity was decreased. Furthermore, transmitted light intensity plays an important role in which faster electron diffusion can be obtained at higher light intensities [81]. For this reason, the ratio of the rear illumination efficiency to the front illumination efficiency (ηR) was decreased.

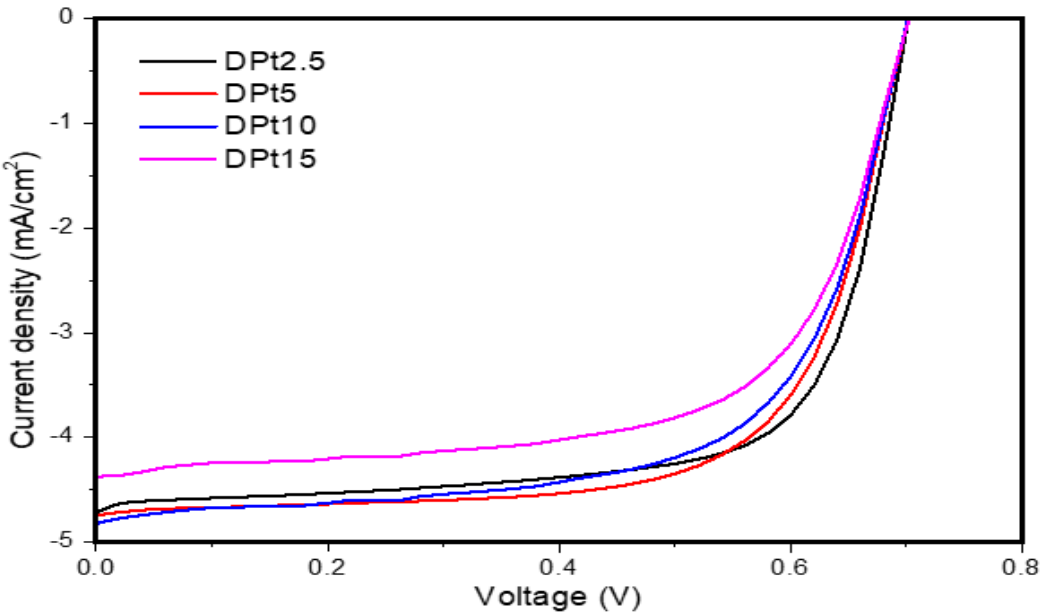

Figure 4.37. J-V curves of the DSSCs based on TiO_2 NR PEs with double layers Pt CEs for rear illumination.

Table 4.11. PV properties of DSSCs made of double layers Pt CEs for rear illumination.

Sample ID	J_{sc} (mA/cm^2)	V_{oc} (V)	η	FF	η_R
DPt 2.5	4.716	0.700	2.298	0.696	0.778
DPt 5	4.747	0.701	2.259	0.679	0.770
DPt 10	4.830	0.700	2.168	0.641	0.750
DPt 15	4.376	0.701	1.971	0.643	0.700

E. Double layers vs single layer performance.

The Pt thickness on the FTO substrate is significant and dominates DSSC performance. This viewpoint contradicts with previous reports illustrating that the thickness of Pt film is insignificant for DSSC performance. The double layers of the Pt films lead to an increase in the film thickness. Figure 4.38 shows the solar cell efficiency of the single and double layers of the DSSCs made of Pt CEs for front illumination with different precursor concentrations. The increase in the number of layers which are leads to an increase in the film thickness. Therefore, the time of the electron transport between CE and the FTO will be increased [71,205]. In general, the duration for the electron injection process occurred within a few femtoseconds for a Ru-complex dye attached to TiO_2 photoanode. This duration should be compared with the decay of the dye excited state, S* to the ground state, S (Mechanism 6 - recombination event). The lifetime of S* was reported around 20 to 60 ns [81]. Therefore, the increase in electron transport time leads to increase the recombination process.

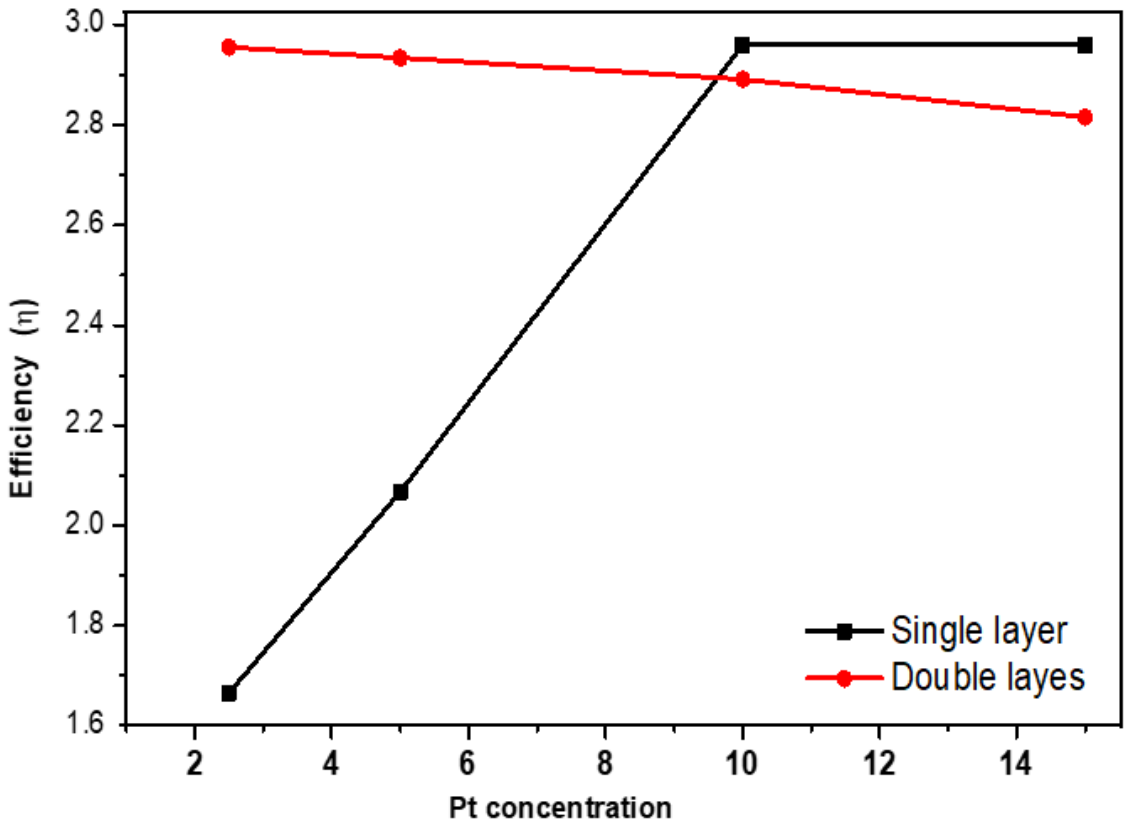

Figure 4.38. The solar cell efficiency of the single and double layers of the DSSCs made of Pt CEs for front illumination.

4.5.2 J-V characterization of TiO_2

The J-V characterization results of synthesized TiO_2 NRs on FTO substrate are carried out using the fabricated solar cell performance system. Figure 4.39 shows the J-V results of TiO_2 films prepared on FTO substrates using a hydrothermal method with different HCl concentration and the etching time. These results reported that the conversion efficiency of the highly effected by the preparation condition parameter where the solar cell efficiency of the fabricated cell are 2.067, 0.889, 2.959, 3.255 and 1.389 for BT, CT, DT, ET and FT respectively. While the open-circuit voltage (V_{oc}) of all samples remained constant at 0.7 V except sample (CT) recorded at (0.68 V) due to the fact that the sample (CT) which has a low thickness and high grain size which lead to increase the recombination process of the electron in TiO_2 CB with electrolyte energy level [206]. J_{sc} is directly proportional to the solar cell

efficiency of the fabricated cell. J_{sc} is affected by several factors as dye molecular structure, amount of dye adsorbed on photoanode, and electrochemical properties of photoanode in the presence of electrolyte [207,208]. Therefore, the variation of the J_{sc} was observed from the modification of TiO_2 structure where the modification of TiO_2 electrode structure increased the internal surface area of the electrode to allow a large enough amount of dye to be contacted simultaneously by the TiO_2 electrode and the electrolyte. As a result, Photo-electron excitation was increased which led to increasing J_{sc}. Therefore, large surface area for dye absorption is the basic requirement for photoanode material [209]. These results are strengthening the SEM results of TiO_2 NRs where the HCl concentration was used to control the number of TiO_2 rods per unit area whereas the etching time led to increase the porosity of the TiO_2 NRs. The I-V parameters such as V_{oc}, J_{sc}, FF, and cell (η), R_s and R_{sh} are estimated from the J-V curves a tabulated in Table 4.12.

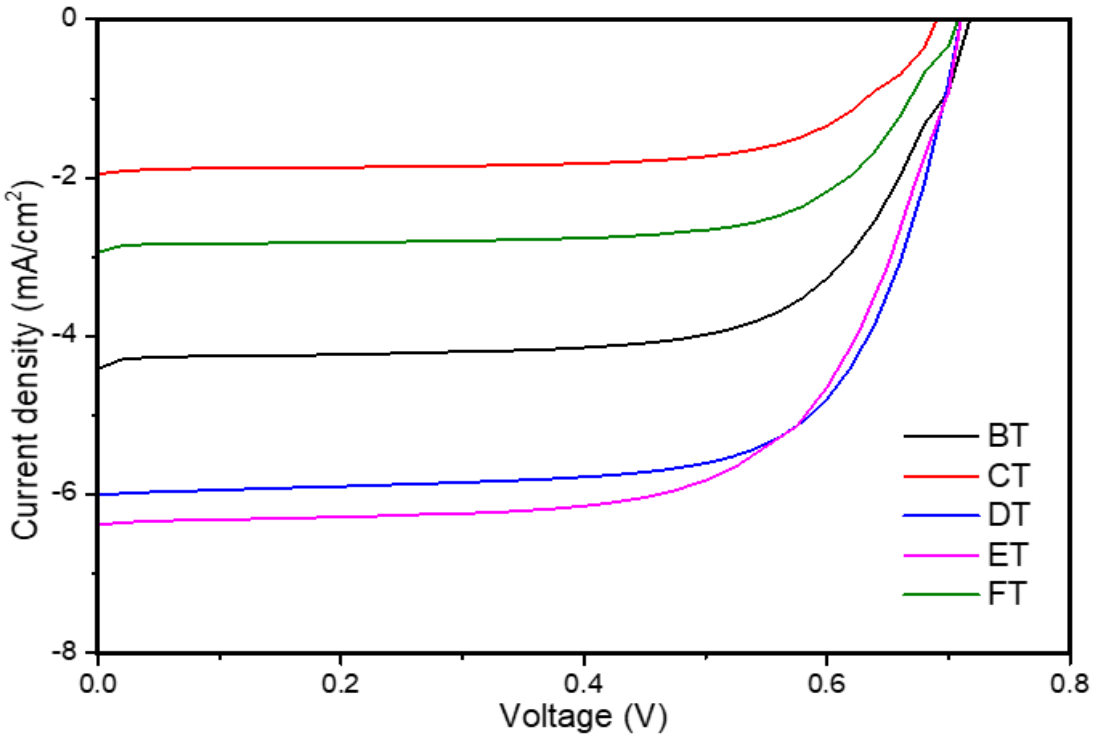

Figure 4.39. J-V curves of the DSSCs based on TiO_2 NR PEs.

Table 4.12. DSSCs parameters of TiO_2 NR PEs.

Sample ID	J_{sc} (mA/cm^2)	V_{oc} (V)	J_m (mA/cm^2)	V_m (V)	η	FF	R_s (Ω)	R_{sh} (Ω)
BT	4.413	0.700	3.690	0.560	2.068	0.669	251.6	9663.8
CT	1.952	0.680	1.646	0.540	0.889	0.670	552.2	20660.7
DT	6.011	0.700	5.285	0.560	2.960	0.703	152.1	12411.9
ET	6.381	0.700	5.906	0.551	3.255	0.729	163.2	13526.9
FT	2.942	0.700	2.481	0.560	1.390	0.675	317.2	13885.7

Additionally, FF is yet another important parameter that reflects the quality of solar cells. FF is a measure of the squareness of the curve, which are used to determine efficiency (η). FF was improved from 0.669 to 0.729 Therefore; the length of TiO_2 NRs significantly improved the performance of DSSC including J_{sc}, V_{oc}, and FF [95,144]. For DSSC, large surface area meant more dye molecules could be attached on TiO_2 NRs, which would be tremendously increased the current density. The improvement of FF indicated that the recombination between electron and holes, and scattering during electron transportation were less [210–212]. Finally, increasing the shunt resistance and decreasing the series resistance as well as reducing the overvoltage for diffusion and electron transfer will lead to a higher FF value, thus resulting in greater efficiency and pushing the output power of the solar cell [213,214].

4.5.3 J-V characterization of MWCNT-ZnO/TiO_2

J-V characterization of synthesized ZnO-MWCNT/TiO_2 on FTO substrates are carried out using the fabricated solar cell performance system. Figure 4.40 illustrates the J-V curves of ZnO-TiO_2 NRs prepared on FTO substrates using a hydrothermal method with

different MWCNT weighing concentrations. DSSC constructed with ZnO based photoanode shows remarkably improved J_{sc} of 6.562 mA cm^{-2}، V_{oc} of 700 mV and hence the highest PV conversion efficiency of 3.938 % to be quite good compared to the bare TiO_2 NRs 3.255%. This improvement was result of a moderate enhancement in current density which can be explained by the increased absorption due to the increase in the number of dye molecules adsorbed onto the ZnO surface [214].

The incorporation of ZnO a nano rods into the TiO_2 structure improved the electron transfer and facilitates the charge carrier separation due to the higher electron mobility of ZnO [51]. Moreover, the improvement observed with one dimensional structure like NRs are due to the unhindered direct pathways for fast electron transport to the collector electrode and further, the decrease in the probability of electron recombination reactions [215]. In addition, the energy levels of the ZnO are slightly higher than those of TiO_2 So, photoelectrons flow from the CB of ZnO towards the CB of TiO_2 and holes diffusion towards the VB of ZnO [216].

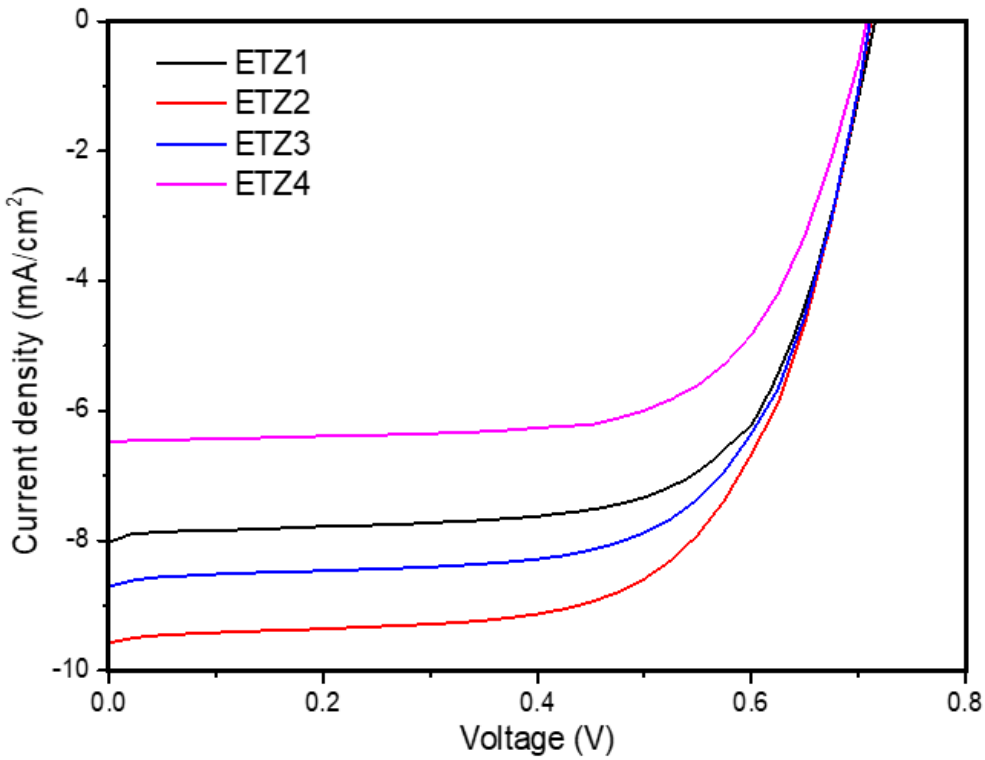

Figure 4.40. J-V curves of the DSSCs based on ZnO-MWCNT/TiO_2 PEs.

Figure 4.40 was also provided the J-V curves illustrated the effectiveness of insetted the MWCNT into ZnO seed layer on the DSSC performance. The solar cell efficiency of the fabricated cell is 3.938, 4.358, 4.047 and 3.203 for ETZ1, ETZ2, ETZ3 and ETZ4 respectively. At the best conditions, the incorporation of MWCNTs at 0.5 wt% in the ZnO films increases the conversion efficiency by approximately 10% compared to 0 wt% DSSCs. The strong enhancement in J_{sc} of the DSSCs with 0.5 wt% MWCNTs suggests that MWCNTs should play an important role in enhancing the conductivity and the electron transport between the ZnO and TiO_2 nanostructure.

However, at higher MWCNT contents, the solar conversion efficiencies decrease, which should be explained by the solar energy loss from the optical absorption of the carbon materials. This result in a lower initial photocurrent generated by the dye molecules, hence a lower current measured in the external circuit [217]. Moreover, the

reduction in PV performance further increase in the MWCNT content up to 1% can be explained by a reduction in light transmittance and photon energy loss of the photoanodes due to optical absorption properties of MWCNT competing with the dye molecules, resulting in a decrease in charge collection and cell efficiency [201].

Finally, the insetted of MWCNT materials in the ZnO linking layer exhibit both positive and negative influence on PV performance of DSSCs. On the one hand, the excellent electron conductivity of MWCNT could accelerate electron transfer from TiO_2 NTs to the FTO conductive substrate. The recombination between photoinduced electron and I_3^- in electrolyte is reduced at the same time. It is the reason that J_{sc} value of DSSCs increase as the addition of MWCNT. On the other hand، sunlight is seriously absorbed when it penetrates the films containing high concentration MWCNT materials as shown in Figure 4.30 [114,218].

These results are consistent with UV-vis absorbance spectral. The I-V parameters such as V_{oc}, J_{sc}, FF, η, R_s, and R_{sh} are estimated from the J-V curves listed in Table 4.13.

Table 4.13. DSSCs parameters of ZnO-MWCNT/TiO_2 PEs.

Sample ID	J_{sc} (mA/cm^2)	V_{oc} (V)	J_m (mA/cm^2)	V_m (V)	η	FF	R_s (Ω)	R_{sh} (Ω)
ETZ1	8.05	0.7	6.562	0.6	3.938	0.698	95.1	1193.4
ETZ2	9.284	0.7	7.92	0.55	4.356	0.671	102.1	1308.9
ETZ3	8.611	0.7	7.358	0.55	4.047	0.671	105.4	635
ETZ4	6.348	0.7	5.608	0.55	3.203	0.694	145.4	360.8

4.6 Conclusion

According to the previous dissection and analysis, the following conclusions can be summarized

1. The surface morphology of the Pt films highly effected on the DSSC performance and the increasing of the H_2PtCl_6 concentration leads to decrease the rear illumination efficiency.
2. The acidic medium assistance to provide rutile phase structures with preferred orientations (101) and (002) of TiO_2 samples.
3. ZnO NRs were grown on the (002) plane and the variation of the MWCNT concentration led to shaft the ZnO peak position.
4. The increase of HCl concentration leads to an increase in the rod diameter of TiO_2 NRs and decrease the length as exhibited in SEM Image. While the etching time leads to a decrease in the diameter and length of TiO_2 NRs.
5. The morphology of ZnO was exhibit a rods shape and the crest of the ZnO NR has a hexagonal shape.
6. Sample ET of the TiO_2 nanorods has a high surface area where depending on length to rod diameter which leads to improve the DSSC performance.
7. The DSSC constructed with ZnO/TiO_2 based photo-anode shows remarkably improved efficiency (η) of 20% where improved the electron transfer.
8. The incorporation of MWCNTs in the ZnO seed films increases the energy conversion efficiency 4.358%.

4.7 Future work

1. The most important recommendation for future research is to try to synthesize semiconductors with greater porosity, for increasing dye loading.

2. Examination of the different manufacturing methods for the preparation of the nanostructured TiO_2 electrodes onto FTO concentrating on the study of mechanical and electrical properties of the interface between the TiO_2 film and FTO.
3. Preparation of ZnO NP paste by controlling the solvent ratio, particle and aggregate sizes may be fine-tuned and further optimized. These conditions can be tuned to optimize for different dye and electrolyte combinations.
4. Work on using different natural dyes to improve the performance of DSSC where the natural sensitizers can be an interesting alternative to these ruthenium complexes. The modification of these naturally extracted dyes can be one way of improving the performance and stability of these natural DSSCs.
5. Co-sensitization by different dyes absorbing in various regions of the solar spectrum is another way which can be employed to improve the performance of DSSCs.

References

References

[1] Q. Wang, C. Chen, W. Liu, S. Gao, and X. Yang, *Recent Progress in All-Solid-State Quantum Dot-Sensitized TiO_2 Nanotube Array Solar Cells*, Journal of Nanoparticle Research **18**, 1 (2016).

[2] B. Pickering, F. Lombardi, and S. Pfenninger, *Diversity of Options to Eliminate Fossil Fuels and Reach Carbon Neutrality across the Entire European Energy System*, Joule **6**, 1253 (2022).

[3] D. DeDomenico, *The Ethics and Economics of the World's Energy Consumption*, Academic Festival (2022).

[4] G. B. A. Kumar and Shivashankar, *Optimal Power Point Tracking of Solar and Wind Energy in a Hybrid Wind Solar Energy System*, International Journal of Energy and Environmental Engineering **13**, 77 (2022).

[5] S. P. Tembhare, D. P. Barai, and B. A. Bhanvase, *Performance Evaluation of Nanofluids in Solar Thermal and Solar Photovoltaic Systems: A Comprehensive Review*, Renewable and Sustainable Energy Reviews **153**, 111738 (2022).

[6] Y. K N, P. D. T, S. P, K. S, Y. K. R, S. Varjani, S. AdishKumar, G. Kumar, and R. B. J, *Lignocellulosic Biomass-Based Pyrolysis: A Comprehensive Review*, Chemosphere **286**, 131824 (2022).

[7] T. Kałuża, M. Hämmerling, P. Zawadzki, W. Czekała, R. Kasperek, M. Sojka, M. Mokwa, M. Ptak, A. Szkudlarek, M. Czechlowski, and J. Dach, *The Hydropower Sector in Poland: Historical Development and Current Status*, Renewable and Sustainable Energy Reviews **158**, 112150 (2022).

[8] M. Aghaei, A. Fairbrother, A. Gok, S. Ahmad, S. Kazim, K. Lobato, G.

Oreski, A. Reinders, J. Schmitz, M. Theelen, P. Yilmaz, and J. Kettle, *Review of Degradation and Failure Phenomena in Photovoltaic Modules*, Renewable and Sustainable Energy Reviews **159**, 112160 (2022).

[9] M. M. Rahman, N. Sultana, and E. Velayutham, *Renewable Energy, Energy Intensity and Carbon Reduction: Experience of Large Emerging Economies*, Renewable Energy **184**, 252 (2022).

[10] H. Tian, K. Chen, X. Ye, S. Yang, and Q. Gu, *Hydrothermal Growth of Bi2Ti$_2$O7/TiO$_2$ and Bi4Ti3O12/TiO$_2$ Heterostructures on Highly Ordered TiO$_2$-Nanotube Arrays for Dye-Sensitized Solar Cells*, Ceramics International **45**, 20750 (2019).

[11] S. Aksoy, O. Polat, K. Gorgun, Y. Caglar, and M. Caglar, *Li Doped ZnO Based DSSC: Characterization and Preparation of Nanopowders and Electrical Performance of Its DSSC*, Physica E: Low-Dimensional Systems and Nanostructures **121**, 163963 (2020).

[12] A. M. Mitrašinović, *Photovoltaics Advancements for Transition from Renewable to Clean Energy*, Energy **237**, 121510 (2021).

[13] R. Wolniak and B. Skotnicka-Zasadzień, *Development of Photovoltaic Energy in EU Countries as an Alternative to Fossil Fuels*, Energies 2022, Vol. 15, Page 662 **15**, 662 (2022).

[14] S. Enayati Maklavani and S. Mohammadnejad, *Reduction of Interface Recombination Current for Higher Performance of P+-CZTSxSe(1-x)/p-CZTS/n-CdS Thin-Film Solar Cells Using Kesterite Intermediate Layers*, Solar Energy **204**, 489 (2020).

[15] D. Devadiga, M. Selvakumar, P. Shetty, and M. S. Santosh, *Dye-Sensitized Solar Cell for Indoor Applications: A Mini-Review*, Journal of Electronic Materials **50**, 3187 (2021).

[16] A. Sahu, A. Garg, and A. Dixit, *A Review on Quantum Dot Sensitized*

Solar Cells: Past, Present and Future towards Carrier Multiplication with a Possibility for Higher Efficiency, Solar Energy **203**, 210 (2020).

[17] A. Pandikumar and R. Ramaraj, Rational Design of Solar Cells for Efficient Solar Energy Conversion, 2018.

[18] A. K. Rajan and L. Cindrella, *W-ZnO Nanostructures with Distinct Morphologies: Properties and Integration into Dye Sensitized Solar Cells*, Ceramics International **46**, 8174 (2020).

[19] S. W. Himmah, M. Diantoro, N. A. Astarini, S. K. G. Tiana, Nasikhudin, A. Hidayat, and A. Taufiq, *Structural, Morphological, Optical, and Electrical Properties of TiO_2/ZnO Rods Multilayer Films as Photoanode on Dye-Sensitized Solar Cells*, Journal of Physics: Conference Series **1816**, 012095 (2021).

[20] S. Gorjian, E. Bousi, Ö. E. Özdemir, M. Trommsdorff, N. M. Kumar, A. Anand, K. Kant, and S. S. Chopra, *Progress and Challenges of Crop Production and Electricity Generation in Agrivoltaic Systems Using Semi-Transparent Photovoltaic Technology*, Renewable and Sustainable Energy Reviews **158**, 112126 (2022).

[21] P. Seferlis, P. S. Varbanov, A. I. Papadopoulos, H. H. Chin, and J. J. Klemeš, *Sustainable Design, Integration, and Operation for Energy High-Performance Process Systems*, Energy **224**, 120158 (2021).

[22] F. Babar, U. Mehmood, H. Asghar, M. H. Mehdi, A. U. H. Khan, H. Khalid, N. ul Huda, and Z. Fatima, *Nanostructured Photoanode Materials and Their Deposition Methods for Efficient and Economical Third Generation Dye-Sensitized Solar Cells: A Comprehensive Review*, Renewable and Sustainable Energy Reviews.

[23] M. Ye, X. Wen, M. Wang, J. Iocozzia, N. Zhang, C. Lin, and Z. Lin, *Recent Advances in Dye-Sensitized Solar Cells: From Photoanodes,*

Sensitizers and Electrolytes to Counter Electrodes, Materials Today **18**, 155 (2015).

[24] M. Bradha, N. Balakrishnan, A. Suvitha, T. Arumanayagam, M. Rekha, P. Vivek, P. Ajay, V. Sangeetha, and A. Steephen, *Experimental, Computational Analysis of Butein and Lanceoletin for Natural Dye-Sensitized Solar Cells and Stabilizing Efficiency by IoT*, Environment, Development and Sustainability **24**, 8807 (2022).

[25] M. Hosseinnezhad, S. Nasiri, M. Fathi, M. Ghahari, and K. Gharanjig, *Introduction of New Configuration of Dyes Contain Indigo Group for Dye-Sensitized Solar Cells: DFT and Photovoltaic Study*, Optical Materials **124**, 111999 (2022).

[26] A. Aboulouard, B. Elhadadi, M. Bensemlali, H. Nasrellah, A. Aarfane, and M. El idrissi, *First-Principles Study on Optoelectronic Properties of New Quinacridone Dye Derivatives in Dye Sensitized Photovoltaic Cells*, Materials Today: Proceedings (2022).

[27] D. Kurniawan, C. Cari, and A. Supriyanto, *Comparison of Nanocomposite ZnO/TiO_2 Composition Dye-Sensitized Solar Cell (DSSC) with Natural Dye Leaves of Green Mustard (Brassica Rapa)*, Journal of Physics: Conference Series **1842**, 012056 (2021).

[28] M. A. S. Z. Karib, Z. A. F. M. Napiah, and F. Arith, *Study of Zinc Dioxide (ZnO) And Titanium Dioxide (TiO_2) Photoanode For Solar Cell Applications Using Silvaco TCAD*, Inotek 2021 **1**, 107 (2021).

[29] X. Li, Y. Tu, S. Pace, U. Anselmi-Tamburini, and J. Briscoe, *Influence of ZnO Nanorod Surface Chemistry on Passivation Effect of TiO2shell Coating*, Journal of Physics D: Applied Physics **54**, 255107 (2021).

[30] M. Heydari Dokoohaki, F. Mohammadpour, and A. R. Zolghadr, *Dye-Sensitized Solar Cells Based on Deep Eutectic Solvent Electrolytes:*

Insights from Experiment and Simulation, Journal of Physical Chemistry C **125**, 15155 (2021).

[31] T. H. Meen, Y. T. Jhuo, S. M. Chao, N. Y. Lin, L. W. Ji, J. K. Tsai, T. C. Wu, W. R. Chen, W. Water, and C. J. Huang, *Effect of TiO_2 Nanotubes with TiCl4 Treatment on the Photoelectrode of Dye-Sensitized Solar Cells*, Nanoscale Research Letters **7**, 1 (2012).

[32] J. R. Hou, *Preparation of Titania Nanorod Arrays by Hydrothermal Method*, Advanced Materials Research **721**, 241 (2013).

[33] G. Wang, W. Xiao, and J. Yu, *High-Efficiency Dye-Sensitized Solar Cells Based on Electrospun TiO2 Multi-Layered Composite Film Photoanodes*, Energy **86**, 196 (2015).

[34] Y. L. Lai, H. R. Hsu, Y. K. Lai, C. Y. Zheng, Y. H. Chou, N. K. Hsu, and G. Y. Lung, *Influence of Thin Film Thickness of Working Electrodes on Photovoltaic Characteristics of Dye-Sensitized Solar Cells*, MATEC Web of Conferences **123**, 00030 (2017).

[35] A. M. A. Alsammarraie and M. K. Jawad, *Morphology Effect of Anodized TiO2 Nanotubes Active Anodes on Dye Sensitive Solar Cell*, Asian Journal of Chemistry **29**, 1985 (2017).

[36] N. Rab, F. K. Chong, H. I. Mohamed, and W. H. Lim, *Preparation of TiO_2 Nanoparticles by Hydrolysis of TiCl 4 Using Water and Glycerol Solvent System*, Journal of Physics: Conference Series **1123**, 012065 (2018).

[37] I. O. Selyanin, A. S. Steparuk, R. A. Irgashev, A. V. Mekhaev, G. L. Rusinov, and A. S. Vorokh, *TiO_2 Paste for DSSC Photoanode: Preparation and Optimization of Application Method*, Chimica Techno Acta **7**, 140 (2020).

[38] M. M. I. Megat Hasnan, N. Nayan, N. K. A. Hamed, Z. Azman, M. K.

Ahmad, M. S. Mohamed Ali, M. Z. Mohd Yusop, and I. M. Noor, *Improvement of Facile Hydrothermal TiO_2 Rutile Nanorod-Flower Using Second HiPIMS Deposition for DSSC Performance Enhancement*, Optical Materials **117**, 111149 (2021).

[39] W.-F. Lai, P.-L. Chao, X.-Y. Lin, Y.-P. Chen, J.-H. Liu, T.-F. Lin, W.-C. Hsu, and C.-Y. Huang, *Characteristics of Dye-Sensitized Solar Cells with TiO_2 Stripes*, Materials **15**, 4212 (2022).

[40] J. hun Bae, S. bin Do, S. ho Cho, K. min Lee, S. E. Lee, and T. O. Kim, *TiO2 Treatment Using Ultrasonication for Bubble Cavitation Generation and Efficiency Assessment of a Dye-Sensitized Solar Cell*, Ultrasonics Sonochemistry **83**, 105933 (2022).

[41] Y. Lou, S. Yuan, Y. Zhao, P. Hu, Z. Wang, M. Zhang, L. Shi, and D. Li, *A Simple Route for Decorating TiO_2 Nanoparticle over ZnO Aggregates Dye-Sensitized Solar Cell*, Chemical Engineering Journal **229**, 190 (2013).

[42] L. Yang and W. W. F. Leung, *Electrospun TiO_2 Nanorods with Carbon Nanotubes for Efficient Electron Collection in Dye-Sensitized Solar Cells*, Advanced Materials **25**, 1792 (2013).

[43] G. K. L. Goh, H. Q. Le, T. J. Huang, and B. T. T. Hui, *Low Temperature Grown ZnO@TiO_2 Core Shell Nanorod Arrays for Dye Sensitized Solar Cell Application*, Journal of Solid State Chemistry **214**, 17 (2014).

[44] M. Z. Razali, H. Abdullah, S. Shaari, and M. R. Taha, *Preparation of Photoelectrode CNT/TiO_2doped ZnO Nanocomposite by Sol-Gel Method for Dye-Sensitized Solar Cell*, Optoelectronics and Advanced Materials, Rapid Communications **8**, 451 (2014).

[45] F. Li, Y. Jiao, S. Xie, and J. Li, *Sponge-like Porous TiO_2/ZnO Nanodonuts for High Efficiency Dye-Sensitized Solar Cells*, Journal of

Power Sources **280**, 373 (2015).

[46] Z. Arifin, S. Suyitno, S. Hadi, and B. Sutanto, *Improved Performance of Dye-Sensitized Solar Cells with TiO_2 Nanoparticles/Zn-Doped TiO2 Hollow Fiber Photoanodes*, Energies **11**, 2922 (2018).

[47] S. Noor, S. Sajjad, S. A. K. Leghari, S. Shaheen, and A. Iqbal, *ZnO/TiO_2 Nanocomposite Photoanode as an Effective UV-Vis Responsive Dye Sensitized Solar Cell*, Materials Research Express **5**, 095905 (2018).

[48] F. Kabir, S. N. Sakib, and S. S. Uddin, *Effect of MWCNT's Concentration in TiO_2 Based DSSC and Degradation Study of the Cell*, Journal of Renewable and Sustainable Energy **11**, 023502 (2019).

[49] T. S. Bramhankar, S. S. Pawar, J. S. Shaikh, V. C. Gunge, N. I. Beedri, P. K. Baviskar, H. M. Pathan, P. S. Patil, R. C. Kambale, and R. S. Pawar, *Effect of Nickel–Zinc Co-Doped TiO_2 Blocking Layer on Performance of DSSCs*, Journal of Alloys and Compounds **817**, 152810 (2020).

[50] S. Aseena, N. Abraham, and V. S. Babu, *Synthesis of CNT Based Nanocomposites and Their Application as Photoanode Material for Improved Efficiency in DSSC*, Ceramics International **46**, 28355 (2020).

[51] S. Borbón, S. Lugo, D. Pourjafari, N. Pineda Aguilar, G. Oskam, and I. López, *Open-Circuit Voltage (VOC) Enhancement in TiO2-Based DSSCs: Incorporation of ZnO Nanoflowers and Au Nanoparticles*, ACS Omega **5**, 10977 (2020).

[52] A. Zatirostami, *Fabrication of Dye-Sensitized Solar Cells Based on the Composite TiO_2 Nanoparticles/ZnO Nanorods: Investigating the Role of Photoanode Porosity*, Materials Today Communications **26**, 102033 (2021).

[53] I. S. Mutashar and M. R. Al-bahrani, *Enhancing of Dye-Sensitized Solar Cells Efficiency Using Graphene - MWCNT Nanocomposite as*

Photoanode, Materials Today: Proceedings (2022).

[54] A. S, N. ABRAHAM, S. B. V, and B. S, *Effect of Carbon Nanotube Content in ZnO/Carbon Nanotube Based Photoanode for Dye Sensitized Solar Cells*, ECS Journal of Solid State Science and Technology (2022).

[55] M. Ramya, T. K. Nideep, V. P. N. Nampoori, and M. Kailasnath, *The Impact of ZnO Nanoparticle Size on the Performance of Photoanodes in DSSC and QDSSC: A Comparative Study*, Journal of Materials Science: Materials in Electronics **32**, 3167 (2021).

[56] A. Bourezgui, I. Kacem, M. Daoudi, and A. F. Al-Hossainy, *Influence of Gamma-Irradiation on Structural, Optical and Photocatalytic Performance of TiO_2 Nanoparticles Under Controlled Atmospheres*, Journal of Electronic Materials **49**, 1904 (2020).

[57] M. M. Abutalib and A. Rajeh, *Influence of MWCNTs/Li-Doped TiO_2 Nanoparticles on the Structural, Thermal, Electrical and Mechanical Properties of Poly (Ethylene Oxide)/Poly (Methylmethacrylate) Composite*, Journal of Organometallic Chemistry **918**, 121309 (2020).

[58] A. Prathan, J. Sanglao, T. Wang, C. Bhoomanee, P. Ruankham, A. Gardchareon, and D. Wongratanaphisan, *Controlled Structure and Growth Mechanism behind Hydrothermal Growth of TiO_2 Nanorods*, Scientific Reports **10**, 1 (2020).

[59] U. Nithiyanantham, A. Ramadoss, and S. Kundu, *Supercapacitor and Dye-Sensitized Solar Cell (DSSC) Applications of Shape-Selective TiO_2 Nanostructures*, RSC Advances **4**, 35659 (2014).

[60] B. O'Regan and M. Grätzel, *A Low-Cost, High-Efficiency Solar Cell Based on Dye-Sensitized Colloidal TiO2 Films*, Renewable Energy: Four Volume Set **2–4**, 208 (2018).

[61] A. Bartkowiak, O. Korolevych, G. L. Chiarello, M. Makowska-Janusik,

and M. Zalas, *How Can the Introduction of Zr4+ Ions into Tio_2 Nanomaterial Impact the Dssc Photoconversion Efficiency? A Comprehensive Theoretical and Experimental Consideration*, Materials **14**, 2955 (2021).

[62] G. V. Belessiotis, M. Antoniadou, I. Ibrahim, C. S. Karagianni, and P. Falaras, *Universal Electrolyte for DSSC Operation under Both Simulated Solar and Indoor Fluorescent Lighting*, Materials Chemistry and Physics **277**, 125543 (2022).

[63] A. H. Ahliha, F. Nurosyid, A. Supriyanto, and T. Kusumaningsih, *Optical Properties of Anthocyanin Dyes on TiO_2 as Photosensitizers for Application of Dye-Sensitized Solar Cell (DSSC)*, IOP Conference Series: Materials Science and Engineering **333**, 012018 (2018).

[64] M. T. Noman, M. A. Ashraf, and A. Ali, *Synthesis and Applications of Nano-TiO_2 : A Review*, Environmental Science and Pollution Research **26**, 3262 (2019).

[65] A. Rais and Y. Warti, *Analysis of DSSC (Dye Sensitized Solar Cell) and Characterization of ZnO-TiO_2 Semiconductor Using Method Sol-Gel as a Material Solar Cell*, Journal of Physics: Conference Series **2193**, 012093 (2022).

[66] I. K. Popoola, M. A. Gondal, J. M. AlGhamdi, and T. F. Qahtan, *Photofabrication of Highly Transparent Platinum Counter Electrodes at Ambient Temperature for Bifacial Dye Sensitized Solar Cells*, Scientific Reports **8**, 1 (2018).

[67] S. Biswas and H. Kim, *Solar Cells for Indoor Applications: Progress and Development*, Polymers **12**, 1338 (2020).

[68] J. L. Lan, Y. Y. Wang, C. C. Wan, T. C. Wei, H. P. Feng, C. Peng, H. P. Cheng, Y. H. Chang, and W. C. Hsu, *The Simple and Easy Way to*

Manufacture Counter Electrode for Dye-Sensitized Solar Cells, Current Applied Physics **10**, S168 (2010).

[69] S. M. Amir-Al Zumahi, N. Arobi, M. Mahbubur Rahman, M. Kamal Hossain, M. Ara Jahan Rozy, M. S. Bashar, A. Amri, H. Kabir, M. Abul Hossain, and F. Ahmed, *Understanding the Optical Behaviours and the Power Conversion Efficiency of Novel Organic Dye and Nanostructured TiO_2 Based Integrated DSSCs*, Solar Energy **225**, 129 (2021).

[70] B. Ünlü, S. Çakar, and M. Özacar, *The Effects of Metal Doped TiO_2 and Dithizone-Metal Complexes on DSSCs Performance*, Solar Energy **166**, 441 (2018).

[71] N. A. Karim, U. Mehmood, H. F. Zahid, and T. Asif, *Nanostructured Photoanode and Counter Electrode Materials for Efficient Dye-Sensitized Solar Cells (DSSCs)*, Solar Energy **185**, 165 (2019).

[72] N. Ramesar and I. Kretzschmar, Effect of Ionic Liquid Electrolytes in DSSCs with Titanium Dioxide (TiO_2) Inverse Opal Structures., 2013.

[73] Z. Yang, S. Gao, T. Li, F. Q. Liu, Y. Ren, and T. Xu, *Enhanced Electron Extraction from Template-Free 3D Nanoparticulate Transparent Conducting Oxide (TCO) Electrodes for Dye-Sensitized Solar Cells*, ACS Applied Materials and Interfaces **4**, 4419 (2012).

[74] M. Yahya, A. Bouziani, C. Ocak, Z. Seferoğlu, and M. Sillanpää, *Organic/Metal-Organic Photosensitizers for Dye-Sensitized Solar Cells (DSSC): Recent Developments, New Trends, and Future Perceptions*, Dyes and Pigments **192**, 109227 (2021).

[75] J. C. De Haro, E. Tatsi, L. Fagiolari, M. Bonomo, C. Barolo, S. Turri, F. Bella, and G. Griffini, *Lignin-Based Polymer Electrolyte Membranes for Sustainable Aqueous Dye-Sensitized Solar Cells*, ACS Sustainable Chemistry and Engineering **9**, 8550 (2021).

[76] S. Mehra, S. Bishnoi, A. Jaiswal, M. Jagadeeswararao, A. K. Srivastava, S. N. Sharma, and P. Vashishtha, *A Review on Spectral Converting Nanomaterials as a Photoanode Layer in Dye-sensitized Solar Cells with Implementation in Energy Storage Devices*, Energy Storage **2**, (2020).

[77] C. P. Cho, H. Y. Wu, and C. C. Lin, *Impacts of Sputter-Deposited Platinum Thickness on the Performance of Dye-Sensitized Solar Cells*, Electrochimica Acta **107**, 488 (2013).

[78] U. Mehmood, A. Ishfaq, and M. Sufyan, *Nanocomposites of Multi-Walled Carbon Nanotubes and Titanium Dioxide (MWCNTs/TiO_2) as Affective Counter Electrode Materials for Platinum-Free Dye-Sensitized Solar Cells (DSSCs)*, Solar Energy **220**, 949 (2021).

[79] D. A. Chalkias, C. Charalampopoulos, A. K. Andreopoulou, A. Karavioti, and E. Stathatos, *Spectral Engineering of Semi-Transparent Dye-Sensitized Solar Cells Using New Triphenylamine-Based Dyes and an Iodine-Free Electrolyte for Greenhouse-Oriented Applications*, Journal of Power Sources **496**, 229842 (2021).

[80] M. I. Ali Umar, Resti, V. Haris, and A. Ali Umar, *The Influence of MoSe2 Coated onto Pt Film to DSSC Performance with the Structure TiO2/Dye/LxMoSe2Pt ($0 \leq x \leq 5$)*, Materials Letters **275**, 128076 (2020).

[81] A. Omar, M. S. Ali, and N. Abd Rahim, *Electron Transport Properties Analysis of Titanium Dioxide Dye-Sensitized Solar Cells (TiO2-DSSCs) Based Natural Dyes Using Electrochemical Impedance Spectroscopy Concept: A Review*, Solar Energy **207**, 1088 (2020).

[82] A. Sacco, *Electrochemical Impedance Spectroscopy: Fundamentals and Application in Dye-Sensitized Solar Cells*, Renewable and Sustainable Energy Reviews **79**, 814 (2017).

[83] V. Stone, B. Nowack, A. Baun, N. van den Brink, F. von der Kammer,

M. Dusinska, R. Handy, S. Hankin, M. Hassellöv, E. Joner, and T. F. Fernandes, *Nanomaterials for Environmental Studies: Classification, Reference Material Issues, and Strategies for Physico-Chemical Characterisation*, Science of the Total Environment **408**, 1745 (2010).

[84] R. Alessandri, P. C. T. Souza, S. Thallmair, M. N. Melo, A. H. De Vries, and S. J. Marrink, *Pitfalls of the Martini Model*, Journal of Chemical Theory and Computation **15**, 5448 (2019).

[85] Q. A. Yousif and N. H. Haran, *Fabrication of TiO2 Nanotubes via Three-Electrodes Anodization Technique under Sound Waves Impact and Use in Dye-Sensitized Solar Cell*, Egyptian Journal of Chemistry **64**, 125 (2021).

[86] H. Al Jabri, M. H. Saleem, M. Rizwan, I. Hussain, K. Usman, and M. Alsafran, *Zinc Oxide Nanoparticles and Their Biosynthesis: Overview*, Life **12**, 594 (2022).

[87] S. T. Hayle, *Synthesis and Characterization of Titanium Oxide Nanomaterials Using Sol-Gel Method*, American Journal of Nanoscience and Nanotechnology **2**, 1 (2014).

[88] J. S. Biggins, S. Yazdi, and E. Ringe, *Magnesium Nanoparticle Plasmonics*, Nano Letters **18**, 3752 (2018).

[89] D. Das and P. Makal, *CdS Q‑Dot-Impregnated TiO2‑B Nanowire-Based Photoanodes for Efficient Photovoltaic Conversion in 'Q‑Dot Co-Sensitized DSSC,'* Energy and Fuels **35**, 8246 (2021).

[90] A. N. Kawade, P. K. Bhujbal, A. T. Supekar, K. M. Sonawane, H. M. Pathan, S. F. Shaikh, and A. A. Al-Kaitani, *Comparative Study of Eosin-Y and Rose Bengal Sensitized SnO_2-ZnO Composite Electrode for Dye-Sensitized Solar Cell*, ES Energy & Environment (2021).

[91] N. El-Atab, W. Babatain, R. Bahabry, R. Alshanbari, R. Shamsuddin, and

M. M. Hussain, *Ultraflexible Corrugated Monocrystalline Silicon Solar Cells with High Efficiency (19%), Improved Thermal Performance, and Reliability Using Low-Cost Laser Patterning*, ACS Applied Materials and Interfaces **12**, 2269 (2020).

[92] T. K. Das, P. Ilaiyaraja, and C. Sudakar, *Whispering Gallery Mode Assisted Enhancement in the Power Conversion Efficiency of DSSC and QDSSC Devices Using TiO_2 Microsphere Photoanodes*, ACS Applied Energy Materials **1**, 765 (2018).

[93] M. K. Hossain, M. T. Rahman, M. K. Basher, M. S. Manir, and M. S. Bashar, *Influence of Thickness Variation of Gamma-Irradiated DSSC Photoanodic TiO_2 Film on Structural, Morphological and Optical Properties*, Optik **178**, 449 (2019).

[94] V. Madurai Ramakrishnan, S. Pitchaiya, N. Muthukumarasamy, K. Kvamme, G. Rajesh, S. Agilan, A. Pugazhendhi, and D. Velauthapillai, *Performance of TiO_2 Nanoparticles Synthesized by Microwave and Solvothermal Methods as Photoanode in Dye-Sensitized Solar Cells (DSSC)*, International Journal of Hydrogen Energy **45**, 27036 (2020).

[95] V. Madurai Ramakrishnan, M. N., B. P., S. Pitchaiya, D. Velauthapillai, and A. Pugazhendhi, *Transformation of TiO_2 Nanoparticles to Nanotubes by Simple Solvothermal Route and Its Performance as Dye-Sensitized Solar Cell (DSSC) Photoanode*, International Journal of Hydrogen Energy **45**, 15441 (2020).

[96] P. Tiwana, P. Docampo, M. B. Johnston, H. J. Snaith, and L. M. Herz, *Electron Mobility and Injection Dynamics in Mesoporous ZnO, SnO_2, and TiO_2 Films Used in Dye-Sensitized Solar Cells*, ACS Nano **5**, 5158 (2011).

[97] J. Panda, U. P. Singh, and R. Sahu, *Synthesis, Characterization of TiO_2*

Nano Particles for Enhancement of Electron Transport Application in DSSC with Cu-BPCA Dye, IOP Conference Series: Materials Science and Engineering **410**, 012008 (2018).

[98] N. J. Ridha, F. K. Mohamad Alosfur, H. B. A. Kadhim, and L. M. Ahmed, *Synthesis of Ag Decorated TiO_2nanoneedles for Photocatalytic Degradation of Methylene Blue Dye*, Materials Research Express **8**, 125013 (2021).

[99] E. S. Teixeira, R. C. Cavalcanti, V. F. Nunes, P. H. F. M. Júnior, F. M. Lima, D. C. Pinho, M. de S. M. de Souza Filho, A. F. L. Almeida, and F. N. A. Freire, *Building and Testing a Spin Coater for the Deposition of Thin Films on DSSCS*, Materials Research **23**, 20200214 (2020).

[100] M. K. Hossain, A. A. Mortuza, S. K. Sen, M. K. Basher, M. W. Ashraf, S. Tayyaba, M. N. H. Mia, and M. J. Uddin, *A Comparative Study on the Influence of Pure Anatase and Degussa-P25 TiO_2 Nanomaterials on the Structural and Optical Properties of Dye Sensitized Solar Cell (DSSC) Photoanode*, Optik **171**, 507 (2018).

[101] S. Al Jitan, G. Palmisano, and C. Garlisi, *Synthesis and Surface Modification of TiO_2-Based Photocatalysts for the Conversion of CO_2*, Catalysts **10**, 227 (2020).

[102] L. Chen, M. E. Graham, G. Li, D. R. Gentner, N. M. Dimitrijevic, and K. A. Gray, *Photoreduction of CO2 by TiO_2 Nanocomposites Synthesized through Reactive Direct Current Magnetron Sputter Deposition*, Thin Solid Films **517**, 5641 (2009).

[103] J. E. S. Haggerty, L. T. Schelhas, D. A. Kitchaev, J. S. Mangum, L. M. Garten, W. Sun, K. H. Stone, J. D. Perkins, M. F. Toney, G. Ceder, D. S. Ginley, B. P. Gorman, and J. Tate, *High-Fraction Brookite Films from Amorphous Precursors*, Scientific Reports **7**, 1 (2017).

[104] H. J. Kwon, K. Shin, M. Soh, H. Chang, J. Kim, J. Lee, G. Ko, B. H. Kim, D. Kim, and T. Hyeon, *Large-Scale Synthesis and Medical Applications of Uniform-Sized Metal Oxide Nanoparticles*, Advanced Materials **30**, 1704290 (2018).

[105] R. Saad, A. Gamal, M. Zayed, A. M. Ahmed, M. Shaban, M. Binsabt, M. Rabia, and H. Hamdy, *Fabrication of ZnO/CNTs for Application in CO2 Sensor at Room Temperature*, Nanomaterials **11**, 3087 (2021).

[106] Y. Kang, F. Yu, L. Zhang, W. Wang, L. Chen, and Y. Li, *Review of ZnO-Based Nanomaterials in Gas Sensors*, Solid State Ionics **360**, 115544 (2021).

[107] A. Boudrioua, M. Chakaroun, and A. Fischer, *Organic Light-Emitting Diodes*, Organic Lasers 49 (2017).

[108] B. Siwach, S. Sharma, Mohan, and D., Structural, Optical and Morphological Properties of ZnO/MWCNTs Nanocomposite Photoanodes for Dye Sensitized Solar Cells (DSSCs) Application, Article, 2017.

[109] M. H. Habibi, M. Mardani, M. Habibi, and M. Zendehdel, *Enhanced Photovoltage (Voc) of Nano-Structured Zinc Tin Oxide (ZTO) Working Electrode Prepared by a Green Hydrothermal Route for Dye-Sensitized Solar Cell (DSSC)*, Journal of Materials Science: Materials in Electronics **28**, 3789 (2017).

[110] T. Guo, Q. Guo, S. Li, Y. Hu, S. Yun, and Y. Qian, *Effect of Surface Basicity over the Supported Cu-ZnO Catalysts on Hydrogenation of CO_2 to Methanol*, Journal of Catalysis **407**, 312 (2022).

[111] B. Sarkodie, Y. Hu, W. Bi, J. Jiang, and C. Li, *Promotional Effects of CuxO on the Activity of Cu/ZnO Catalyst toward Efficient CO Oxidation*, Applied Surface Science **548**, 149241 (2021).

[112] H. Fatima, Z. Y. Jin, Z. Shao, and X. J. Chen, *Recent Advances in ZnO-Based Photosensitizers: Synthesis, Modification, and Applications in Photodynamic Cancer Therapy*, Journal of Colloid and Interface Science **621**, 440 (2022).

[113] M. M. Ahmed, R. Zhao, J. Du, and J. Li, *Review—Nanostructural ZnO-Based Electrochemical Sensor for Environmental Application*, Journal of The Electrochemical Society **169**, 020573 (2022).

[114] C. S. Huang, C. Y. Yeh, Y. H. Chang, Y. M. Hsieh, C. Y. Ku, and Q. T. Lai, *Field Emission Properties of CNT-ZnO Composite Materials*, Diamond and Related Materials **18**, 452 (2009).

[115] Q. Liu, Y. K. Wu, J. Li, E. Liu, F. Tian, H. Zhao, and R. Chen, *Construction of Ag-Decorated ZnO with Oxygen Vacancies for Enhanced Antibacterial Activity via Increased H2O2 Production*, Journal of Inorganic Biochemistry **231**, 111778 (2022).

[116] S. D. Delekar, A. G. Dhodamani, K. V. More, T. D. Dongale, R. K. Kamat, S. F. A. Acquah, N. S. Dalal, and D. K. Panda, *Structural and Optical Properties of Nanocrystalline TiO2 with Multiwalled Carbon Nanotubes and Its Photovoltaic Studies Using Ru(II) Sensitizers*, ACS Omega **3**, 2743 (2018).

[117] M. Ben Manaa, N. Issaoui, Y. O. Al-Ghamdi, H. Belmabrouk, and A. Ben Lamine, *A Microscopic and Macroscopic Investigation of the Adsorption of N719 Dye on ZnO Nanopowders (ZNP) and ZnO Nanorods (ZNR) for Dye Sensitized Solar Cells Using Statistical Physics Treatment and DFT Simulation*, RSC Advances **10**, 27615 (2020).

[118] L. Ellis-Gibbings, V. Johansson, R. B. Walsh, L. Kloo, J. S. Quinton, and G. G. Andersson, *Formation of N719 Dye Multilayers on Dye Sensitized Solar Cell Photoelectrode Surfaces Investigated by Direct Determination*

of Element Concentration Depth Profiles, Langmuir **28**, 9431 (2012).

[119] P. M. Sommeling, B. C. O'Regan, R. R. Haswell, H. J. P. Smit, N. J. Bakker, J. J. T. Smits, J. M. Kroon, and J. A. M. Van Roosmalen, *Influence of a TiCl4 Post-Treatment on Nanocrystalline TiO 2 Films in Dye-Sensitized Solar Cells*, Journal of Physical Chemistry B **110**, 19191 (2006).

[120] M. K. Nazeeruddin, A. Kay, I. Rodicio, R. Humphry-Baker, E. Müller, P. Liska, N. Vlachopoulos, and M. Grätzel, *Conversion of Light to Electricity by Cis-X2Bis (2,2'-Bipyridyl-4,4'-Dicarboxylate) Ruthenium (II) Charge-Transfer Sensitizers (X = Cl−, Br−, I−, CN−, and SCN−) on Nanocrystalline TiO2 Electrodes*, Journal of the American Chemical Society **115**, 6382 (1993).

[121] N. Sakai, N. Kawashima, and T. N. Murakami, *Effect of TiCl4 Treatment on Porous ZnO Photoelectrodes for Dye-Sensitized Solar Cells*, Chemistry Letters **40**, 162 (2011).

[122] K. W. Ko, M. Lee, S. S. Sekhon, S. K. Balasingam, C. H. Han, and Y. Jun, *Efficiency Enhancement of Dye-Sensitized Solar Cells by the Addition of an Oxidizing Agent to the TiO2 Paste*, ChemSusChem **6**, 2117 (2013).

[123] A. V. Vorontsov, E. N. Kabachkov, I. L. Balikhin, E. N. Kurkin, V. N. Troitskii, and P. G. Smirniotis, *Correlation of Surface Area with Photocatalytic Activity of TiO 2* , Journal of Advanced Oxidation Technologies **21**, 127 (2018).

[124] J. Ma, J. Chang, Z. Lin, X. Guo, L. Zhou, Z. Liu, H. Xi, D. Chen, C. Zhang, and Y. Hao, *Elucidating the Roles of TiCl4 and PCBM Fullerene Treatment on TiO_2 Electron Transporting Layer for Highly Efficient Planar Perovskite Solar Cells*, Journal of Physical Chemistry C **122**,

1044 (2018).

[125] V. Kumar, R. Gupta, and A. Bansal, *Hydrothermal Growth of ZnO Nanorods for Use in Dye-Sensitized Solar Cells*, ACS Applied Nano Materials **4**, 6212 (2021).

[126] F. Bella, S. Galliano, G. Piana, G. Giacona, G. Viscardi, M. Grätzel, C. Barolo, and C. Gerbaldi, *Boosting the Efficiency of Aqueous Solar Cells: A Photoelectrochemical Estimation on the Effectiveness of TiCl 4 Treatment*, Electrochimica Acta **302**, 31 (2019).

[127] D. Li, Z. Jiang, Q. Xia, and Z. Yao, *Pre- or Post-$TiCl_4$ Treated TiO_2 Nano-Array Photoanode for QDSSC: Ti3+ Self-Doping, Flat-Band Level and Electron Diffusion Length*, Applied Surface Science **491**, 319 (2019).

[128] R. Yu, Q. Lin, S. F. Leung, and Z. Fan, *Nanomaterials and Nanostructures for Efficient Light Absorption and Photovoltaics*, Nano Energy **1**, 57 (2012).

[129] H. Eicken, F. Danielsen, J. M. Sam, M. Fidel, N. Johnson, M. K. Poulsen, O. A. Lee, K. V. Spellman, L. Iversen, P. Pulsifer, and M. Enghoff, *Connecting Top-Down and Bottom-Up Approaches in Environmental Observing*, BioScience **71**, 467 (2021).

[130] N. Abid, A. M. Khan, S. Shujait, K. Chaudhary, M. Ikram, M. Imran, J. Haider, M. Khan, Q. Khan, and M. Maqbool, *Synthesis of Nanomaterials Using Various Top-down and Bottom-up Approaches, Influencing Factors, Advantages, and Disadvantages: A Review*, Advances in Colloid and Interface Science **300**, 102597 (2022).

[131] N. Köbis, C. Starke, and I. Rahwan, *Artificial Intelligence as an Anti-Corruption Tool (AI-ACT) -- Potentials and Pitfalls for Top-down and Bottom-up Approaches*, (2021).

[132] Y. Wang, C. Zhao, D. Qin, M. Wu, W. Liu, and T. Ma, *Transparent*

Flexible Pt Counter Electrodes for High Performance Dye-Sensitized Solar Cells, Journal of Materials Chemistry **22**, 22155 (2012).

[133] M. G. Košević, M. M. Zarić, S. R. Stopić, J. S. Stevanović, T. E. Weirich, B. G. Friedrich, and V. V. Panić, *Structural and Electrochemical Properties of Nesting and Core/Shell Pt/Tio2 Spherical Particles Synthesized by Ultrasonic Spray Pyrolysis*, Metals **10**, 11 (2020).

[134] S. B. Wategaonkar, V. G. Parale, S. S. Mali, C. K. Hong, R. P. Pawar, P. S. Maldar, A. V. Moholkar, H. H. Park, B. M. Sargar, and R. K. Mane, *Influence of Tin Doped Tio2 Nanorods on Dye Sensitized Solar Cells*, Materials **14**, 6282 (2021).

[135] M. R. Al-Bahrani, H. H. Ali, H. M. Khudier, and A. S. Ali, *Efficiency Enhancement in Dye-Sensitized Solar Cell Using Pt and Nano Carbon as Counter Electrode*, http://solidstatetechnology.us/index.php/JSST/article/view/499.

[136] F. H. Ali, *Building a Spin Coater Device for Thin-Film Preparation*, in *IOP Conference Series: Materials Science and Engineering*, Vol. 757 (Institute of Physics Publishing, 2020), p. 012050.

[137] J. H. Kang, S. H. Lee, H. Ruh, and K. M. Yu, *Development of a Thickness Meter for Conductive Thin Films Using Four-Point Probe Method*, Journal of Electrical Engineering and Technology **16**, 2265 (2021).

[138] W. Que, A. Uddin, and X. Hu, *Thin Film TiO_2 Electrodes Derived by Sol-Gel Process for Photovoltaic Applications*, Journal of Power Sources **159**, 353 (2006).

[139] P. G. Choi, N. Shirahata, and Y. Masuda, *Tin Oxide Nanosheet Thin Film with Bridge Type Structure for Gas Sensing*, Thin Solid Films **698**,

137845 (2020).

[140] K. M. Kuznetsov, M. I. Kozlov, A. N. Aslandukov, A. A. Vashchenko, A. V. Medved'ko, E. V. Latipov, A. S. Goloveshkin, D. M. Tsymbarenko, and V. V. Utochnikova, *Eu(Tta)3DPPZ-Based Organic Light-Emitting Diodes: Spin-Coatingvs. Vacuum-Deposition*, Dalton Transactions **50**, 9685 (2021).

[141] M. Pichumani, P. Bagheri, K. M. Poduska, W. González-Viñas, and A. Yethiraj, *Dynamics, Crystallization and Structures in Colloid Spin Coating*, Soft Matter **9**, 3220 (2013).

[142] G. De Silva, P. Payagala, C. Edirisinghe, and G. Illeperuma, *Development of a Cost-Effective and Reliable Spin Coating Device Promoting Local Enterprises to Meet the Research Needs*, Procedings of Technical Sesions **37**, 46 (2021).

[143] M. D. Tyona, *A Comprehensive Study of Spin Coating as a Thin Film Deposition Technique and Spin Coating Equipment*, Advances in Materials Research **2**, 181 (2013).

[144] A. Mishra, N. Bhatt, and A. K. Bajpai, *Nanostructured Superhydrophobic Coatings for Solar Panel Applications*, in *Nanomaterials-Based Coatings: Fundamentals and Applications*, edited by Phuong Nguyen Tri, Sami Rtimi, and Claudiane M. Ouellet Plamondon (Elsevier, 2019), pp. 397–42.

[145] S. R. Puniredd, W. Pisula, and K. Müllen, *Influence of Film Morphology on Optical and Electronic Properties of Organic Materials*, in *Handbook of Organic Materials for Optical and (Opto)Electronic Devices: Properties and Applications* (Elsevier Inc., 2013), pp. 83–101.

[146] J. C. Chou, Y. C. Lin, C. H. Lai, P. Y. Kuo, Y. H. Nien, R. H. Syu, Z. R. Yong, and Y. T. Wu, *Silver Nanowires Modified Flexible Dye-Sensitive*

Solar Cells and Application with the Internet of Things under Low Illumination, IEEE Journal of Photovoltaics **11**, 1243 (2021).

[147] M. H. El-Ahmar, A. H. M. El-Sayed, and A. M. Hemeida, *Mathematical Modeling of Photovoltaic Module and Evalute the Effect of Varoius Paramenters on Its Performance*, https://doi.org/10.1109/MEPCON.2016.7836976.

[148] M. C. Kao, H. Z. Chen, S. L. Young, C. Y. Kung, and C. C. Lin, *The Effects of the Thickness of TiO_2 Films on the Performance of Dye-Sensitized Solar Cells*, Thin Solid Films **517**, 5096 (2009).

[149] R. S. Dubey, K. V. Krishnamurthy, and S. Singh, *Experimental Studies of TiO2 Nanoparticles Synthesized by Sol-Gel and Solvothermal Routes for DSSCs Application*, Results in Physics **14**, 102390 (2019).

[150] D. Kiermasch, L. Gil-Escrig, H. J. Bolink, and K. Tvingstedt, *Effects of Masking on Open-Circuit Voltage and Fill Factor in Solar Cells*, Joule **3**, 16 (2019).

[151] E. S. Systems, *13th International Symposium on Process Systems* (2019).

[152] K. Sahu, M. Dhonde, and V. V. S. Murty, *Microwave-Assisted Hydrothermal Synthesis of Cu-Doped TiO_2 Nanoparticles for Efficient Dye-Sensitized Solar Cell with Improved Open-Circuit Voltage*, International Journal of Energy Research **45**, 5423 (2021).

[153] A. Nirala, N. Kumar, D. B. Singh, S. K. Sharma, A. K. Shrivastava, S. Chandan, and H. Prasad, *Fabrication of a Tubular Furnace for Sintering and Heat Treatment of Metals/Alloys*, Materials Today: Proceedings **28**, 2180 (2020).

[154] A. Mwafy Eman, M. Dawy, A. Abouelsayed, I. A. Elsabbagh, and M. M. Elfass, *Synthesis and Characterization of Multi-Walled Carbon Nanotubes Decorated ZnO Nanocomposite*, Egyptian Journal of

Chemistry **59**, 1061 (2016).

[155] A. E. Mariño-Gámez, G. E. Acosta-González, M. I. Pech-Canul, M. B. Hernández, S. García-Villarreal, P. Zambrano-Robledo, B. S. Vera Barrios, and J. A. Aguilar-Martínez, *Influence of High Energy Ball Milling on Structural, Microstructural and Optical Properties of TiO2 Nanoparticles*, Ceramics International **48**, 3362 (2022).

[156] B. Manikandan, K. Murali, and R. John, *Optical, Morphological and Microstructural Investigation of TiO2nanoparticles for Photocatalytic Application*, http://ijc.iaush.ac.ir/article_680810.html.

[157] F. C. Krebs, F. C. Krebs, M. JÃ¸rgensen, E. Bundgaard, R. de Bettignies, F. C. Krebs, E. A. Katz, K. Norrman, E. Bundgaard, F. C. Krebs, K. Norrman, S. Cros, R. de Bettignies, M. Firon, F. C. Krebs, T. Aernouts, S. Cros, F. C. Krebs, and F. C. Krebs, *Characterization of Organic Solar Cells*, Polymer Photovoltaics: A Practical Approach 2 (2010).

[158] A. Ray, A. Roy, S. Bhattacharjee, S. Jana, C. K. Ghosh, C. Sinha, and S. Das, *Correlation between the Dielectric and Electrochemical Properties of TiO2-V2O5 Nanocomposite for Energy Storage Application*, Electrochimica Acta **266**, 404 (2018).

[159] O. A. Khaleel and D. S. Ahmed, *Interface Engineering at Electron Transport/Perovskite Layers Using Wetting Mesoporous Titanium Dioxide to Fabricate Efficient and Stable Perovskite Solar Cells*, International Journal of Energy Research **46**, 11163 (2022).

[160] J. B. Coulter and D. P. Birnie, *Assessing Tauc Plot Slope Quantification: ZnO Thin Films as a Model System*, Physica Status Solidi (B) **255**, 1700393 (2018).

[161] P. Makuła, M. Pacia, and W. Macyk, *How To Correctly Determine the Band Gap Energy of Modified Semiconductor Photocatalysts Based on*

UV-Vis Spectra, Journal of Physical Chemistry Letters **9**, 6814 (2018).

[162] C. Elias, P. Valvin, T. Pelini, A. Summerfield, C. J. Mellor, T. S. Cheng, L. Eaves, C. T. Foxon, P. H. Beton, S. V. Novikov, B. Gil, and G. Cassabois, *Direct Band-Gap Crossover in Epitaxial Monolayer Boron Nitride*, Nature Communications 2019 10:1 **10**, 1 (2019).

[163] M. A. Brza, S. B. Aziz, H. Anuar, and M. H. F. Al Hazza, *From Green Remediation to Polymer Hybrid Fabrication with Improved Optical Band Gaps*, International Journal of Molecular Sciences 2019, Vol. 20, Page 3910 **20**, 3910 (2019).

[164] B. C. da Silva, O. D. D. Couto, H. T. Obata, M. M. de Lima, F. D. Bonani, C. E. de Oliveira, G. M. Sipahi, F. Iikawa, and M. A. Cotta, *Optical Absorption Exhibits Pseudo-Direct Band Gap of Wurtzite Gallium Phosphide*, Scientific Reports 2020 10:1 **10**, 1 (2020).

[165] S. Sarker, A. J. S. Ahammad, H. W. Seo, and D. M. Kim, *Electrochemical Impedance Spectra of Dye-Sensitized Solar Cells: Fundamentals and Spreadsheet Calculation*, International Journal of Photoenergy **2014**, (2014).

[166] L. Kojovic and A. Turak, Assembly of a Four Point Probe Assembly of a Four Point Probe That Operates under the Van Der Pauw Method, 2017.

[167] S. Choudhary, R. Narula, and S. Gangopadhyay, *Thin Cu Film Resistivity Using Four Probe Techniques: Effect of Film Thickness and Geometrical Shapes*, in *AIP Conference Proceedings*, Vol. 1953 (American Institute of Physics Inc., 2018), p. 100054.

[168] J. L. Yagüe, A. Guimerà, R. Villa, N. Agulló, and S. Borrós, *A New Four-Point Probe Design to Measure Conductivity in Polymeric Thin Films*, Afinidad **70**, 166 (2013).

[169] J. H. Kang, G. Ying, Y. C. Cheng, C. S. Kim, S. H. Lee, and K. M. Yu,

An International Comparison Measurement of Silicon Wafer Sheet Resistance Using the Four-Point Probe Method, Journal of Electrical Engineering and Technology **10**, 325 (2015).

[170] A. Awodugba, Investigation of Annealing Effect Electrical and Optical Properties of ZnS-CuS Thin Films Prepared by SILAR Technique, 2011.

[171] L. B. Valdes, *Resistivity Measurements on Germanium for Transistors*, Proceedings of the IRE **42**, 420 (1954).

[172] M. D. Tyona, *A Theoritical Study on Spin Coating Technique*, Advances in Materials Research **2**, 195 (2013).

[173] D. H. Chen, J. J. Yeh, and T. C. Huang, *Synthesis of Platinum Ultrafine Particles in AOT Reverse Micelles*, Journal of Colloid and Interface Science **215**, 159 (1999).

[174] T.-T. Duong, J.-S. Choi, A.-T. Le, and S.-G. Yoon, *Morphology Control of Pt Counter Electrodes Using a Pt Precursor Solution with $H_2PtCl_6 \cdot xH$ 2 O for Highly Efficient Dye-Sensitized Solar Cells* , Journal of The Electrochemical Society **161**, H166 (2014).

[175] L. L. Li, C. W. Chang, H. H. Wu, J. W. Shiu, P. T. Wu, and E. Wei-Guang Diau, *Morphological Control of Platinum Nanostructures for Highly Efficient Dye-Sensitized Solar Cells*, Journal of Materials Chemistry **22**, 6267 (2012).

[176] A. Ghifari, D. X. Long, S. Kim, B. Ma, and J. Hong, *Transparent Platinum Counter Electrode Prepared by Polyol Reduction for Bifacial, Dye-Sensitized Solar Cells*, Nanomaterials **10**, 502 (2020).

[177] S. Gullace, F. Nastasi, F. Puntoriero, S. Trusso, and G. Calogero, *A Platinum-Free Nanostructured Gold Counter Electrode for DSSCs Prepared by Pulsed Laser Ablation*, Applied Surface Science **506**, 144690 (2020).

[178] H. Ye, R. W. J. Scott, and R. M. Crooks, *Synthesis, Characterization, and Surface Immobilization of Platinum and Palladium Nanoparticles Encapsulated within Amine-Terminated Poly(Amidoamine) Dendrimers*, Langmuir **20**, 2915 (2004).

[179] C. Li, J. H. Hsieh, J. C. Cheng, and C. C. Huang, *Optical and Photoelectrochemical Studies on Ag_2O/TiO_2 Double-Layer Thin Films*, Thin Solid Films **570**, 436 (2014).

[180] R. S. Moraes, E. Saito, D. M. G. Leite, M. Massi, and A. S. Da Silva Sobrinho, *Optical, Electrical and Electrochemical Evaluation of Sputtered Platinum Counter Electrodes for Dye Sensitized Solar Cells*, Applied Surface Science **364**, 229 (2016).

[181] T. Kalaivani and P. Anilkumar, *Role of Temperature on the Phase Modification of TiO_2 Nanoparticles Synthesized by the Precipitation Method*, Silicon **10**, 1679 (2018).

[182] M. Lv, D. Zheng, M. Ye, L. Sun, J. Xiao, W. Guo, and C. Lin, *Densely Aligned Rutile TiO2 Nanorod Arrays with High Surface Area for Efficient Dye-Sensitized Solar Cells*, Nanoscale **4**, 5872 (2012).

[183] C. Cao, C. Hu, X. Wang, S. Wang, Y. Tian, and H. Zhang, *UV Sensor Based on TiO2 Nanorod Arrays on FTO Thin Film*, Sensors and Actuators, B: Chemical **156**, 114 (2011).

[184] G. Bennett, *CHRIS Hazardous Chemical Data Manual*, 2nd ed., Vol. 14 (U.S. Government Printing Office, Washington, DC, 1987).

[185] J. H. Lee and Y. S. Yang, *Effect of HCl Concentration and Reaction Time on the Change in the Crystalline State of TiO_2 Prepared from Aqueous $TiCl_4$ Solution by Precipitation*, Journal of the European Ceramic Society **25**, 3573 (2005).

[186] D. Suh, *Etch Characteristics and Morphology of Al_2O_3/TiO_2 Stacks for*

Silicon Surface Passivation, Sustainability (Switzerland) **11**, 3857 (2019).

[187] L. M. Cursaru, S. N. Valsan, M. E. Puscasu, I. A. Tudor, N. Zarnescu-Ivan, B. S. Vasile, and R. M. Piticescu, *Study of Zno-Cnt Nanocomposites in High-Pressure Conditions*, Materials **14**, 5330 (2021).

[188] N. Kumar, M. Patel, T. T. Nguyen, S. Kim, and J. Kim, *Effect of TiO_2 Layer Thickness of TiO_2/NiO Transparent Photovoltaics*, Progress in Photovoltaics: Research and Applications **29**, 943 (2021).

[189] M. F. Hossain, M. S. Pervez, and M. A. I. Nahid, *Influence of Film Thickness on Optical and Morphological Properties of TiO_2 thin Films*, Emerging Materials Research **9**, 186 (2020).

[190] M. A. Mahadik, P. S. Shinde, M. Cho, and J. S. Jang, *Metal Oxide Top Layer as an Interfacial Promoter on a ZnIn2S4/TiO2 Heterostructure Photoanode for Enhanced Photoelectrochemical Performance*, Applied Catalysis B: Environmental **184**, 337 (2016).

[191] M. M. El-Nahass, M. H. Ali, and A. El-Denglawey, *Structural and Optical Properties of Nano-Spin Coated Sol-Gel Porous TiO_2 Films*, Transactions of Nonferrous Metals Society of China (English Edition) **22**, 3003 (2012).

[192] M. M. El-Nahass, H. S. Soliman, and A. El-Denglawey, *Absorption Edge Shift, Optical Conductivity, and Energy Loss Function of Nano Thermal-Evaporated N-Type Anatase TiO_2 Films*, Applied Physics A: Materials Science and Processing **122**, (2016).

[193] A. N. Fouda, *Influence of Deposition Temperature on the Structural and Dispersion Parameters of TiO_2 Thin Films*, Applied Physics A: Materials Science and Processing **126**, 1 (2020).

[194] M. M. Karkare, *Estimation of Band Gap and Particle Size of TiO_2 Nanoparticle Synthesized Using Sol Gel Technique*, Proceedings - 2014 IEEE International Conference on Advances in Communication and Computing Technologies, ICACACT 2014 (2015).

[195] B. S. Avinash, V. S. Chaturmukha, H. S. Jayanna, C. S. Naveen, M. P. Rajeeva, B. M. Harish, S. Suresh, and A. R. Lamani, *Effect of Particle Size on Band Gap and DC Electrical Conductivity of TiO_2 Nanomaterial*, AIP Conference Proceedings **1728**, 020426 (2016).

[196] H. B. A. Kadhim, N. J. Ridha, F. K. Mohamad Alosfur, N. M. Umran, R. Madlol, K. J. Tahir, and R. T. Ahmed, *Ablation of ZnO in Liquid by Nanosecond Laser*, Journal of Physics: Conference Series **1032**, 012039 (2018).

[197] R. A. Shathy, S. A. Fahim, M. Sarker, M. S. Quddus, M. Moniruzzaman, S. M. Masum, and M. A. I. Molla, *Natural Sunlight Driven Photocatalytic Removal of Toxic Textile Dyes in Water Using B-Doped ZnO/TiO_2 Nanocomposites*, Catalysts **12**, 308 (2022).

[198] S. S. Fouad, B. Parditka, M. Nabil, E. Baradács, S. Negm, H. E. Atyia, and Z. Erdélyi, *Bilayer Number Driven Changes in Polarizability and Optical Property in ZnO/TiO_2 Nanocomposite Films Prepared by ALD*, Optik **233**, 166617 (2021).

[199] L. Munguti and F. Dejene, *Effects of Zn:Ti Molar Ratios on the Morphological, Optical and Photocatalytic Properties of ZnO-TiO_2 Nanocomposites for Application in Dye Removal*, Materials Science in Semiconductor Processing **128**, 105786 (2021).

[200] X. Zou, X. Dong, L. Wang, H. Ma, X. Zhang, and X. Zhang, *Preparation of Ni Doped ZnO-TiO_2 Composites and Their Enhanced Photocatalytic Activity*, International Journal of Photoenergy **2014**, (2014).

[201] T. Das, X. Rocquefelte, and S. Jobic, *Ab Initio Positioning of the Valence and Conduction Bands of Bulk Photocatalysts: Proposition of Absolute Reference Energy*, Journal of Physical Chemistry C **124**, 19426 (2020).

[202] B. Choudhury, M. Dey, and A. Choudhury, *Defect Generation, d-d Transition, and Band Gap Reduction in Cu-Doped TiO_2 Nanoparticles*, International Nano Letters **3**, 1 (2013).

[203] S. Ayed, R. Ben Belgacem, J. O. Zayani, and A. Matoussi, *Structural and Optical Properties of ZnO/TiO_2 Composites*, Superlattices and Microstructures **91**, 118 (2016).

[204] A. S. Alshammari, Z. R. Khan, M. Gandouzi, M. Mohamed, M. Bouzidi, M. Shkir, and H. M. Alshammari, *Tailoring the Optical Properties and the UV Detection Performance of Sol-Gel Deposited ZnO Nanostructured Thin Films via Cd and Na Co-Doping*, Optical Materials **126**, 112146 (2022).

[205] E. Przeździecka, K. M. Paradowska, A. Lysak, A. Wierzbicka, P. Sybilski, E. Placzek-Popko, R. Jakiela, J. M. Sajkowski, and A. Kozanecki, *Influence of As Doping on the Properties of Nonpolar ZnO*, Thin Solid Films **720**, 138520 (2021).

[206] K. Janani Archana, A. Christy Preetha, and K. Balasubramanian, *Influence of Urbach Energy in Enhanced Photocatalytic Activity of Cu Doped ZnO Nanoparticles*, Optical Materials **127**, 112245 (2022).

[207] H. M. Ghartavol, M. R. Mohammadi, A. Afshar, and Y. Li, *On the Assessment of Incorporation of CNT-TiO_2 Core-Shell Structures into Nanoparticle TiO_2 Photoanodes in Dye-Sensitized Solar Cells*, Photochemical and Photobiological Sciences **18**, 1840 (2019).

[208] A. Mathew, G. M. Rao, and N. Munichandraiah, *Dye Sensitized Solar Cell Based on Platinum Decorated Multiwall Carbon Nanotubes as*

Catalytic Layer on the Counter Electrode, Materials Research Bulletin **46**, 2045 (2011).

[209] S. A. Svatek, C. Bueno-Blanco, D. Y. Lin, J. Kerfoot, C. Macías, M. H. Zehender, I. Tobías, P. García-Linares, T. Taniguchi, K. Watanabe, P. Beton, and E. Antolín, *High Open-Circuit Voltage in Transition Metal Dichalcogenide Solar Cells*, Nano Energy **79**, 105427 (2021).

[210] M. S. Su'ait, M. Y. A. Rahman, and A. Ahmad, *Review on Polymer Electrolyte in Dye-Sensitized Solar Cells (DSSCs)*, Solar Energy **115**, 452 (2015).

[211] J. M. K. W. Kumari, N. Sanjeevadharshini, M. A. K. L. Dissanayake, G. K. R. Senadeera, and C. A. Thotawatthage, *The Effect of TiO_2 Photo Anode Film Thickness on Photovoltaic Properties of Dye-Sensitized Solar Cells*, Ceylon Journal of Science **45**, 33 (2016).

[212] A. Eshaghi and A. A. Aghaei, *Effect of TiO_2-Graphene Nanocomposite Photoanode on Dye-Sensitized Solar Cell Performance*, Bulletin of Materials Science **38**, 1177 (2015).

[213] J. Park, P. Lee, and M. J. Ko, *Design and Fabrication of Long-Term Stable Dye-Sensitized Solar Cells: Effect of Water Contents in Electrolytes on the Performance*, International Journal of Precision Engineering and Manufacturing - Green Technology **6**, 125 (2019).

[214] V. Ramasubbu, P. R. Kumar, E. M. Mothi, K. Karuppasamy, H. S. Kim, T. Maiyalagan, and X. S. Shajan, *Highly Interconnected Porous TiO_2-Ni-MOF Composite Aerogel Photoanodes for High Power Conversion Efficiency in Quasi-Solid Dye-Sensitized Solar Cells*, Applied Surface Science **496**, 143646 (2019).

[215] Y. Gu, T. Wang, Y. N. Dong, H. Zhang, D. Wu, and W. Chen, *Ferroelectric Polyoxometalate-Modified Nano Semiconductor TiO_2 for*

Increasing Electron Lifetime and Inhibiting Electron Recombination in Dye-Sensitized Solar Cells, Inorganic Chemistry Frontiers **7**, 3072 (2020).

[216] J. Sun, X. Yang, L. Zhao, B. Dong, and S. Wang, *Ag-Decorated TiO2 Nanofibers for Highly Efficient Dye Sensitized Solar Cell*, Materials Letters **260**, 126882 (2020).

[217] Y. H. Nien, Z. R. Yong, C. S. Ho, J. C. Chou, C. H. Lai, P. Y. Kuo, G. M. Hu, J. X. Chang, and Y. C. Lin, *Preparation and Characterization of the Dye-Sensitized Solar Cell with Modified Photoanode by FePt/TiO_2 Nanofibers*, IEEE Transactions on Nanotechnology **20**, 507 (2021).

[218] A. K. Alanazi, *Effect of Zno Nanomaterial and Red and Green Cabbage Dyes on the Performance of Dye-Sensitised Solar Cells*, Coatings **11**, 1057 (2021).

[219] R. Shashanka, H. Esgin, V. M. Yilmaz, and Y. Caglar, *Fabrication and Characterization of Green Synthesized ZnO Nanoparticle Based Dye-Sensitized Solar Cells*, Journal of Science: Advanced Materials and Devices **5**, 185 (2020).

[220] S. Sharma, M. Khannam, and S. K. Dolui, *A Quasi Solid State Dye Sensitized Solar Cell Based on Gelatin/Multiwalled Carbon Nanotube Gel Electrolyte and ZnO Nanorod Photoanode*, Journal of Materials Science: Materials in Electronics **27**, 7864 (2016).

[221] I. Mohammadi, F. Zeraatpisheh, E. Ashiri, and K. Abdi, *Solvothermal Synthesis of G-C3N4 and ZnO Nanoparticles on TiO_2 Nanotube as Photoanode in DSSC*, International Journal of Hydrogen Energy **45**, 18831 (2020).

[222] T. Sawatsuk, A. Chindaduang, C. Sae-kung, S. Pratontep, and G. Tumcharern, *Dye-Sensitized Solar Cells Based on TiO_2-MWCNTs*

Composite Electrodes: Performance Improvement and Their Mechanisms, Diamond and Related Materials **18**, 524 (2009).

[223] Y. L. Zhao, D. S. Yao, C. B. Song, L. Zhu, J. Song, X. Q. Gu, and Y. H. Qiang, *CNT-G-TiO_2 Layer as a Bridge Linking TiO_2 Nanotube Arrays and Substrates for Efficient Dye-Sensitized Solar Cells*, RSC Advances **5**, 43805 (2015).

الخلاصة

تلعب الابتكارات في تكنولوجيا المواد دورًا رئيسيًا في مجالات الطاقة الكهروضوئية من أجل التحول النموذجي من الوقود الأحفوري إلى المصادر المتجددة، ولهذا فإن مصادر الطاقة الشمسية تعد واحدة من مصادر الطاقة المتجددة التي أظهرت العديد من المزايا مثل التكلفة المنخفضة وسهولة التنصيب إلى جانب إنها صديق للبيئة.

تتمثل الأهداف الرئيسة لهذه الدراسة في تصنيع وتحسين أداء الخلايا الشمسية الصبغية الحساسة، فقد تم تحضير أغشية رقيقة من البلاتين على سطح الزجاج الموصل FTO بتراكيز مختلفة من محلول H_2PtCl_6 2.5 ,5، 10، 15 باستعمال تقنية الطلاء الدوراني كقطب كاثود هذا من هذه الجانب، ومن جانب آخر فقد تم استعمال بوتوكسيد التيتانيوم $Ti(OBu)_4$ لتحضير قضبان ثاني أكسيد التيتانيوم TiO_2 النانوية كقطب أنود ضوئي باستعمال الطريقة الحرارية المائية مباشرة على زجاج FTO ، مع نسبة حمض الهيدروكلوريك (HCl) – الماء (H_2O) مختلفة 7,5-12,5 و 10-10 و 7,5- 12,5 و 5-15 مل لتر و زمن التنميش 24 و 48 و 72 ساعة، فضلا عن ذلك فقد تم تصنيع قضبان اوكسيد الزنك النانوية على قضبان ثاني أكسيد التيتانيوم TiO_2 النانوية باستعمال عملية البذر والنمو، إذ تم استعمال محلول أسيتات الزنك بتركيز 0.01 مولار لتحضير طبقة من بذور ZnO على NR TiO_2 بواسطة جهاز الطلاء الدوراني ليتم بعدها استعمال الطريقة الحرارية المائية لتنمية ZnO NR في محلول مائي 0.03 مولاري من نترات الزنك هيدرات و hexamethylenetetramine (HMT) والماء منزوع الأيونات (DI)، فضلا عن إدخال الأنابيب النانوية الكربونية متعددة الجدران (MWCNT) في طبقة من بذور ZnO بنسب وزنية مختلفة 0 ، 0.5 ، 1 و 1.5 ٪. أخيرًا ، تم غمر القطب الضوئي المحضر في صبغة N719 لمدة 24 ساعة وتجميعها مع قطب الكاثود لإكمال DSSC على شكل شطيرة ثم لصقها مع بعض باستعمال Meltonix 45 µm و تعبئتها بالمحلول الالكتروليتي (Iodolyte HI-30).

أظهرت نتائج حيود الأشعة السينية (XRD) إن عينات TiO_2 لها بنية بطور الروتيل متعدد البلورات بالاتجاه المفضل (101) و (002) بينما نمت ZnO NRs على اتجاه (002). علاوة على ذلك، لا توجد قمة ل MWCNT مميزة بسبب كميتها الصغيرة التي لا يمكن اكتشافها، هذا فضلا عن تغيير تركيز MWCNT الذي أدّى إلى ازاحة موضع القمة الخاصة بالـ ZnO.
إن زيادة تركيز حمض الهيدروكلوريك تؤدي إلى زيادة قطر TiO_2 NRs وتقليل الطول كما هو

معروض في صور المجهر الماسح الإلكتروني SEM ، بينما تؤدي زيادة زمن التنميش إلى انخفاض في قطر وطول TiO_2 NRs، فضلا عن إن شكل ZnO عبارة عن مجموعات من قضبان ZnO وذات قمم سداسية الشكل. من خلال طيف حيود الأشعة السينية المشتتة للطاقة (EDX) تبين أن العينات المحضرة كانت نقية ولم يتم العثور على شوائب أخرى، في حين تبين الخصائص البصرية لـ TiO_2 NRs المُصنَّعة من خلال تحليل الطيف المرئي و فوق البنفسجي (UV-Vis) إن فجوة الطاقة البصرية تقل مع زيادة تركيز حمض الهيدروكلوريك، بينما تزداد مع زيادة وقت النقش، ويؤدي نمو ZnO على TiO_2 NRs إلى زيادة Eg للقطب البصري، بينما يقل مع زيادة تركيز MWCNT.

ومن خلال منحنى J-V المحسوب بواسطة منظومة قياس كفاءة الخلايا الشمسية نجد أن الزيادة في تركيز محلول H_2PtCl_6 تؤدي إلى زيادة كفاءة الخلايا الشمسية (η) 1.666 و 2.067 و 2.96 و 2.96 للغشاء ذو الطبقة الواحدة، بينما تنخفض تدريجيًا 2.956 و 2.938 و 2.891 و 2.816 مع زيادة في تركيز محلول H_2PtCl_6 للغشاء ذو طبقة مزدوجة، هذا من جهة . ومن جهة أخرى فقد كانت الكفاءة المثلى (η) لـ DSSC على أساس TiO_2 NRs هي 3.255٪ في العينة ET إذ كانت حالة التحضير H_2O+7.5HCl 12.5 بزمن تنميش 48 ساعة. ويُظهر DSSC الذي تم إنشاؤه باستعمال الأنود الضوئي ZnO NRs / TiO_2 NRs زيادة في الكفاءة بشكل ملحوظ بنسبة 20٪ إذ تم تحسين نقل الإلكترونات، كما تبلغ كفاءة الخلايا الشمسية لـ MWCNT المُدرج في طبقة بذورة ZnO للخلايا المصنعة 3.938 ، 4.358 ، 4.047 و 3.203 مع زيادة تركيز MWCNT، و في أفضل الأوضاع فقد كانت نسبة MWCNT عند 0.5٪ والتي ادّت إلى زيادة كفاءة التحويل بنسبة 10٪ تقريبًا. اخيرا وجد ان اجمالي التحسين على كفاءة الخلية الشمسية لثاني اوكسيد التيتانيوم هو 34% .

جامعة كربلاء
كلية العلوم
قسم الفيزياء

تعزيز اداء الخلية الشمسية $MWCNTs\text{-}ZnO / TiO_2$ نانوية التركيب

اطروحة مقدمة إلى مجلس كلية العلوم / جامعة كربلاء وهي جزء من متطلبات نيل درجة الدكتوراه في علوم الفيزياء

من قبـــــل

عمار صلاح حميـد

بأشـــــــــراف

أ.د رجاء عبد الامير مدلول **أ.د نور جواد رضا**

١٤٤٤ هـ **٢٠٢٢ م**